

**Monodisperse elastic shells:**

**a 3D study of jammed granular matter and**

**microencapsulation**

Cover: Confocal images of jammed, unloaded and reloaded elastic shells

PhD thesis, Utrecht University, The Netherlands, May 2014

ISBN 978-90-393-6143-6

A digital version of this thesis is available at <http://www.colloid.nl>

# **Monodisperse elastic shells: a 3D study of jammed granular matter and microencapsulation**

Monodisperse elastische schillen:  
een 3D studie van vastzittende granulaire materie en microencapsulatie

(met een samenvatting in het Nederlands)

Proefschrift

ter verkrijging van de graad van doctor aan de Universiteit Utrecht op gezag van de rector magnificus, prof. dr. G.J. van der Zwaan, ingevolge het besluit van het college voor promoties in het openbaar te verdedigen op dinsdag 20 mei 2014 des ochtends te

10.30 uur

door

**Jissy Jose**

geboren op 10 april 1986 te Cochin, India

**Promotor:** Prof. dr. A. van Blaaderen

**Co-promotor:** Dr. A. Imhof

This thesis is part of the research program of the ‘Stichting voor Fundamenteel Onderzoek der Materie’ (FOM), which is financially supported by the ‘Nederlandse Organisatie voor Wetenschappelijk Onderzoek’ (NWO).

*'When you want something, all the universe conspires in helping you to achieve it.'*

*Paulo Coelho, The Alchemist*



# Contents

Chapter 1. Introduction	1
1.1 Soft materials	1
1.2 Jamming	2
1.3 Microencapsulation	4
1.4 Outline of the thesis	5
Chapter 2. Bulk scale synthesis of monodisperse, permeable microcapsules with diameters above $3 \mu\text{m}$	7
2.1 Introduction	8
2.2 Experimental Method	10
2.2.1 Materials	10
2.2.2 Methods	11
2.2.3 Characterization	14
2.3 Results and discussions	15
2.3.1 Turrax Homogenizer	15
2.3.2 Prehydrolysis and Reshaking	18
2.3.3 Seeded growth - <i>DMDES</i>	19
2.3.4 Seeded growth - Hydrocarbons and silicone oil	20
2.3.5 Conventional method - droplet shearing	26
2.4 Conclusions	27
2.5 Acknowledgments and contributions	28
Chapter 3. Unloading and reloading microcapsules with apolar solutions by controlled and reversible buckling	29
3.1 Introduction	30
3.2 Experimental section	32
3.2.1 Materials	32
3.2.2 Methods	33
3.2.3 Characterization	34
3.3 Results and discussions	34
3.3.1 Controlled Buckling/Release	34
3.3.2 Reversed Buckling/Loading	40
3.4 Conclusions	47
3.5 Acknowledgments	47
Chapter 4. 3D image processing on jammed packings of monodisperse elastic shells	49
4.1 Introduction	50

4.2	Confocal microscopy	52
4.2.1	Sample preparation	52
4.2.2	Image acquisition	53
4.3	Image processing	53
4.3.1	Edge detection	54
4.3.2	Shape determination and fitting	56
4.3.3	Centroid and radius determination	58
4.3.4	Dimple detection	61
4.4	Conclusions	63
4.5	Acknowledgments	63
Chapter 5. 3D microstructure and contact forces in jammed packings of elastic shells - static compression		65
5.1	Introduction	66
5.2	Experimental Method	67
5.2.1	Sample preparation	67
5.2.2	Image analysis	68
5.3	Results and discussions	70
5.3.1	Microstructure of compressed shells	70
5.3.2	Contact forces in compressed shells	79
5.4	Conclusions	94
5.5	Acknowledgments	95
Chapter 6. 3D microstructure and contact forces in jammed packings of elastic shells - shear		97
6.1	Introduction	98
6.2	Experimental method	98
6.2.1	Sample preparation	98
6.2.2	Data acquisition and image analysis	100
6.3	Results and discussions	103
6.3.1	Structure of deformable shells under shear	103
6.3.2	Contact forces under shear	105
6.4	Conclusions	110
6.5	Acknowledgments	111
Bibliography		113
Summary		123
Samenvatting		127
Acknowledgments		131

CONTENTS

ix

List of publications

133

About the author

134



# 1

## Introduction

### 1.1 SOFT MATERIALS

Most materials can be classified under three basic states of matter: solid, liquid and gas. Yet there is a range of materials that are composed of mixtures of two or more states; for example shaving cream is a mixture of a liquid and a gas, mayonnaise consists of liquid droplets in a liquid, pastes consists of solids and liquids. These types of materials are known as soft materials. Even single phase materials like polymers and granular materials can be included in this category. An important property of soft materials is that they are viscoelastic. That means, these materials exhibit both elastic behavior of a solid and the viscous nature of a liquid. For example a pile of shaving cream on a table can hold its shape and even support a small amount of weight, such as a piece of paper. Upon increasing the weight, the pile deforms slightly, but it regains its shape when the weight is removed. If the weight added is too much the pile flows and does not return to its original shape even when the weight is taken away, the deformation is plastic or irreversible. Thus, foam possesses a yield stress. If the applied stress is below the yield stress, the foam behaves like an elastic solid, but if the applied stress is above the yield stress, the foam flows like a fluid. This solid-like to liquid-like transition or vice versa is a common behavior of soft materials like colloids and granular materials.

Colloids [1,2] are suspensions of small solid particles dispersed in a solvent. The size of the colloidal particle ranges from a few nanometers to several micrometers. Colloidal particles in dispersion undergo Brownian motion, random motion resulting from their collision with the solvent molecules. In physics colloids are an interesting model system for atoms and molecules. The forces that govern the structure and behavior of atoms are also present between colloidal particles, but due to their larger length and time scales compared to atomic systems they are relatively easy to study experimentally using microscopy or scattering techniques. They can form different phases: fluid, crystal and glass, depending on the volume fraction and interparticle interactions [3]. Colloidal

hard sphere glasses have many similarities to molecular glasses and hence the former is also a popular model system to study the glass transition [4–8].

Unlike colloids, in granular materials the grains are so big that their thermal energy is small compared to the gravitational energy. Typical examples include sand, snow, nuts, rice *etc.*. Another key feature that differentiates granular materials from colloids is friction, which is present between the touching grains. Due to friction and the lack of thermal energy granular materials are most often found in a solid state. However, they can behave like a liquid or gas under an external input energy, like an applied stress. An example is the behavior of sand; sand behaves like a solid when standing on it, but behaves like a fluid in an hourglass and like a gas when it is shaken. Granular materials are commercially important in areas as diverse as pharmaceutical industry, agriculture, and construction. A good understanding of the physics of granular materials is desired, for example, to predict and control landslides and avalanches [9,10], to design efficient transport and handling of coal or chemicals [11,12] and to make high quality tablets (medicine), i.e. the correct amounts of active and inert ingredients [13, 14]. Unfortunately, there still remains a poor understanding of the behavior of granular matter [15–17].

## 1.2 JAMMING

The term jamming refers to the phenomenon where constituent particles, whether they be molecular, colloidal or granular, in their disordered state are arrested in a small region of phase space with no possibility of escape. The stress relaxation time in jammed systems exceeds the experimental time scale and the material develops a yield stress [18,19]. Below the yield stress the system is jammed and behaves like an elastic solid and above this stress the system is unjammed and can flow like a liquid.

This transition from freely flowing to a jammed state, known as jamming transition, is achieved in various systems by tuning different control parameters. Granular materials jam as the driving force is lowered, emulsions and foams jam as shear stress drops, colloidal suspensions of small particles jam as the packing density is increased and supercooled molecular liquids jam as the temperature is lowered. Despite the significant differences in the physical origin of jamming in different systems, there are many features that they have in common, such as spatially heterogeneous dynamics at the onset of jamming [7, 20–22], dramatic increase of relaxation time [23–25] and emergence of a spatially heterogeneous force network [19, 26–28].

In 1998 Liu and Nagel [29] proposed a jamming phase diagram that brings all the soft matter systems in one framework, figure 1.1A. The coordinates in the phase diagram that control the transition from liquid-like (unjammed) to solid-like (jammed) state or vice versa are the temperature ( $T$ ), inverse packing density or volume fraction ( $1/\phi$ ) and the applied load ( $\Sigma$ ). The states, which lie within the curved surface are jammed,

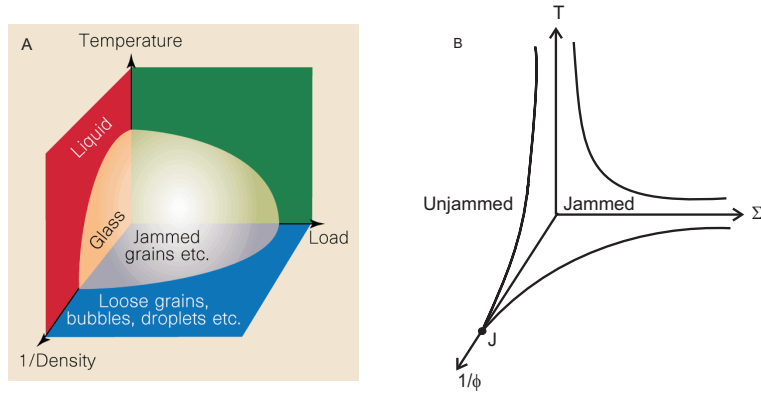


FIGURE 1.1. Jamming phase diagram; for sufficiently small temperature ( $T$ ), inverse density ( $1/\phi$ ) and applied stress ( $\Sigma$ ) the system is in the jammed state; A) classical diagram, reprinted by permission from Macmillan Publishers Ltd:[Nature] [29], copyright (1998) and B) revised diagram based on reference [30].

and those outside are unjammed. The temperature - inverse density plane represents the phase transition of supercooled liquids to glass that occurs at a glass transition temperature  $T_g$ . Glass transition is density dependent: as the density is lowered,  $T_g$  normally decreases. The phase diagram for foams, emulsions and granular materials would be the inverse density-applied load plane. At a fixed packing fraction, the system unjams if the applied stress is higher than the yield stress.

Later, the phase diagram was revised [30] (figure 1.1B) with a change in the curvature of the transition line based on the experiments performed by Trappe *et al.* [31] on attractive colloids. The new curvature implies that a material can be kept in a jammed state at a high density, even if the temperature is raised dramatically. The same applies if the material is at sufficiently low temperature and high density, it remain jammed even at high applied stress. The point  $J$  reflects the volume fraction of systems with repulsive interactions at zero temperature and zero applied stress below which the spheres do not touch each other and above which spheres start to overlap.

A significant feature of jamming in granular matter is the force network. When granular materials jam, the grains exert a force on each other and the stress is found to be inhomogeneously distributed throughout the system [19, 32, 33]. The collection of all contact forces form a force network which is typically characterized by the probability distribution of contact forces  $P(F)$ . Various experimental and theoretical approaches have been used to study contact forces in granular matter. A similar distribution of contact forces has been seen in simulations and experiments in other soft matter systems like glass, emulsion and foam [26–28]. Therefore  $P(F)$  is considered a universal property of jamming.

In this thesis we introduce spherical particles with a solid elastic shell to probe the jammed packings in a systematic and quantitative way. Note that all experiments

reported in the thesis are performed in the  $(1/\phi-\Sigma)$  plane. The size of the particles is several micrometers with a shell of thickness a few tens of nanometer. The mechanical behavior of the shells, depending on the ratio of shell thickness to particle radius, can be varied from soft and floppy to stiff and hard. Measuring the magnitude of shell deformation gives access to the contact forces between touching particles. Besides, due to the softness of the shells higher volume fractions close to unity are achievable, similar to other soft systems like foams and compressed emulsions.

### 1.3 MICROENCAPSULATION

In contrast to the deformation of particles with an elastic shell under a localized force in a jammed state, the shells in a dilute state, where they are not touching each other, can undergo a similar deformation when subjected to an isotropic pressure. This results in a reduction in their volume by the release of material from inside without causing any damage to the shell. The elastic restoring force of the shell further allows the particles to regain their original volume (shape) by refilling with different materials. Thus the elasticity of the shells make these particles a useful candidate for microencapsulation applications.

In general micron sized particles with a shell topology form a system that is extensively used in many industrial applications. These particles are commonly denominated as microcapsules. Due to their inherent properties, such as small size, wall permeability, mechanical stability, large inner volume and tunability, they are widely used as encapsulant to protect materials from environmental influences, as drug delivery vehicles for the sustained and targeted release of drugs, as microreactors and in catalysis. The most versatile approach of microcapsule fabrication available today is the templating technique, where a shell, mostly a polymer, is coated around a sacrificial template which is followed by template removal [34–40]. Efficient loading of cargo in microcapsules is extremely important in any of the above mentioned applications. The two popular methods of encapsulation are preloading of cargo onto the template [41, 42] and the postloading in preformed capsules [43, 44]. The choice of the method strongly depends on the nature of both the template and the cargo and moreover the permeability of the shell. Preloading has the advantage of efficient loading but finding a compatible template and cargo is an issue. On the other hand, in postloading compatibility is less relevant but encapsulation efficiency can be rather low.

Besides having an efficient encapsulation method a good release strategy of cargo is equally important in many applications. A sudden and complete release of cargo is achieved by rupturing of shell through an applied shear or pressure [45]. Another, more subtle method would be the diffusion of material through the shell without causing damage to the shell [46]. Nowadays responsive shells are gaining huge attention for targeted and sustained release of encapsulated materials in drug delivery. For this

purpose the capsule wall or shell is functionalized with compounds that are sensitive to external stimuli. A huge amount of research is devoted in this direction mainly on polymer capsules made by layer-by-layer technique [47–49]. In this thesis we describe an efficient encapsulation and release mechanism implemented in preformed elastic shells, where the shell is a semipermeable flexible membrane, for applications in the direction of microencapsulation.

## 1.4 OUTLINE OF THE THESIS

This thesis focusses on two, admittedly rather different, applications of spherical elastic shells. First (based on chapter order) in the field of microencapsulation as a smart container to encapsulate and release functional materials. Second, in jammed matter research as a model system to probe the microstructure and contact force networks in jammed packings, in a disordered state. What unites these two subjects is that they both depend upon the reversible elastic response of the shells: in microencapsulation this response allows loading and release to take place, while in granular matter the response allows the shells to act as sensors of the local stress. The thesis is structured as follows: in chapter 2 we describe the synthesis of stable spherical shells of size larger than  $3\ \mu\text{m}$ . They are prepared on a bulk scale with high monodispersity and fluorescently labeled for real space studies using a confocal microscope. The synthesis is based on an emulsion templating technique in which a solid shell of tetraethylorthosilicate (*TEOS*) cross-linked with dimethyldiethoxysilane (*DMDES*) is coated around liquid droplets, in our case polydimethylsiloxane (*PDMS*) oil droplets. Various robust methods to make monodisperse *PDMS* droplets are also discussed in this chapter. In chapter 3 we explore the possibilities of capsules filled with *PDMS* oil in microencapsulation applications like drug delivery. We propose a new method to efficiently unload and reload preformed capsules with apolar liquids that can contain fluorescent tracer molecules. The morphological changes that the capsules underwent during these processes were monitored and analyzed both qualitatively and quantitatively for a range of capsules with different ratio of shell thickness to radius.

Further chapters deal with the quantitative study of the amorphous structure and contact force network in jammed packings of elastic shells. Instead of capsules filled with *PDMS* oil we have chosen shells with an empty core for these studies. By empty core we mean that the liquid inside and outside the shell remain the same; in our system it was an index matched solvent. Chapter 4 addresses the first stage of quantitative analysis, that is, the image processing. The 3D coordinates and radii of the deformed shells in jammed packings were identified with sub pixel resolution using ImageJ algorithms. In jammed packings the shells were deformed in such a way that one of the shells formed a dimple and the other remained spherical upon contact. On the whole the volume of the shells was not conserved in a jammed state. This chapter also covers a way to identify

the shell that contains a dimple and hence the number of dimples per particle, which is a unique property of these packings. Having the knowledge of positions and radii of the shells we moved on to studying the geometry of the packings and the contact forces between pairs of shells, and hence the force network under static compression and shear, respectively, in chapter 5 and 6. Chapter 5 presents a detailed analysis of jammed packings as a function of their distance to the jamming transition from higher volume fractions. Chapter 6 briefly describes the effects of shear deformation on the anisotropy in the geometric structure as well as contact force distributions in jammed shells at a volume fraction above random close packing.

# 2

## Bulk scale synthesis of monodisperse, permeable microcapsules with diameters above 3 $\mu\text{m}$

We report several convenient methods to prepare monodisperse polydimethylsiloxane (*PDMS*) droplet templates in the size range 3-8  $\mu\text{m}$  for microcapsule synthesis in a high yield and discuss their pros and cons. The oil droplets are formed by the base catalyzed hydrolysis and condensation of the monomer dimethyldiethoxysilane (*DMDES*). To prepare these *PDMS* droplets we used various methods: introducing a Turrax homogenizer for the effective mixing of the monomer, prehydrolysing the monomer, shaking of a preformed polydisperse emulsion and finally via a seeded growth technique. In the seeded growth procedure, the *PDMS* droplets were exposed to hydrocarbons or a silicone oil. Depending on the water solubility of the second oil, the seed droplets showed swelling or de-swelling behavior. The template droplets, obtained from these different methods, are subsequently encapsulated in an elastic shell. The shell was formed by the co-polymerization of silane monomers *DMDES* and tetraethylorthosilicate (*TEOS*) via a post-addition method, in the presence of poly(vinylpyrrolidone) (*PVP*) stabilizer that prevented capsule aggregation.

## 2.1 INTRODUCTION

The synthesis of microcapsules represents an active field of research because they can potentially encapsulate, protect and distribute materials. As a result, there is a compelling fundamental as well as industrial interest for which the latter field is as diverse as food science, pharmaceuticals, cosmetics, biotechnology, the paint industry and advanced materials in general [37, 41, 50–55]. The most versatile approach for capsule synthesis is a templating technique. In this technique a shell is formed around a sacrificial particle via methods like interfacial polymerization [34], polymer precipitation by phase separation [35, 36], layer-by-layer self assembly [37, 56] or via locking of interfacial colloids [38] followed by removal of the core. For the sacrificial core, solid particles as well as liquid droplets have been used. An important advantage of the use of solid template particles (like silica, latex or gold colloidal particles) [57–60] is that it allows for a large scale synthesis of monodisperse cores in a wider range of sizes. However, after deposition of the shell material, relatively harsh dissolution or heating conditions are needed to remove the template. This complicates the production process and affects the quality and robustness of the as-prepared particles negatively [61, 62]. On the contrary, liquid template droplets allow for a more facile removal of the core under milder conditions [63, 64]. However, a combination of bulk scale synthesis and monodispersity is scarce when using liquid templating droplets [61, 65]. In conventional methods like ultrasonication [66, 67] and high-shear emulsification techniques [68–70] emulsion droplets are prepared in a large amount but with a wide size distribution. The reverse is true for droplets prepared using microfluidics, which allows for an exquisite degree of control over droplet size and composition but for which the production rate, and thus yield, is low [71–74]. In general, a high control over the capsule size distribution is required as the particle thickness and size sets the release rate [75–78]. As a result, there remains a need for an efficient method that can produce monodisperse template drops with well controlled sizes and size distributions.

An exception, where liquid droplets of high monodispersity and yield can be prepared, has been described by Vincent and co-workers [79]. As a result of a nucleation and growth process, a monodisperse polydimethylsiloxane (*PDMS*) emulsion formed by base catalyzed hydrolysis and condensation of the difunctional monomer dimethyldiethoxysilane (*DMDES*). The resulting droplets were stable against coalescence in the absence of added surfactant. Due to the high monodispersity, large scale production and facile drop removal, the liquid *PDMS* droplets have been used as sacrificial templates for the production of tetraethoxysilane-crosslinked-polydimethylsiloxane shells [39, 80], polydopamine capsules [81], colloidosomes [82] and even for polymer microspheres [83]. In all studies, the accessible size range was limited to about 0.6–3  $\mu\text{m}$  [39, 80, 81]. However, a wider size range is preferred in order for a capsule to act

as a transportation vehicle as the particle size has to nicely match the application in mind. For circulation and in vivo studies, nanometer sized capsules are for example required whereas larger particles allow higher loading capacity for in vitro studies [84]. Besides, the particle size controls the accessibility of the target location, especially in drug delivery. Particles smaller than  $0.2 \mu\text{m}$  can access bone marrow, capsules of  $1\text{--}5 \mu\text{m}$  are accessible through the air by inhalation and can be used to target antigen-presenting cells whereas capsules of  $5\text{--}15 \mu\text{m}$  can be used to target tumor tissues and spontaneously accumulate in lung capillaries [38,75]. Finally, the particle size determines the detection strategy that will be used during encapsulation and release studies. Ensemble assays are required for small particles based on for example UV-spectrophotometry [85] whereas detection on a single particle level is possible for larger (micron sized) particles in real time and real space with the confocal microscope [86–89]. Attempts to further increase the size of the *PDMS* droplet template, which predetermines the final size of the capsule, did not produce promising results yet. In principle, the droplet size can be varied up to  $5 \mu\text{m}$  by increasing the ammonia solution concentration. However, dynamic light scattering measurements on systems in which the droplet size was greater than  $1 \mu\text{m}$ , showed them to be more polydisperse [79]. Other means to tune the droplet size up to several micrometers, is by increasing the *DMDES* monomer concentration [79, 81, 90]. However, it was found to be difficult to prepare intact capsules for droplet diameters above  $2.4 \mu\text{m}$ , for which the initial monomer concentration had to exceed 3% v/v [79, 81, 90]. Another attempt to increase the capsule diameter was described in chapter 3 in which both *DMDES* and ammonia concentrations were higher than what has been used in reference [39]. However, this synthesis procedure was not found to be robust as it sometimes resulted in a polydisperse system. One can conclude that there is a lack of a sturdy synthesis procedure for monodisperse *PDMS* templating droplets, and hence capsules, with diameter exceeding  $3 \mu\text{m}$ .

The *PDMS* droplets can be coated with a *Tetraethoxysilane-crosslinked-PolyDiMethylSiloxane* shell to form *TC – PDMS* microcapsules. These capsules were synthesized for the first time by Zoldesi and Imhof [39], with sizes in the range  $0.6\text{--}2 \mu\text{m}$ . One advantage of *TC – PDMS* capsules, next to the monodispersity and size control, is the possibility to tune their shell thickness which is beneficial for potential encapsulation and release studies. In addition, the capsules were found to form anisotropic shapes upon drying, by simply tuning the ratio of shell thickness to droplet diameter [39, 90]. From an applied point of view these capsules have already shown promise because they are permeable to small polar dye molecules [90]. Recently our group (chapter 3) further extended the use of these capsules as containers by efficiently encapsulating and releasing apolar liquids, which can contain fluorescent tracer molecules, via controlled and reversible buckling. The capsules can even be loaded with surfactant molecules [91]. Besides, these capsules can be an interesting new model system to study the physics

of jammed matter [92], systems with slow relaxation dynamics, like granular materials, emulsions and foams [28,32,93], provided they are large enough. Not many experimental studies are performed in this direction due to the lack of imaging techniques that can see inside highly dense packings. As these capsules are highly flexible and can be index matched easily their jamming behavior can be quantitatively studied using real space confocal microscopy in 3D.

Herein, we introduce several methods to make monodisperse, stable *PDMS* droplets of sizes above 3  $\mu\text{m}$  in a high yield. The first method to make monodisperse emulsions is based on a modification of the *PDMS* synthesis as described in [79]. Here, we used higher *DMDES* concentrations as well as a Turrax homogenizer, for efficient mixing, during the nucleation stage of the oil-in-water emulsion. The second synthesis method is based on hydrolyzing the monomer prior to emulsion preparation. The third procedure is a seeded growth technique, in which we feed the primary *PDMS* droplets with more monomer *DMDES* or with oils like hydrocarbons and silicone oil. We further show that the oil droplets can be used as templates for the growth of a tetraethoxysilane-crosslinked-polydimethylsiloxane shell. In this way, we extend the range of particle diameters up to more than 5  $\mu\text{m}$  while maintaining the high yield, the high monodispersity, the surfactant free synthesis and facile drop removal. The size range is now comparable to the micron sized capsules [94] that are formed using microfluidic devices, but due to the broad diameter range the shells in the present study also allow miniaturization to sizes of a few hundred nm for a wider range of applications.

## 2.2 EXPERIMENTAL METHOD

### 2.2.1 Materials

Dimethyldiethoxysilane (*DMDES*, 97.0%), the triblock copolymer Pluronic P123 ( $(\text{PEG})_{20}-(\text{PPG})_{70}-(\text{PEG})_{20}$ , Mw - 5800), Tetraethylorthosilicate (*TEOS*, 98.0%), 3-aminopropyl-triethoxysilane (*APS*, 99%), rhodamine B- isothiocyanate (*RITC*), pyrromethene-567, polyvinylpyrrolidone (*PVP*, Mw-58000 g/mol), ammonia (25 wt%  $\text{NH}_3$ ), octamethylcyclotetrasiloxane (*OMCTS*,  $\text{C}_8\text{H}_{24}\text{O}_4\text{Si}_4$ ), cyclohexane ( $\text{C}_6\text{H}_{12}$ , 99.8%), iso-octane (99%) and hexadecane ( $\text{C}_{16}\text{H}_{34}$ , 99.0%) were purchased from Sigma-Aldrich. Ethanol (100%, technical grade) was obtained from Interchema and n-pentane (> 99% for spectroscopy) from Acros. Organically stabilized *CdSe/CdS/CdZnS/ZnS* nanoparticles (*QD's*) with a diameter of 6.9 nm were prepared by adapting the method of [95]. All chemicals were used as received. Demineralized water (resistivity 18  $\text{M}\Omega\text{cm}$ ) was used in all reactions and also for cleaning of glassware.

### 2.2.2 Methods

#### *Turrax Homogenizer*

(Large scale) We prepared monodisperse *PDMS* emulsion droplets by hydrolysis and condensation of the monomer *DMDES*, by modifying the original procedure of Vincent et al [79]. An aqueous dispersion (total volume 750 mL) of 22.7% v/v ammonia and 6.8% v/v of *DMDES* monomer was prepared in a 2 L beaker. Another typical sample (total volume 720 mL) was prepared at about the same ammonia concentration (23.7% v/v) but at a reduced *DMDES* concentration of 2.9% v/v. Directly afterwards, each sample was vigorously mixed using a Turrax homogenizer (IKA's Ultra-Turrax with a S25N 10G dispersing element) at a speed of 11,200 rpm. Mixing typically continued for 8-14 minutes, until the large *DMDES* droplets disappeared and small nuclei started to appear as seen under a light microscope. Hereafter, the turbid solution was poured into a 1 L flask and allowed to stand undisturbed for at least 2 days before the coating step.

(Small scale) Emulsion droplets were also prepared with the Turrax homogenizer on a smaller scale as compared to the above described procedure. An aqueous solution (total volume 29.9 mL) of 22.7% v/v of ammonia and 6.7% v/v of *DMDES* monomer was prepared in a 40 mL glass vial. Samples were vigorously mixed using the Turrax homogenizer at a speed of 11,200 rpm for about 4-5 minutes. Droplets were allowed to grow, while keeping the sample static, for at least 2 days.

Based on the work described in [39] fluorescent shells were grown around the as-prepared emulsion droplets. Before incorporation of the *RITC* dye into the shells, the coupling agent *APS* and dye *RITC* were covalently coupled by mixing 6.5 mg of the dye and 40  $\mu$ L *APS* with 1 mL anhydrous ethanol, after which this mixture was stirred for at least 12 h in the dark. The shell growth itself was modified when compared to [39] by introducing the steric stabilizer polyvinylpyrrolidone (*PVP*) onto the particle surface, in accordance with previous work done by Graf et al [60]. An aqueous solution (total volume 1725 mL) of 2.3 wt% *PVP* was prepared in a 2 L flask. Hereafter, 550 mL of the as-prepared emulsion (still containing ammonia) was added while gently stirring the sample. Inspired by the postaddition method introduced by O'Sullivan et al. [80], both *TEOS* (8 mL) and *DMDES* (8 mL) were added simultaneously during the shell growth step. The monomers were added slowly over time using a syringe pump (KD Scientific) (10  $\mu$ L/min). The *APS/RITC* dye solution (0.330 mL) was typically added 5 h after start of the shell growth. Shells were allowed to grow for at least 1-2 days, while gently stirring the sample, after which the *PDMS* template was removed by following the procedure below.

The dispersion containing the fluorescent shells was divided over small (40 mL) sample vials and centrifuged (800g for 30 min) after which the concentrated supernatant

was collected. The concentrated samples were dispersed in ethanol, which is known to penetrate the shells and to dissolve the liquid cores [39,90]. Shells were found to remain spherical in shape upon transferring about 100 mL of the concentrated dispersion in 2 L of (anhydrous) ethanol but started to buckle when the same amount of sample was dispersed in 1 L of ethanol. Often, samples were washed several times with ethanol in order to remove all *PDMS* oil.

#### *Prehydrolysed DMDES and reshaking*

In this method *DMDES* monomer was prehydrolysed prior to emulsion preparation by adding 2 mL of deionized water to 5 mL of *DMDES* monomer, which was taken straight from the bottle. The solution, with two immiscible liquids, was shaken in a vortex mixer (IKA minishaker MS2) at 2500 rpm for 5 min and then placed on a rollerbank to gently homogenize the mixture. By prehydrolysis the solubility of the monomer can be speeded up in the reaction medium. Monodisperse emulsions (total volume 11 mL) of *PDMS* oil droplets were prepared from *DMDES* that was either prehydrolysed for half an hour or for 24 h by adding 1 mL of hydrolysed *DMDES* (final concentration 6.5% v/v) to an ammonia solution (final concentration, 22.7% v/v) in a 20 mL glass vial. The reaction mixture was then mixed in with a vortex mixer for 3-4 minutes and then placed on a rollerbank during droplet growth.

An emulsion (total volume 10.8 mL) was also prepared without prehydrolysis of the *DMDES* monomer. Deionized water was added to 23.2% v/v of ammonia and 7.4% v/v of *DMDES* monomer in a 20 mL vial. The sample was vigorously mixed using a vortex mixer at about 2500 rpm for 4 minutes, after which it was placed on a rollerbank. Three hours after sample preparation, the dispersion was shaken once more by hand for 1 minute, after which the sample was positioned back on the rollerbank.

#### *Seeded growth - DMDES*

A suspension of monodisperse *PDMS* seed droplets (total volume 31 mL) of size 3.5  $\mu\text{m}$  was prepared by shaking (by hand) a mixture of 2.8 mL *DMDES* and 28.2 mL aqueous solution of ammonia (concentration of ammonia 22.7% v/v) in a 40 mL glass vial for 2 mins. The sample was placed on a rollerbank during droplet growth. The seeds were allowed to grow for 48 h after which the emulsion was transferred to a new vial (40 mL). We would like to note here that this sample was prepared in a glass vial where we used caps from manufactured by WHEATON that have a styrene-butadiene rubber liner. Whereas the samples that were closed with other caps, without styrene-butadiene rubber liner, often led to a polydisperse emulsion. The possible effects of capliner on size distribution is described in the thesis of Nina Elbers. For the seeded growth 2.8 mL of fresh *DMDES* was added to these seed suspension at once and the sample was kept on the rollerbank for gentle stirring. The addition of *DMDES* was repeated again at 120 h, 160 h and 216 h after the emulsion synthesis using the same

amount of *DMDES*. Each time an excess layer of oil (approximately 0.3 mL) was discarded by transferring the emulsion to a new vial.

#### *Seeded growth - Hydrocarbons and silicone oil*

For the seeded growth of *PDMS* droplets with a second oil, several seed emulsions were prepared using the Turrax homogenizer. Two samples were prepared according to the large scale Turrax method, but with reduced *DMDES* concentrations as described below. One sample was used to investigate the change in droplet size when exposing the as-prepared emulsion to various types of oil (sample A), whereas the other sample was only exposed to one type of oil, during which the particle size was monitored in time (sample B). Sample A (total volume 743.9 mL) was prepared in a 2 L beaker with an ammonia concentration of 22.9% v/v and *DMDES* monomer concentration of 6.0% v/v. Sample B (total volume 728.9 mL) contained 23.4% v/v ammonia and 4.1% v/v *DMDES*. The third monodisperse emulsion (sample C) was prepared according to the small scale Turrax method described above. This sample was used during swelling studies with fluorescently labeled cyclohexane. In all studies the droplets were allowed to grow, while keeping the sample without stirring or homogenization, for at least 2 days before starting the seeded growth procedure.

The preformed silicone oil droplets were grown larger using a seeded growth procedure with a second oil. The procedure for samples A and B was the following. Aqueous solutions (total volume 50 mL) of 2.7 wt% *PVP* were prepared. Hereafter, 20 mL of the original emulsion (still containing ammonia) was added, as well as 10 mL of the oil, which formed a layer on top of the emulsion. Various oils were used, including cyclohexane, pentane, iso-octane, hexadecane and octamethylcyclotetrasiloxane (*OMCTS*). The droplets in sample C were exposed to cyclohexane containing 0.28 mg/mL pyromethene-567. In order to do so, an aqueous solution (total volume 25 mL) of 2.7 wt% *PVP* was prepared. Hereafter, 5 mL of the original emulsion was added, as well as 3.5 mL of the fluorescently labeled oil phase. Droplets were allowed to grow, while keeping all samples slowly tumbling on a rollerbank for about 22 h (samples A and B) or 6 h (sample C).

The droplets resulting from the seeded growth in samples B and C were encapsulated by a solid shell by making use of the coating procedure described above for the Turrax method. However, a slight modification was needed as the current dispersion was already diluted with the *PVP* solution prior to start of the encapsulation. First, the sample was kept static for 5 min such that the excess oil phase creamed up. Subsequently, the turbid supernatant of the emulsion was transferred to a new vial such that the top oil phase could be avoided during the coating reaction. Hereafter, the *APS/RITC* solution was added (4  $\mu\text{L}$  for sample B and 2  $\mu\text{L}$  for sample C) while gently stirring the dispersion. Then, equal amounts (0.34 mL for sample B and 0.85

mL for sample C) of the monomers *DMDES* and *TEOS* were added using a syringe-pump (10  $\mu\text{L}/\text{min}$ ). The sample was transferred to the rollerbank after all monomer had been added. Shells were allowed to grow for a maximum of 24 h (sample B) or 3 h (sample C). The coated emulsion droplets in sample B were transferred to ethanol within 24 h after the start of the shell growth. Shells remained spherical when adding the sample drop-by-drop to (anhydrous) ethanol in a ratio of 1:8 mL, under vigorous stirring.

#### *Conventional method - droplet shearing*

An emulsion of *OMCTS* oil in water was prepared in a home built couette shear cell [96]. First, a crude emulsion of *OMCTS* droplets was made by mixing 2 mL of *OMCTS*, 1 mL of 0.17 wt% Triton X-100 surfactant solution and 8 mL deionized water in a vortex mixer and then shearing the sample at a shear rate  $2.00 \times 10^4 \text{ s}^{-1}$  in the couette shear cell. The resulting crude emulsion was again sheared at  $6.00 \times 10^4 \text{ s}^{-1}$  to obtain the final emulsion of *OMCTS* droplets of maximum size 15  $\mu\text{m}$ . For coating the droplets with a shell 6 mL of the obtained emulsion was added to 1 mL of ammonia solution (25 wt%  $\text{NH}_3$ ) and gently tumbled on rollerbank for homogeneous mixing. Afterwards, 48  $\mu\text{L}$  of *TEOS* and 48  $\mu\text{L}$  of *DMDES* were added and the sample was placed on rollerbank during shell growth.

### **2.2.3 Characterization**

#### *Static light scattering (SLS)*

The size and polydispersity of the *PDMS* oil droplets were determined by Static Light Scattering (*SLS*) experiments. The measurements were carried out in a home-built equipment using a *He – Ne* laser as light source (632.8 nm, 10 mW). The measurements were performed on dilute suspensions in de-mineralized water. The angular distribution of intensity of the scattered light was measured at scattering angles in the range  $14^\circ$  to  $135^\circ$  relative to the transmitted beam, with a photomultiplier detector mounted on a goniometer. The data were plotted against the scattering vector  $k = 4\pi n \sin(\theta/2)/\lambda$ , where  $n$  is the solvent refractive index and  $\lambda$  the wavelength in vacuum. By comparing the scattering profiles with theoretical ones calculated with the full Mie solution for the scattering factor, [97] the radius and polydispersity were determined. The positions of the interference minima in the scattering curves give the size of the droplets, whereas the polydispersity is given by the depth of the minima: the lower the polydispersity, the deeper the minima. The value of refractive index used to fit the experimental data for the oil droplets was 1.394, corresponding to the low molecular weight silicone oil [98].

#### *Confocal and optical microscopy*

The fluorescently labelled shells were imaged using an inverted Leica, TCS-SP2 Confocal Scanning Laser Microscope (63 $\times$  NA 1.4 oil immersion objective). A 543

nm green  $He - Ne$  laser was used for the excitation of rhodamine ( $RITC$ ) labelled shells and a 488 nm blue Argon laser was used for the excitation of pyrromethene 567 dye and of  $QD's$ . Samples were put in a capillary either  $0.1 \times 1$  mm or  $0.1 \times 2$  mm for imaging. Unlabelled oil droplets were observed using a Leica optical microscope ( $63\times$  NA 0.7 air objective).

#### *Atomic force microscopy (AFM)*

The thickness of the shell was measured using Atomic Force Microscopy ( $AFM$ , Digital Instrument, Nanoscope) in tapping mode. Samples for  $AFM$  were prepared by applying a drop of the hollow shells in ethanol onto a glass cover slide. The collapse of the shells, due to drying, leads to plateaus in the height profile that corresponds to twice the thickness of the shell.

## 2.3 RESULTS AND DISCUSSIONS

### 2.3.1 Turrax Homogenizer

Inspired by the method described in [79], low molecular weight polydimethylsiloxane ( $PDMS$ ) silicone oil-in-water emulsion droplets were synthesized by the base-catalyzed hydrolysis and polymerization of  $DMDES$ . We modified the synthesis procedure, by introducing a Turrax homogenizer for mixing and by using higher ammonia and  $DMDES$  monomer concentrations than what has been reported before by Zoldesi *et.al.* [39, 90]. The Turrax homogenizer helped to speed up the hydrolysis of added monomer and hence reduced the nucleation time for  $PDMS$  droplets, so that the droplets became monodisperse. Samples prepared in this way, became turbid about 8-14 min after start of the mixing, indicative for the formation of  $PDMS$  droplets. This happened faster when compared to the 1 hour time-scale described in [39, 79]. The position of the homogenizer-probe was found to strongly affect the monodispersity of the droplets, most likely because mixing variations affect the homogenization and hence the nucleation and growth procedure. A probe position close to the interface was found to be most successful. The samples had to be kept static after mixing. Samples that were kept on the rollerbank became polydisperse. This latter problem can (most likely) be attributed to the small amount of unreacted  $DMDES$  which could result in the formation of secondary nuclei and could also affect the charge stabilization of the as formed emulsion upon hydrolysis. Apparently, the tumbling motion caused by the rollerbank pronounced these effects, making the method less reliable than the static procedure. An indication that the system is indeed really sensitive to subtle changes in the amount of  $DMDES$ , is that both methods resulted in polydisperse systems when the overall monomer concentration was increased to higher values than what has been reported in the experimental section. When taking this into account, the method resulted in a high yield of highly monodisperse and micron sized oil droplets.

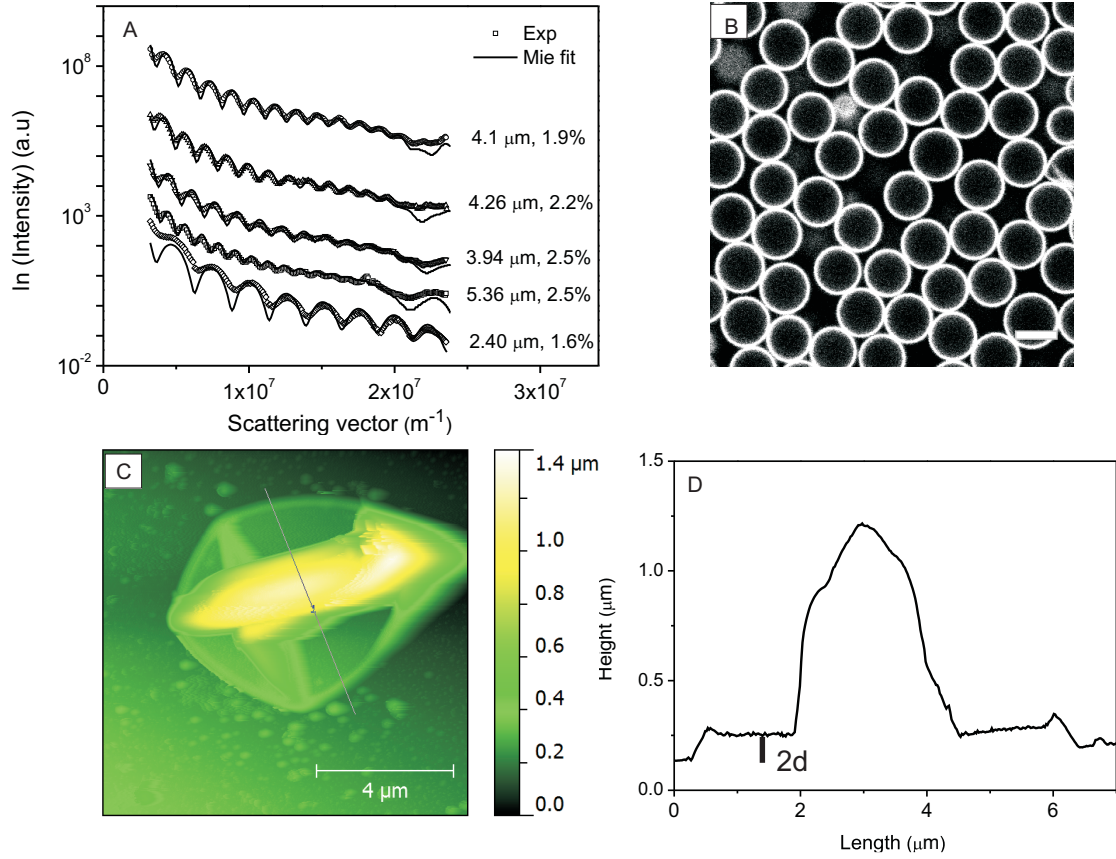


FIGURE 2.1. (A) *SLS* experimental data (scatter) fitted by theoretical calculations with full Mie solution of the form factor (lines) for different series of *PDMS* droplets prepared using the Turrax homogenizer, all after 3 days of preparation. In all samples the concentration of ammonia was 23% v/v and of *DMDES* was 6.8% v/v. The only exception was the emulsion with 2.4  $\mu\text{m}$  droplets which was prepared at a reduced *DMDES* concentration of 2.9% v/v. (B) Confocal micrograph of the 5.36  $\mu\text{m}$  microcapsules in an index matched solvent. (C) *AFM* image of these dried capsule, after removing the *PDMS* core by washing with ethanol. (D) The height profile taken along the line drawn through the collapsed capsules from which we measured a shell thickness of 56 nm.

Four batches of droplets were prepared at an ammonia concentration of 23% v/v and *DMDES* concentration of 6.8% v/v, and one more batch at a reduced *DMDES* concentration of 2.9% v/v. The many well-defined minima in the static-light-scattering (*SLS*) curves in figure 2.1A are indicative for the high monodispersity in these large scale (750 mL) suspensions. The size and polydispersity of the droplets could be obtained by comparing the scattering profiles with theoretical ones calculated using the full Mie solutions for the scattering form factors [97]. The fits showed that the droplet

diameters and polydispersities varied slightly between the four different batches (with a *DMDES* concentration of 6.8% v/v) after 3 days of droplet growth, in the range 4-5.4  $\mu\text{m}$  and 2-2.5 % respectively. This result indicates that the synthesis procedure generates droplets that are similar in size as the upper limit reported in [79] ( $\sim 5 \mu\text{m}$ ). However, the deep minima in the *SLS* profiles prove that the polydispersity remains significantly lower in the current system. When reducing the *DMDES* monomer concentration from 6.8 to 2.9% v/v, the droplet diameter decreased to 2.4  $\mu\text{m}$ , figure 2.1A. Earlier studies have also shown a similar relationship between droplet size and monomer concentration [79, 81, 90].

All samples prepared with the small scale method also resulted in monodisperse emulsions. Using *SLS*, the droplet sizes were determined for two batches after 2 days of droplet growth. The droplet diameter and polydispersities were found to be 2.8  $\mu\text{m}$  and 1.7  $\mu\text{m}$  and 1.9% and 1.8%, respectively. One can conclude that these sizes were reduced when compared to the large scale procedure that uses the same concentration of ammonia and *DMDES*. The absence of an excess *DMDES* phase after mixing as well as a more effective homogenization in general for smaller amounts of emulsions can most likely be the cause of this difference. Such a strong influence of the emulsion amount and the mixing procedure on the particle size has also been reported by [90].

Tetraethoxysilane-crosslinked-polydimethylsiloxane shells were grown around the monodisperse, template droplets prepared with the large scale Turrax procedure. The cross-linked network of silica and siloxane units formed upon addition of both the monomers *DMDES* and *TEOS*, in accordance with previous work done by O’Sullivan et al [80]. However, shells were found to form small aggregates during the coating step, likely caused by van der Waals attractions between these micron sized particles. In order to prevent this, we modified the procedure slightly by diluting the emulsion with a *PVP* solution prior to addition of the monomers as described in the experimental section. Such an adsorbed layer of *PVP* is known to stabilize colloidal particles in water [60]. On a trial-and-error basis, the concentration of *PVP* was increased to 2.3 wt%, such that aggregation was reduced considerably. Shell growth typically continued for about 2 days, after which the liquid templating drop could be removed by transferring the coated droplets to ethanol. The procedure for this solvent transfer is described in the experimental section. A concentrated dispersion of ethanol filled microcapsules could be index matched (refractive index = 1.42) in a 52.6% v/v dimethyl sulfoxide (*DMSO*) and 47.4% v/v ethanol solution. A confocal micrograph of such a system formed around a 5.36  $\mu\text{m}$  templating droplets, is given in figure 2.1B. The shell thickness of the capsules in this sample was measured by taking cross-sectional profiles through atomic force microscopy (*AFM*) height images, as shown in figure 2.1C and D. Using this procedure, the shells were found to be about 56 nm thick. We can therefore conclude

that we can grow stable *TC* – *PDMS* capsules around *PDMS* template droplets with diameters exceeding the limit of about 3  $\mu\text{m}$  that has been reported before [80,90].

### 2.3.2 Prehydrolysis and Reshaking

Another method to synthesize monodisperse *PDMS* oil-in-water emulsions is using prehydrolysed *DMDES*. Prehydrolysis makes the monomer readily soluble, so that the nucleation time may be reduced, leading to more monodisperse droplets. Prehydrolysis, prior to emulsion preparation was done by mixing 28.5% v/v of water and 71.5% v/v *DMDES*. Before mixing, the solution formed two phases, as *DMDES* is insoluble in water. But within half an hour it became a clear single phase, indicating the hydrolysis of the monomer. Two batches of emulsions were prepared with 9% v/v of half an hour old prehydrolysed *DMDES* (final concentration of *DMDES* was 6.5% v/v) and 22.7% v/v of ammonia by shaking (vortex mixer). The samples were placed on a roller bank to gently tumble the mixture during droplet growth. After 24 h of synthesis, both batches contained monodisperse *PDMS* oil droplets of diameter 5.6  $\mu\text{m}$  and 5.0  $\mu\text{m}$  with polydispersity 2% and 1.9%. These sizes are comparable to those obtained using the Turrax homogenizer. On the contrary, we found that emulsions made without prehydrolysis of monomer under otherwise identical conditions often became polydisperse. This result is therefore also in agreement with the adverse effect of the excess *DMDES* phase that was described above for samples prepared with the Turrax homogenizer which were gently tumbled during droplet growth instead of being kept static. Apparently prehydrolysis reduces the amount of unreacted *DMDES* in the sample that can adversely affect the size distribution of droplets.

However, we noticed that prehydrolysis for a longer period reduces significantly the size of the *PDMS* droplets. Two batches of emulsions, each prepared using a 24 h old prehydrolysed *DMDES*, contained droplets of diameter 1.7  $\mu\text{m}$  and 2.0  $\mu\text{m}$  with polydispersity 2.9%. Although still monodisperse the average droplet size was reduced approximately by 60% compared to the droplets prepared from a half hour old prehydrolysed *DMDES*. It is likely that the aging of hydrolysed monomer results in an increase in the concentration of water-soluble oligomers in the sample and hence that the nucleation rate is increased. The same volume of oil is now distributed over more nuclei, which results in smaller droplets. A similar size decrease was observed earlier in the presence of added surfactant [99,100], where the droplet size decreased with increasing surfactant concentration. The prehydrolysis of the monomer can perhaps happen in the bottles where *DMDES* monomer is stored. Each time when the bottle is opened for preparation moisture in the air can likely initiate hydrolysis of monomer. Although this is a small amount, the effects of hydrolysis might become prominent over a longer period (1 or 2 years).

A monodisperse oil-in-water emulsion could also be prepared when shaking the samples by hand instead of using the Turrax homogenizer or without prehydrolysing the *DMDES* monomer. Samples were prepared at a slightly higher *DMDES* concentration (7.4% v/v) and ammonia concentration (23.2% v/v) when compared to the Turrax synthesis procedures. Three hours later, the emulsion became polydisperse containing droplets of maximum size 4-6  $\mu\text{m}$ . At this stage the dispersion was shaken once more by hand for one minute. Samples without this second shaking step remained polydisperse during droplet growth, as indicated by the lack of well-defined minima in the *SLS* profile (result not shown). Whereas samples that were shaken once more after 3 hours became monodisperse. Two batches of emulsions, both 3 days old, were found to be 2.1  $\mu\text{m}$  and 3.0  $\mu\text{m}$  in diameter and both had a polydispersity of 1.6%. These droplets were smaller compared to what has been obtained with the Turrax homogenizer. We would like to note that the time-interval for the second shaking step was not found to be critical. For example, reshaking the polydisperse emulsion after 3 days still resulted in a monodisperse emulsion. The droplets were found to become 2.46  $\mu\text{m}$  in diameter with a 1.6% polydispersity, as determined with *SLS*, 5 days later. A similar scenario was observed for another sample which was reshaken after 2 days. The effect of the second shaking step is puzzling. Possibly by reshaking, new nuclei were formed from the short linear oligomers and any unreacted *DMDES*. These linear species, formed by the slow *DMDES* monomer reaction [90], are known to be surface active [101], so they might decrease the energy barrier for nucleation. As a result, nuclei were formed in a narrow time-window which leads to monodisperse, micron sized droplets upon further growth with left-over material. When comparing both methods, the prehydrolysis and reshaking, one can conclude that the synthesis scale could not (yet) compete with the Turrax procedure. However, both routes produced droplets that were larger than what has been reported in [90] and of the order of what has been achieved so far [79, 80].

### 2.3.3 Seeded growth - *DMDES*

More *DMDES* was used to increase the size of the *PDMS* droplets, similarly to the seeded growth of silica colloids [102]. The amount of *DMDES* that was added during the seeded growth step, was the same as what has been used during the preparation of the seed/original suspension. Seeded growth was performed for 9 days during which the monomer was added four times with a time intervals of 48 h, except for the second addition. The sample was placed on a rollerbank during droplet growth. Figure 2.2A shows the *SLS* curves of seed droplets taken just before the first and last addition of monomer. We measured an increase of droplet size from 3.48  $\mu\text{m}$  to 8.00  $\mu\text{m}$  from the scattering profiles. The growth of the droplets followed in time after each addition is shown in the plot figure 2.2B, where the points marked in red represent the time of addition of monomer. The data point at 0 h represents the time of preparation of the

seed emulsion. A major increase in size of the seed droplets, approximately 0.5  $\mu\text{m}$  occurred during the first 24 h of growth; thereafter the growth was rather slow. The droplets were found to remain stable and monodisperse up to 8.00  $\mu\text{m}$ , even in the presence of more monomer. The stability of the droplets can be attributed to factors like the increase in surface area and hence surface charge [79] and the surfactant like behavior of linear *PDMS* chains [101]. However, after the last addition of monomer the emulsion became unstable and underwent coalescence. Although the size of the droplets can be increased by feeding with *DMDES* monomer, the size increase occurred on a much slower rate due to the slow condensation reaction of hydrolysed monomer [90]. So it would be interesting to search for oils where a similar or even larger size increase can be possible in a shorter time period.

### 2.3.4 Seeded growth - Hydrocarbons and silicone oil

Three batches of monodisperse *PDMS* emulsions were prepared for the seeded growth with a second oil. Droplets from sample A were exposed to various oils, whereas the increase in droplet diameter was followed in time for one type of oil in sample B. Sample C was used for a seeded growth procedure with a dyed oil phase. In all studies, the *PDMS* droplets were at least 2 days old before exposure to the commercial oils. This was required as the preformed *PDMS* droplets are known to increase slowly in time within the first 48 h [90]. An elapse of at least 2 days therefore allowed us to attribute any changes in droplet size to the exposure of the oil.

Monodisperse droplets formed in sample A with a diameter of 4.2  $\mu\text{m}$  and polydispersity of 2.1% after 2 days of growth. An optical micrograph of this sample is shown in figure 2.3A. The oil droplets were used in a seeded growth process by exposing the emulsion for 22 h to various types of oils, including cyclohexane, iso-octane, hexadecane and *OMCTS*. A significant size increase was observed in presence of cyclohexane, resulting in monodisperse droplets of about 8.5  $\mu\text{m}$  in diameter as can be seen in figure 2.3B. A smaller increase, resulting in diameters of about 5  $\mu\text{m}$ , was monitored for the sample with iso-octane (figure 2.3C). Droplets in both samples remained stable for a couple of days. When compared to the seeded growth with *DMDES* after a time period of about 24 hours (figure 2.2B), droplet size increased more rapidly for cyclohexane, and occurred at about the same rate for iso-octane. Besides, droplets could now be grown up to 8.5  $\mu\text{m}$  in diameter, without the need of successive addition steps. Continuing the seeded growth procedure with *OMCTS* (result not shown) and hexadecane (figure 2.3D), the droplet size was found to decrease and the number of oil droplets reduced. Besides, these systems became polydisperse and significantly less turbid, indicative of reduced sample stability and deswelling as will be discussed in more detail below. From these observations, one can conclude that the various oils affect both the stability and the size of the original *PDMS* seed droplets.

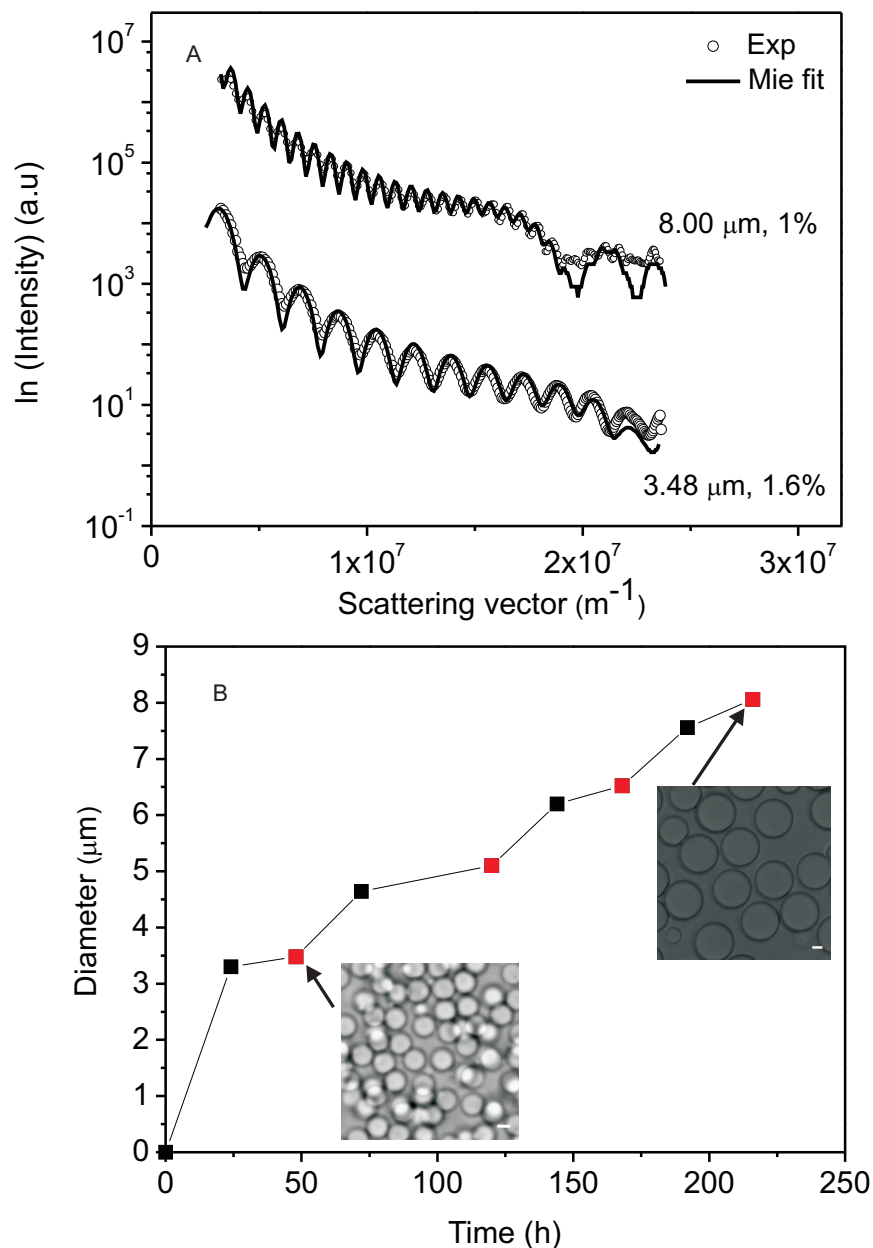


FIGURE 2.2. (A) *SLS* profile of *PDMS* droplets. Using a seeded growth procedure with *DMDES*, the droplets were grown larger by adding more monomer at definite time intervals. (B) Increase of the droplets radius followed in time. Data points marked in red denote the time at which more of the monomer was added. Inset pictures are the optical micrograph of seed droplets just before first and last addition of more monomer. Scale bar represent  $2 \mu\text{m}$

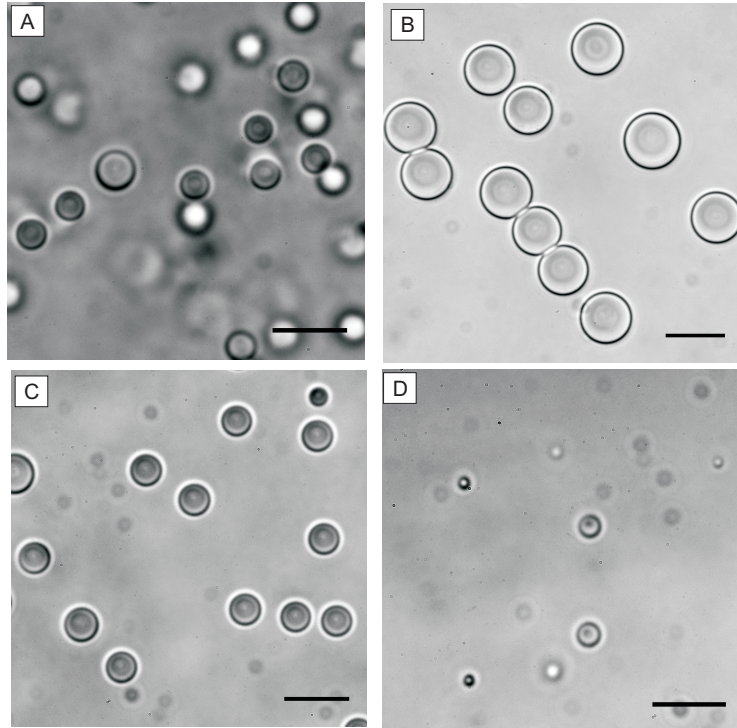


FIGURE 2.3. Optical micrographs of the original *PDMS* seed droplets (A) and of these droplets after 22 h of exposure to cyclohexane (B), iso-octane (C) and hexadecane (D). The droplet size was found to vary, depending on the solubility of the hydrocarbon oil in water. Scale bars denote 10  $\mu\text{m}$ . The appearance of a core-shell structure is caused by the refractive index mismatch.

A study by Neumann [101] is related to the stability of the droplets. They conducted droplet lifetime measurements on mixtures of synthesized *PDMS* and n-heptane. Stable droplets could be formed in pure water, in absence of any added surfactant, at a volume fraction of *PDMS* greater than 0.25. This stability was attributed to the linear chains in the synthesized *PDMS* oil that can act as surfactants as evidenced by interfacial tension measurements. It was postulated that the linear chains hereby can give rise to an enhanced Gibbs elasticity of the interface. A similar scenario could explain the stability of droplets swollen with cyclohexane and iso-octane in the present study even though the volume fraction of *PDMS* in the former mixture is as low as 0.124. In this context, it's surprising that droplets exposed to *OMCTS* were found to be unstable and to deswell. The interfacial tension of *OMCTS* oil is 40.1 mN/m and is therefore even lower than the 48.4 mN/m reported for the commercial n-heptane that could result in stable droplets when mixed with synthesized *PDMS* [101]. This therefore suggests that the system is also influenced by another factor which can, most likely, also explain the size dependence of the swollen *PDMS* droplets.

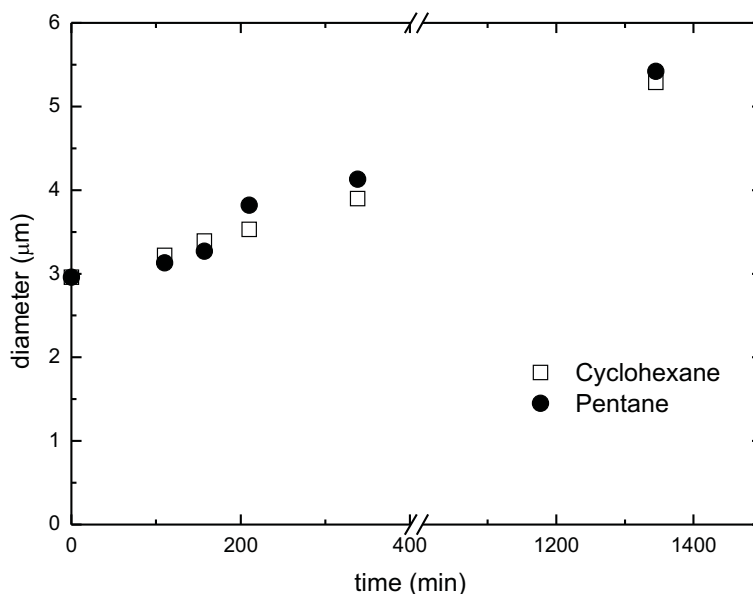


FIGURE 2.4. (A) Increase of the droplet diameter followed in time when exposing the sample to cyclohexane or pentane.

The rate of swelling of the original *PDMS* seed droplets, and hence the particle size, is most likely related to the solubility of the various oils in water. In general, the solubility of hydrocarbon in water decreases with increasing chain - length. This trend matches nicely with the observation that size increase was most pronounced for cyclohexane followed by iso-octane. The reverse, a decrease in droplet size, was observed for oils like hexadecane and *OMCTS* for which the oil solubility in water is poor [103]. It's likely that the threshold for successful swelling of the preformed emulsion is set by the solubility of the synthesized *PDMS* oil itself. Oils for which the solubility is higher than for *PDMS* result in a particle increase whereas the reverse, a decrease in droplet size, is occurring for oils poorly soluble in water. It's known that about 80% of the total material in the synthesized *PDMS* oil is comprised of the cyclic tetramer *OMCTS* [79]. The fact that swelling with *OMCTS* and hexadecane was found to be unsuccessful suggests that the linear oligomers, present in the synthesized *PDMS* oil, raise the water solubility of the preformed emulsion to values above that of these two oils. Along the same line of reasoning, it could furthermore be that these linear chains were withdrawn first from the as-prepared emulsion during the de-swelling process. A reduction in the number of these surface active molecules [101] could clarify why samples also became unstable in presence of poorly soluble oils, as indicated by the polydispersity and by the reduction in the number of droplets.

In another experiment, we exposed the droplets in sample B to one type of oil and monitored the increase in diameter over time with the optical microscope. The original *PDMS* droplets, 3 days old, were found to be  $2.96 \mu\text{m}$  in diameter with a polydispersity

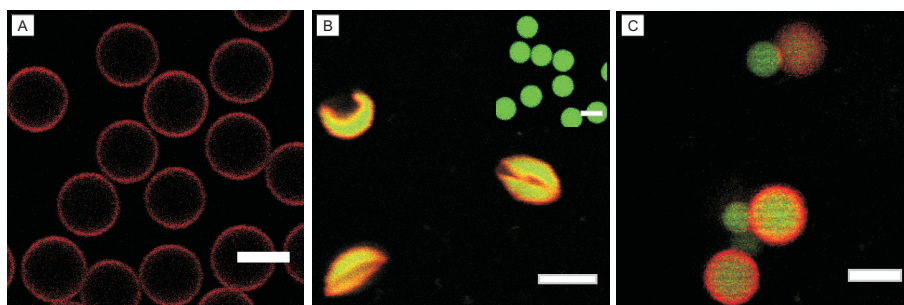


FIGURE 2.5. (A) Confocal micrograph of shells formed around cyclohexane swollen *PDMS* droplets, 24 h after the start of shell growth. (B) The preformed *PDMS* emulsion could be swollen with fluorescently labeled cyclohexane (inset). After encapsulation, shell buckling indicated that the volume of the templating droplets is not conserved anymore, 3 h after the start of shell growth. (C) Shells unbuckled, and then budded secondary droplets, in presence of excess cyclohexane due to overloading. Scale bars denote 5  $\mu\text{m}$ .

of 2%. One batch of these droplets was exposed to cyclohexane and another batch was exposed to pentane. The water solubility of pentane [104] is similar to that of cyclohexane [105]. Indeed, in both samples a similar increase of the particle diameter was observed as shown in figure 2.4, confirming the suggested relationship between droplet size and the oil solubility in water. After 22 hours, the droplets reached a diameter of 5.4  $\mu\text{m}$ , measured from optical micrographs. The diameter increase of about 50% is in good agreement with the increase reported for sample A which was also exposed to cyclohexane for the same amount of time.

The swollen droplets could be encapsulated by a solid shell. Again, an adsorbed layer of the steric stabilizer *PVP* was introduced around the droplet surface in order to prevent aggregation during the coating step [60]. For this purpose, the emulsion was diluted with the *PVP* solution prior to addition of cyclohexane or pentane. Even though the swollen droplets would remain stable in absence of polymer, this intermediate step was required as dilution at a later stage would result again in a decrease in size. This indicates that the continuous phase had to be saturated with oil in order to maintain a constant drop size during shell growth. When using this procedure, shells could be successfully grown around the 5.4  $\mu\text{m}$  cyclohexane swollen droplets as can be seen in figure 2.5A.

Spherical, ethanol-filled capsules could be obtained with this seeded growth procedure when shells were transferred to ethanol according to the procedure described in the experimental section. The shell thickness was found to be only 20 nm when taking cross-sectional profiles of *AFM* height images. Possibly, by increasing the amount of *DMDES* and *TEOS* during shell growth, thicker shells can be formed. However, the present study focused on the increase in the capsule diameter rather than control over

the shell thickness. Control over the latter parameter was already achieved in studies described by [39, 80, 90]. Besides, capsules with high diameter-to-wall thickness ratios can be interesting for potential applications [41].

If shells were not transferred to ethanol within about 24 hours of shell growth, the particles started to buckle in the reaction medium. First of all, buckling indicates that a solid shell has grown around the templating emulsion. Second, it also suggests that the volume of the templating droplets is not conserved anymore. In principle, such a decrease in volume was prevented as the continuous phase had been saturated with oil. These results therefore suggest that loss of oil possibly occurred via evaporation, even though the samples were sealed with a cap. An indication for this hypothesis is that samples swollen with pentane, which has an even lower boiling point than cyclohexane, buckled in a more pronounced way, and already within the first 24 hours. Leakage of oil might be prevented in further studies by exposing the aqueous dispersion to oil vapors. All the results above suggest that swelling of preformed *PDMS* droplets will be most successful for oils with a high water solubility and a high boiling point. Of course, in practice these two requirements tend to exclude each other.

An example of the buckling behavior due to loss of oil is shown in figure 2.5B, for shells formed in sample C. These shells were grown around *PDMS* droplets (3.2  $\mu\text{m}$  in diameter, polydispersity 2%, 5 days old) that were swollen to 5.5  $\mu\text{m}$  within 6 hours by exposure to stained cyclohexane. By labelling the cyclohexane phase with the dye pyromethene-567, the original droplets not only swelled but also became preloaded with the fluorescent dye. A confocal micrograph of this dyed emulsion is shown in the inset of figure 2.5B. Interestingly, unbuckling of the encapsulated droplets was possible by exposing the sample again to an excess phase of (dyed) cyclohexane. This could be achieved by filling half a capillary with the buckled shells from the reaction medium and the rest of the capillary with the (fluorescent) cyclohexane phase. Confocal micrographs of this system were taken near the oil-water interface soon after preparation of this sample. As can be seen in figure 2.5C, shells fully relaxed to spheres and even became overloaded with the oil phase resulting in the formation of a dumbbell. A similar observation is described in chapter 3 where the overloading with cyclohexane was attributed to the combination of the shell rigidity and a favorable mixing entropy of the oils. The present result also indicates that the system is still highly permeable to both oil and dye molecules, even though the shell synthesis is slightly altered when compared to that described in chapter 3 by introducing the polymer *PVP* and using the seeded growth procedure. When transferring buckled shells like the ones shown in figure 2.5B to ethanol, a deformed capsule was obtained. These capsules were slightly dimpled and their shape did not change 24 hours after transfer to ethanol. This therefore suggests that the particles were fixated in this shape, possibly because shell growth proceeded while the volume of the template had decreased. It's however striking that shells also

contained a small dimple in ethanol, after they had first been unbuckled with excess cyclohexane in the reaction medium. Possibly this spherical intermediate state was caused by a slight swelling of the capsule in presence of excess cyclohexane oil. This, combined with shell weakening during buckling in water or stretching upon exposure to oil, might also limit full relaxation to a sphere in ethanol. It's therefore important that shells are transferred to ethanol within the time-frame set by the onset of buckling. On a final note, it should be mentioned that buckling in sample C already occurred within 3 h after start of shell growth whereas this typically occurred after 24 h when samples were prepared according to the procedure of sample B, as discussed above. Possibly, this deviation is caused by the preloading with dye, a pronounced evaporation of oil due to the use of disposable sample vials or due to the increase in the *DMDES* and *TEOS* concentration in the former system, as described in the experimental section.

The above described preloading (with dye in the present study) could in principle result in high encapsulation efficiencies before droplet coating. One of the important benefits of microfluidic devices is for example that the chemical composition of the dispersed phase, and hence the encapsulation of actives, can be controlled by selecting the fluid that is introduced [74]. Unfortunately, preloading in the present system was not found to be successful when using cyclohexane in which 6.9 nm quantum dots were dispersed ( $1 \cdot 10^{-7}$  mol/mL). Even though the droplets did swell, the quantum dots remained dispersed in the phase separated (excess) cyclohexane phase. This result indicates that material can only be transferred to the monodisperse emulsion when the encapsulates are water soluble on the single particle level. In another experiment, surfactant micelles were introduced by adding 0.036 wt% of the surfactant P123. Initially, a mixture was formed between monodisperse, unloaded *PDMS* droplets and polydisperse, *QD*-loaded cyclohexane droplets. However, within 4 days, all droplets became polydisperse and unloaded droplets were still observed. Hence, *QD*'s could not be successfully transferred to the monodisperse, preformed *PDMS* emulsion based on this seeded growth procedure with cyclohexane in absence, as well as in presence, of surfactant micelle shuttles. However, a previous study by Cui et al [81] showed that cargo loading with *QD*'s is in principle possible during the formation of the monodisperse *PDMS* emulsion when dispersing the nanoparticles in the *DMDES* monomer.

### 2.3.5 Conventional method - droplet shearing

In addition to the above described methods we tried to make even larger templates and capsules. This was done by applying a shear force [70,96] on a crude suspension of surfactant stabilized oil droplets in water. The oil used for this experiment was the low molecular weight silicone oligomer octamethylcyclotetrasiloxane (*OMCTS*). The size of the droplets obtained by shear was in the range 3-15  $\mu\text{m}$ , quite polydisperse, as

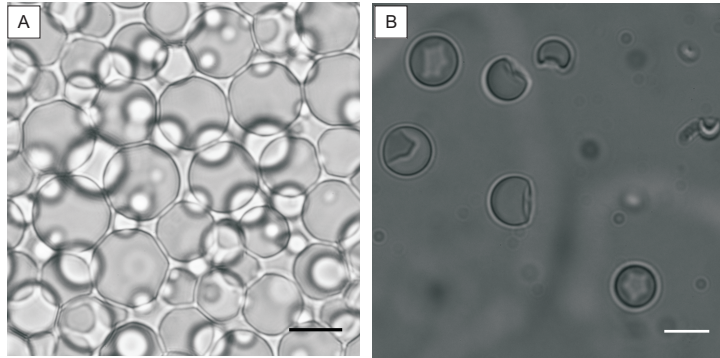


FIGURE 2.6. Optical micrograph of surfactant stabilized *OMCTS* emulsion droplets prepared by shear. (B) *OMCTS* droplets coated with *TC – PDMS* shell. The capsules buckled with a dimple due to the dissolution of *OMCTS* oil by surfactant micelles. Scale bars represent  $10\ \mu\text{m}$ .

shown in figure 2.6A. We coated these droplets with the tetraethoxysilane-crosslinked-dimethylsiloxane shell by adding *TEOS* and *DMDES* simultaneously, using the post addition method [101], figure 2.6B. However, this time we didn't use *PVP* to stabilize the capsules during shell growth. As a result the capsules underwent aggregation, even though all the capsules in the image are loose and stable. The presence of a solid shell was confirmed by adding a non-ionic surfactant (Pluronic P123) to the capsule suspension as described in chapter 2. The capsule was found to buckle with a dimple due to the volume decrease caused by the gradual dissolution oil by surfactant micelles. Note that this shear procedure of making template droplets is not a surfactant free method. Studies are underway to replace the surfactant with synthesized *PDMS*, as linear *PDMS* chains can likely impart the necessary stability to the droplets against coalescence [101].

## 2.4 CONCLUSIONS

In the present study, we have shown that we can synthesize capsules around monodisperse *PDMS* templating droplets above  $3\ \mu\text{m}$ . The shell material was formed by a tetraethoxysilane-crosslinked-polydimethylsiloxane network. The templating droplets are prepared via various methods. In one method, a Turrax homogenizer was used during the nucleation stage of the droplets, resulting in droplets (and hence capsules) with diameters above  $5\ \mu\text{m}$  in a bulk (750 mL) scale. In the second technique, the monomer was prehydrolyzed or the reaction medium was reshaken, confirming the need of a heterogeneous oil composition prior to nucleation of stable, micron-sized *PDMS* droplets. In the third method, preformed *PDMS* templates were swollen with *DMDES* monomer or with oils like hydrocarbons and cyclic silicone oligomer *OMCTS*

during a seeded growth procedure, resulting in monodisperse droplets up to 8.5  $\mu\text{m}$ . For swelling with hydrocarbons and silicone oligomer, the solubility of the oil has to be higher than that of the synthesized *PDMS*. Besides, the spherical capsules had to be transferred to ethanol before particles started to buckle in the reaction medium, limiting the duration of shell growth. Finally, large but polydisperse (up to 15  $\mu\text{m}$ ) capsules were grown around droplets that were prepared using a droplet break up shear procedure described in the literature [70, 96]. This latter experiment confirms once more the disadvantage of normal bulks scale emulsification techniques in which a large scale production is typically coupled with a wide size distribution. We therefore believe that the monodisperse droplets prepared with the other routes are interesting sacrificial templates in general, for synthesis of capsules above 3  $\mu\text{m}$ . They allow for a surfactant free synthesis procedure, high monodispersity and facile drop removal.

When comparing all procedures, it can be stated that the Turrax procedure currently allow for the largest scale synthesis of droplets up to about 5.5  $\mu\text{m}$  in diameter. When aiming for even larger droplets, the seeded growth procedures with *DMDES* or hydrocarbons are preferred. The main advantages of the hydrocarbon method are that the droplet size increases faster and no successive addition steps are required. Finally, the droplet size and synthesis scale of the prehydrolysis and reshaking methods can not yet compete with the Turrax and seeded growth routes. Overall, we think that the increased *PDMS* drop diameters broaden the horizon for potential applications and also allow the use of elastic shells for granular jamming/contact force studies.

## 2.5 ACKNOWLEDGMENTS AND CONTRIBUTIONS

This work was performed in close collaboration with Nina Elbers, who performed the experiments on seeded growth with hydrocarbons/silicone oil and reshaking. Together we developed the procedure for the Turrax homogenizer. This chapter was also written together. Mark Boneschanscher and Jaco Geuchies are thanked for their help with the *AFM* measurements on our capsules and Relinde Moes for providing the *QD's*.

# 3

## Unloading and reloading microcapsules with apolar solutions by controlled and reversible buckling

We introduce a new experimental method to encapsulate and release oils and fluorescent molecules, into preformed elastic microcapsules of polydimethyldiethoxysilane (*PDMS*) filled siloxane shells, which are crosslinked with tetraethoxysilane. The method uses controlled buckling, where the volume of the capsule is reduced by dissolving the *PDMS* oil inside the capsule by surfactant micelles. This results in a change in the morphology of the capsule that depends on the ratio of shell thickness to total particle radius ( $d/R_t$ ). Microcapsules of  $d/R_t$  in the range 0.007-0.05 formed microbowls upon decreasing the inner volume. The amount of oil released or dissolved by the micelles can be directly related to the concentration of surfactant. By tuning the amount of oil released we can make microbowls of variable depth. In addition, we demonstrate that the microbowls can be further used to load different oils like silicone oil, hydrocarbons, and apolar dyes. The elasticity of the capsule wall and the left-over *PDMS* oil inside the capsule provide the principal driving forces by which one can promote the uptake of different oils, including dissolved dye molecules.

### 3.1 INTRODUCTION

In recent years polymer microcapsules have gained huge attention in fields as diverse as food science, pharmaceuticals, cosmetics, biotechnology, the paint industry and advanced materials [37, 41, 51–55]. To date different routes are available to fabricate a range of polymer capsules. Among them, the templating technique is a well known synthesis route. In this technique material is deposited on to a sacrificial template via methods such as interfacial polymerization [34, 106] and layer-by-layer self-assembly [37, 56]. Various templates, including solid particles (*e.g.*, silica, latex or gold colloidal particles) [57–60] and emulsion droplets [63, 64] have been used for this purpose. One main advantage of emulsion droplets as templates over solid particles is that the former can be removed under relatively mild conditions. In recent years there has been an increasing demand for microcapsules that can encapsulate and release cargo as desired, especially in the medical field for drug delivery. Polyelectrolyte microcapsules are a versatile system studied intensively in biotechnology and medicine for the controlled and targeted delivery of therapeutic molecules [107]. They are made by layer-by-layer adsorption of polyelectrolytes onto charged colloidal templates, followed by decomposition of the templates. One advantage of these microcapsules compared to other polymer capsules is the tunability of both capsule interior and wall using external triggers like a change in pH, temperature, ionic strength, *etc.* [108–110]. Moreover, the capsule wall can be functionalized with nanoparticles and biomolecules for targeted delivery [111]. In microcapsules available today chemicals are mostly encapsulated in the template during the synthesis. Alternatively, chemicals are allowed to diffuse through the permeable wall but the amount loaded will be limited by the bulk concentration and the encapsulation efficiency will be low. Accumulation inside preformed capsules has been observed to a certain extent in polyelectrolyte capsules [44, 87]. But it remains a challenge to design capsules that can reversibly load and release their cargo.

Microcapsules generally undergo a deformation when materials are released from their interior. This deformation results in interesting shapes depending on several factors like composition and thickness to radius ratio of the capsule, rate of deformation, wall permeability *etc.* [112, 113]. It is also important to have a good release mechanism for different types of microcapsules. In polyelectrolyte microcapsules the deformation of the capsule was achieved by osmotically induced buckling [114]. Also recently atomic force microscopy (*AFM*) in combination with fluorescence microscopy was used to quantify the release of materials from polyelectrolyte capsules [86, 114]. Moreover, an osmotic pressure difference has been used to investigate the folding pathways of polymer capsules of inhomogeneous thickness, upon release of inner material [115]. Another way to release the core and to induce buckling was reported in microcapsules made of

Pickering emulsion droplets [115]. There the deformation was induced by dissolving the inner core in an unsaturated continuous phase resulting in different morphologies.

In this chapter we focus on polymer capsule, recently developed in our group by Zoldesi *et.al.* [39,90] using an emulsion templating technique. They are the highly monodisperse, elastic *Tetraethoxysilane-crosslinked-PolyDiMethylSiloxane (TC – PDMS)* colloids. The sacrificial templates used for microcapsule preparation were emulsion droplets of polydimethylsiloxane (*PDMS*). By now several groups have used these droplets as templates for making different microcapsules because of their high monodispersity and relatively easy removal [80, 81, 83]. The *PDMS* droplets are obtained by the base catalyzed hydrolysis and condensation of the difunctional silane monomer dimethyldiethoxysilane (*DMDES*) into short linear oligomers approximately four units long [79]. The droplets are then coated with a solid elastic shell which is formed by crosslinking of a small percentage of the silicone oligomer with tetraethoxyorthosilicate (*TEOS*). If desired, the template can be easily removed by transferring the capsules to ethanol or even by evaporation. One main advantage of these microcapsules is the tunability of the shell thickness. It was found that, depending on the ratio of the shell thickness to the total particle radius (*i.e.* droplet radius and shell thickness,  $d/R_t$ ), solvent-filled *TC – PDMS* capsules formed different shapes upon drying: microspheres, microbowls, and microballoons [39]. Therefore they are also a good candidate for making anisotropic colloids. For many applications, the most important properties of a capsule are its wall permeability, adhesion, and mechanical behavior. Mechanical properties of the solvent filled *TC – PDMS* capsules were investigated using *AFM* and buckling experiments [116]. The deformation of the capsules strictly followed a macroscopic continuum theory derived to describe the elasticity of thin shells [117,118]. This was true both for the regime where the capsules were slightly flattened by the *AFM's* tip and the regime where a dimple is formed in the capsule wall. The Young's modulus ( $E$ ) of the shell was found to be 200 MPa, indicating that the material is somewhere between a soft polymer and a stiff rubber [116]. Qualitative experiments showed the permeability of solvent filled shells to polar molecules, but excluded apolar chemicals [90]. No studies were done on the controlled release and loading of chemicals in these microcapsules, as far as we know.

Herein, we report a novel method which enables these microcapsules to be emptied and then reloaded with an oil that could contain functional compounds, like surfactants, dyes or drugs. If needed, they can even be loaded and unloaded multiple times. This adds functionality for use in, for example, drug delivery. In the proposed method we utilize two aspects of *TC – PDMS* microcapsules that drive these processes; the elasticity of the shell and the apolar nature of the emulsion template. Release by buckling is first induced by micelles, which gradually dissolve the *PDMS* oil template inside the microcapsule by forming a microemulsion. This transforms the shape of

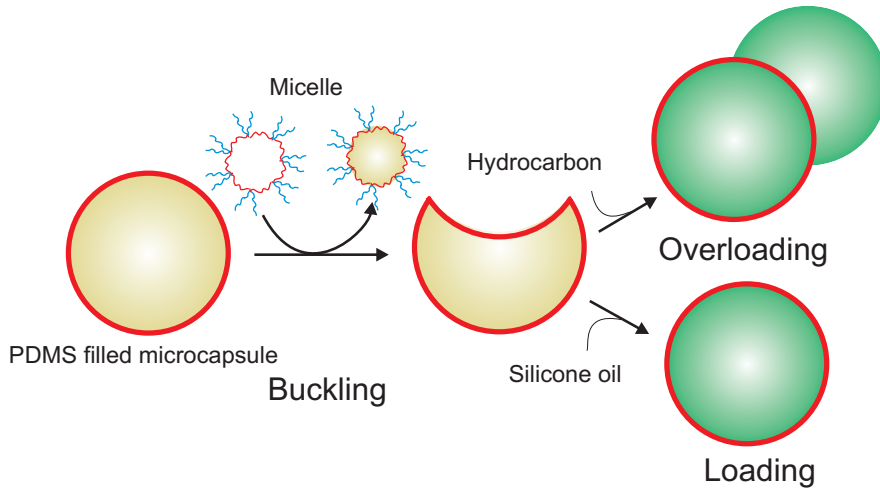


FIGURE 3.1. Schematic illustrating the release of core material through micelle induced buckling of a  $TC - PDMS$  microcapsule and subsequent loading and overloading in the presence of silicone oil and hydrocarbons.

the microcapsules to bowls. This shape provides an elastic restoring force to drive the reloading of the capsule when exposed to excess oil, like low molecular weight silicone oil or hydrocarbons that may also contain, for example, a hydrophobic dye. This process was helped by the mixing of the added hydrophobic chemical with some remaining  $PDMS$  template, which provided an additional driving force. The loading of hydrocarbons also led to interesting particle morphologies which depended on the kinetics at which the content was able to pass through the shells. Scheme 3.1 shows the whole process of release of  $PDMS$  oil and subsequent loading of different oils.

## 3.2 EXPERIMENTAL SECTION

### 3.2.1 Materials

Dimethyldiethoxysilane ( $DMDES$ , 97.0%) was obtained from Fluka Analytical. Tetraethylorthosilicate ( $TEOS$ , 98.0%), 3-aminopropyl-triethoxysilane ( $APS$ , 99%), rhodamine B-isothiocyanate ( $RITC$ ), pyrromethene 546, triblock copolymer Pluronic P123 ( $(PEG)_{20} - (PPG)_{70} - (PEG)_{20}$ , Mw-5800), ammonia (25 wt%  $NH_3$ ), octamethylcyclotetrasiloxane ( $OMCTS$ ,  $C_8H_{24}O_4Si_4$ ), cyclohexane ( $C_6H_{12}$ , 99.8%), decane ( $C_{10}H_{22}$ , 99.0%), hexadecane ( $C_{16}H_{34}$ , 99.0%) were purchased from Sigma-Aldrich.  $CdSeQD's$  were prepared using the recipe from reference [119]. All chemicals were used as received. Demineralized water (resistivity 18  $M\Omega cm$ ) was used in all reactions and also for cleaning of glassware.

### 3.2.2 Methods

#### *Preparation of PDMS contained TC – PDMS microcapsules*

*PDMS* filled microcapsules were prepared by the emulsion templating method reported by Zoldesi *et.al.* [116]. The synthesis was performed in two steps. In the first step monodisperse, *PDMS* an oil-in-water emulsion was prepared by base-catalyzed hydrolysis and partial condensation of the *DMDES* monomer  $((CH_3)_2Si(OC_2H_5)_2)$ . To make microcapsule suspension (11 mL) *DMDES* monomer (1 mL) and 25 wt% ammonia solution (2.5 mL) were added to deionized water (7.5 mL). The reaction mixture was then mixed by shaking either in a vortex mixer or by hand for 3-4 minutes. By this time the nucleation of *PDMS* droplets had started and the sample was placed on a rollerbank to gently stir the mixture during droplet growth. The concentrations of *DMDES* and ammonia used were higher than what was used in reference [116]. Droplets were grown for three to eight days. In the second step *PDMS* oil droplets were coated with a Tetraethoxysilane-crosslinked-PolyDiMethylSiloxane (*TC – PDMS*) shell by adding *TEOS* (0.018 M) in steps with 5 min intervals and then put on the rollerbank after each addition. The sample was diluted with deionized water (3 mL) prior to the addition of *TEOS*. To incorporate dye in the sample a solution of *RITC* (6.3 mL), prepared by mixing overnight *RITC* powder (6.5 mg) in ethanol (1 mL) and *APS* (coupling agent) (40  $\mu$ L), was added to the sample after the addition of *TEOS*. The shell is formed by the co-condensation of *TEOS* and unreacted *DMDES* left over from the *PDMS* droplet synthesis. From previous studies [39] it was clear that the main contribution to the thickness of the shell is from the unreacted *DMDES* in the sample. By tuning the days of droplet growth (3-8 days) and shell growth (1-5 days) we prepared microcapsules of different shell thickness/total particle radius ( $d/R_t$ ). We note that this procedure sometimes leads to more polydisperse capsules. We did our experiments only on those batches that turned out monodisperse.

#### *Controlled buckling of capsules*

*PDMS* oil from inside the microcapsule was released by adding a surfactant. A stock solution of Pluronic P123 (15 wt%) in water was prepared. The total radius ( $R_t$ ) of the particle and the thickness ( $d$ ) of the shell of two microcapsules used to study the variation of the depth of the dimples with surfactant concentrations were  $R_t = 2225$  nm and 2133 nm,  $d = 88$  nm and 16 nm, respectively. This corresponds to a ( $d/R_t$ ) of 0.04 and 0.0075. Different concentrations of P123 were added to a suspension of  $d/R_t = 0.04$  (0.52%v/v) microcapsules and a suspension of  $d/R_t = 0.0075$  (1.53%v/v) microcapsules. After addition the sample was shaken well and left to equilibrate for 30 mins. Then a capillary (Vitrocom,  $0.1 \times 1$  mm/ $0.1 \times 2$  mm) was filled with suspension to image the morphology of the microbowls. To study the evolution of the morphology upon surfactant addition of thin microcapsules with  $d/R_t = 0.006$  and  $d/R_t < 0.005$  a

capillary was partly filled with microcapsule suspension. Then slowly a P123 solution was injected into the remaining space of the capillary, such that a concentration gradient of P123 built up in the capillary. In this way we could see individual buckling events of microcapsules in the confocal or optical microscope.

#### *Reversed buckling of microbowls*

Microbowls obtained from buckling experiments were used to encapsulate different oils like silicone oil and hydrocarbons. The microbowls were therefore already placed in a Pluronic surfactant solution. The shell thickness to total particle radius ( $d/R_t$ ) of these microbowls was 0.04. For the encapsulation of *OMCTS* and cyclohexane bowls of depth to particle radius,  $\delta/2R_t = 0.78$  were used and for hexadecane  $\delta/2R_t = 0.56$ . The oil was dyed by dissolving pyrromethene 546 (oil soluble dye) (2 mg) in oil (1 mL) prior to addition, except for decane. The dyed oil (100  $\mu\text{L}$ ) was added to microbowl suspension (100  $\mu\text{L}$ ) and the sample was put on the rollerbank for mixing. Capillaries were filled with this suspension at different times, always avoiding the bulk oil phase. For the swelling experiment of microcapsules with cyclohexane spherical *PDMS* filled shells ( $d/R_t = 0.04$ ) dispersed in water were used. These did not contain any surfactant. For loading of *CdSe* quantum dots (*QD*) of size 3 nm microbowls of  $d/R_t = 0.56$  and  $d/R_t = 0.04$  were used. The *QD*'s were dispersed in toluene stabilized by oleic acid and made according to a literature procedure [119].

### 3.2.3 Characterization

The size and polydispersity of the *PDMS* oil droplets were determined by Static Light Scattering (*SLS*) experiments. The measurements were carried out using home-built equipment using a *He-Ne* laser as light source (632.8 nm, 10 mW). The thickness of the shell was measured using Atomic Force Microscopy (*AFM*, Digital Instrument, Nanoscope) in tapping mode. Samples for *AFM* were prepared by applying a drop of the shells in ethanol, after removing the *PDMS* core, onto a glass cover slide. The collapse of the shells leads to plateaus in the height that corresponds to twice the thickness of the shell. To study the post-buckling morphologies of the microcapsules and the relaxation of the microbowls in real space an inverted Leica, TCS-SP2 Confocal Scanning Laser Microscope in fluorescence mode was used. A 543 nm green *He-Ne* laser was used for the excitation of rhodamine-labeled shells and the 488 nm blue Argon laser was used for the excitation of pyrromethene 546 dye and *CdSeQD*'s. Samples were taken in a capillary either  $0.1 \times 1$  mm or  $0.1 \times 2$  mm for imaging.

## 3.3 RESULTS AND DISCUSSIONS

### 3.3.1 Controlled Buckling/Release

Monodisperse *TC - PDMS* microcapsules containing *PDMS* oil of sizes around 4  $\mu\text{m}$  were prepared using an emulsion templating technique as described in the methods

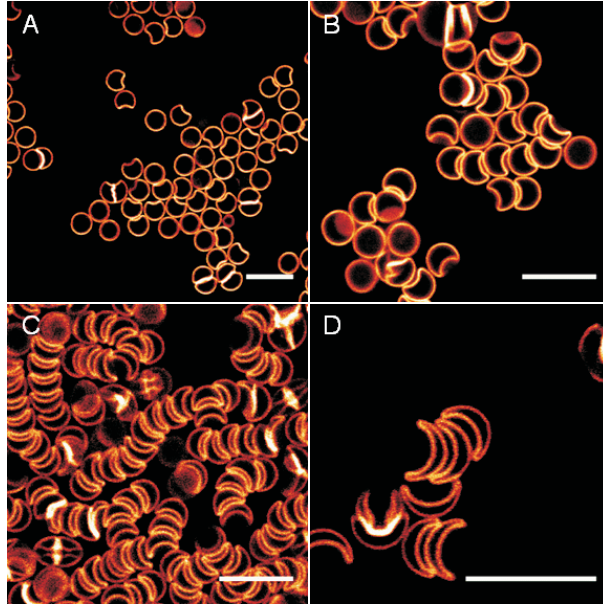


FIGURE 3.2. Confocal microscope images of microbowls ( $d/R_t = 0.04$ ) partly filled with *PDMS* obtained at different concentrations of Pluronic P123: (A) 0.48% v/v, (B) 1.44% v/v, (C) 5.3% v/v and (D) 6.3% v/v. All scale bars represent 10  $\mu\text{m}$

section. The *TC* – *PDMS* shell was labelled with the dye rhodamine B-isothiocyanate (*RITC*) to be able to observe the morphology of the capsules after release of the *PDMS* oil using confocal microscopy. To release the *PDMS* oil template from inside the microcapsules we used a surfactant. The surfactant used in the present study was the nonionic block co-polymer Pluronic P123 ( $(\text{PEG})_{20} - (\text{PPG})_{70} - (\text{PEG})_{20}$ ), but we expect that our methodology is not dependent on the exact nature of the surfactant used. The concentration of surfactant used was always above the critical micelle concentration (*CMC*) (0.004 wt% at 20 °C [120]). We started with microcapsules with a ratio of shell thickness to total particle radius ( $d/R_t$ ) of 0.04. To release the *PDMS* oil, we initially added 0.5 mL of an aqueous solution of P123 to 0.02 mL of microcapsules to give a final concentration of 0.48% v/v of P123 and 0.52% v/v of microcapsules. A precise number for the latter was obtained by counting the number of microcapsules in a volume measured with confocal microscopy. After addition the suspension was left for about 30 min to equilibrate and then observed with the confocal microscope. Figure 3.2A shows that the spherical microcapsules had developed a bowl-like shape with a small dimple. The presence of the dimple clearly indicates the release of *PDMS* oil contained in the microcapsule. Similar shapes were observed in water filled polyelectrolyte capsules that were buckled osmotically when exposed to a polyelectrolyte solution [114]. In the present system the release of *PDMS* oil from the capsules was triggered by the Pluronic micelles in the solution. The micelles in the suspension

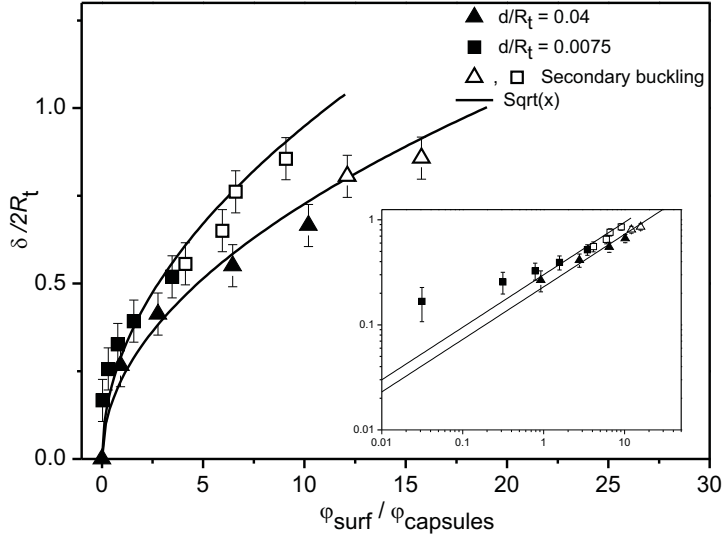


FIGURE 3.3. Plot of ratio of dimple depth to particle diameter ( $\delta/2R_t$ ) against the ratio of concentration of P123 surfactant to capsules ( $\varphi_{surf}/\varphi_{capsules}$ ) for two different  $d/R_t$ . Open symbols indicate samples in which secondary buckling into a polygonal shape was observed. Inst graph shows the double logarithmic plot with slope of the lines 0.5.

solubilize *PDMS* oil in the aqueous medium. This uptake of oil by micelles causes the capsule volume to decrease for as long as the tendency to solubilize oil exceeds the elastic restoring force of the shells, resulting in the buckling of the spherical capsule and the formation of a bowl-like shape. In figure 3.2A, some capsules appear to be spherical because the dimple is out of the focal plane, but it was observed by analyzing 3D confocal data sets that all capsules possessed a dimple of similar depth. Since we started with monodisperse spherical microcapsules the resultant microbowls were also monodisperse.

To release even more *PDMS* oil we further increased the concentration of P123 for the same concentration of microcapsules (0.52% v/v). The confocal pictures of microcapsules at concentrations 1.44% v/v, 5.3% v/v and 6.3% v/v of P123 is shown in figure 3.2B-D. The depth of the dimple increased, i.e. the microbowls became deeper, with increasing concentration of P123. This indeed shows that we can release the oil inside the capsule in a very controlled way by simply tuning the surfactant concentration, above the *CMC*. For surfactant concentrations below the *CMC* there was no release of *PDMS* and hence no change in the shape of capsules. In addition to the release of oil, the micelles also serve as a depletant [121]. The microbowls were found to self assemble into stacks by depletion force (figure 3.2B-D). This is similar to the lock and key self-assembly of colloidal particles described in reference [122].

From the mechanical theory of elasticity of shells [117, 118], the critical pressure at which a spherical capsule becomes unstable and buckles is given by the relation

$$P_c = \frac{4E}{\sqrt{12(1-\nu^2)}} \frac{d^2}{R_t} \quad (3.1)$$

Assuming the values of Young's modulus  $E = 200$  MPa [116] and Poisson ratio  $\nu = 0.3$ , for microcapsules of  $d/R_t = 0.04$  the critical buckling pressure that must be overcome to induce buckling is  $P_c = 0.3873$  Mpa (Equation 3.1). For the thinner capsules of  $d/R_t = 0.0075$  the calculated value of  $P_c = 0.0136$  MPa, is lower by about 96%.

Since the orientations of the microbowls in the stacks were mostly restricted we could easily quantify the average depth of the dimples from confocal images for different P123 concentrations. We compared the variation of the depth of dimple to particle diameter ( $\delta/2R_t$ ) with the ratio of surfactant to shell concentration ( $\varphi_{surf}/\varphi_{capsules}$ ) for capsules of  $d/R_t = 0.04$  and  $0.0075$  as shown in figure 3.3. As expected from the above relation,  $\delta/2R_t$  is higher for  $d/R_t = 0.0075$  compared to  $0.04$ , but only by about 50%. Also,  $\delta/2R_t$  is found to have approximately a square root dependence on  $\varphi_{surf}/\varphi_{capsules}$  for both  $d/R_t = 0.04$  and  $0.0075$  (inset of figure 3.3).

High resolution confocal images of microbowls of different capsule volume also gave us the possibility to investigate the precise shape of the dimple. For small to moderate depth the dimple was always an inverted sphere with the same radius of curvature as the original capsule. This way a strongly curved region was formed near the cusp. This curvature is related to the shell thickness and can thus be used to find an approximate, independent value of  $d/R_t$  of the capsules, which in other studies was determined by light scattering and atomic force or electron microscopy [37]. The estimation is done by using the relation between the radius of curvature at the cusp of the dimple  $r_{edge}$ , and the Föppl-von Kármán number,  $\gamma = 12(1-\nu^2)(R_t/d)^2$ , described in reference [123]:

$$\frac{r_{edge}}{R_t} = \frac{c}{\gamma^{1/4}} \left(1 - \frac{V}{V_0}\right)^{-1/4} \quad (3.2)$$

The numerical prefactor  $c$  is only weakly volume dependent. The radius of curvature  $r_{edge}$  for different capsule (reduced) volumes  $V/V_0$  ( $V$  - volume of dimple and  $V_0$ - initial sphere volume) was measured by fitting an osculating circle at the cusp of capsule as shown in figure 3.4A. The logarithm of this power law was indeed found to be a straight line with slope -0.25 and y-intercept  $\ln(c/\gamma^{1/4})$ . figure 3.4B shows the logarithmic plot of  $r_{edge}/R_t$  against  $(1 - V/V_0)$  for two capsules of  $d/R_t = 0.04$  and  $0.0075$ . Assuming  $c = 0.7$  from [123], we find the Föppl-von Kármán number,  $\gamma = (3.6 \pm 0.5) \times 10^3$  and  $(64 \pm 5) \times 10^3$  (Equation 3.2) for  $d/R_t = 0.04$  and  $0.0075$ . From this we find  $d/R_t = 0.055 \pm 0.004$  and  $0.0130 \pm 0.5 \times 10^{-3}$ , respectively, which is in reasonable agreement with the measured values.

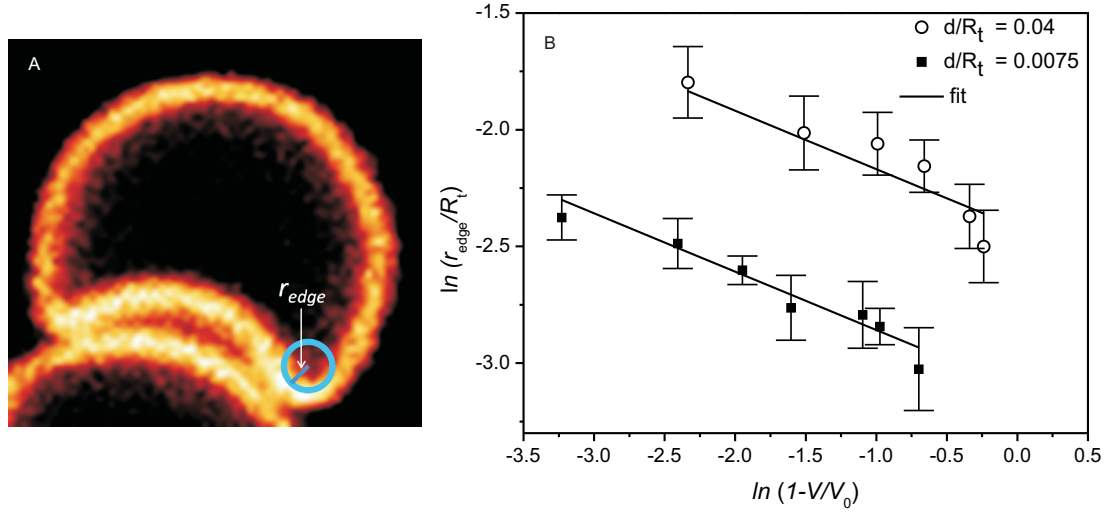


FIGURE 3.4. (A) Confocal picture of a microbowl ( $d/R_t = 0.04$ ) of reduced volume,  $V/V_0 = 0.93$ , with a radius of curvature at the edge of the circular rim,  $r_{edge}$ . (B) Logarithmic plot of ratio of radius of curvature to radius of capsules ( $r_{edge}/R_t$ ) versus capsule volume for microcapsules of  $d/R_t = 0.04$  and  $0.0075$ . The lines are fits with a slope of  $-0.25$ .

Simulations and experiments [112,113,124] have indicated that for a large deformation of thin elastic shells the smooth circular rim of the indentation undergoes a secondary buckling and forms a polygonal shape within the buckled dimple. This is a spontaneous way of minimizing the elastic energy of the shell caused by in plane stretching, which is energetically costly. This evolution of polygonal shapes, or stretching ridges, during the volume change of shells was seen to happen for large Föppl-von Kármán number,  $\gamma$ , which is inversely related to the ratio of shell thickness to total particle radius,  $d/R_t$ . Earlier buckling experiments performed on these shells, where the *PDMS* was completely dissolved in the solvent, have shown these polygonal shapes with four to eight regularly spaced wrinkles in the inner surface of microbowls [113]. These shapes were also reproduced in simulation [112,113]. We also observed these polygonal shapes when the volume of the capsule was sufficiently reduced. Cases where this happened are shown by the open symbols in figure 3.3. For capsules of  $d/R_t = 0.04$ , at a reduced volume,  $V/V_0 = 0.28$ , the rim of indentation is a smooth polygon with 4 wrinkles as shown in figure 3.5A. Whereas for  $d/R_t = 0.006$ , at a reduced volume of  $V/V_0 = 0.34$ , the rim of indentation was found to possess prominent sharp edged wrinkles, as shown in figure 3.5B. These well-defined polygonal internal structures would be

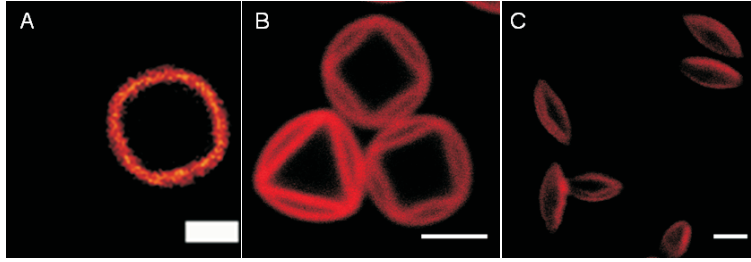


FIGURE 3.5. Confocal picture of (A) smooth polygonal rim of indentation for  $d/R_t = 0.04$  and  $V/V_0 = 0.28$ , (B) polygonal shape with three to four sharp wrinkles for  $d/R_t = 0.006$  and  $V/V_0 = 0.34$  and (C) subsequent collapse of microbowl with sharp wrinkles to a coffee bean shape with elongated depression. All scale bars represent  $2 \mu\text{m}$ .

quite interesting to combine with the recently developed depletion-induced lock-and-key interactions [122]. In the picture there is also a capsule with three wrinkles, which was not observed before in these microbowls. The maximum number of wrinkles observed was five; after that, instead of an increase in the number of wrinkles with decreasing inner volume, surprisingly the microbowls transformed into a shape with a single elongated depression, like that of a coffee bean (figure 3.5C). Coffee bean shapes were observed before in various experimental systems [83, 125, 126]. But then these shapes were not formed by a collapse of an initially bowl like conformation. They also have not been predicted theoretically for uniform shells [112, 113], but appeared when elongated apertures were introduced in the shells [127]. This might suggest that the coffee beans were induced by slight rupturing or weakening of the shells in their polygonal conformation.

We also looked at the evolution of the morphology of capsules of low value of  $d/R_t < 0.005$  (figure 3.6A-D). First, a number of indentations were observed (figure 3.6B) as predicted by simulations [112, 113]. But at a later time only a single large depression was left (figure 3.6C). Finally, the shell collapsed to a coffee bean shape (figure 3.6D). figure 3.6E is the corresponding confocal image of a coffee bean shaped particle. According to the theory of elasticity of shells [117], when a spherical capsule is subjected to uniform pressure, the deformation of the capsule or the depth of indentation has an inverse relation with the external pressure. This means dimples of large depth grow of their own accord, while smaller ones shrink. Recent simulations [112, 113] performed on spherical elastic shells showed that the evolution to a single indentation, the lowest energy state, from multiple indentations depends on the rate of deformation and the Föppl-von Kármán number. For slow enough deformation the shell evolves to a single indentation following an Ostwald ripening pathway rather than a merging of indentations.

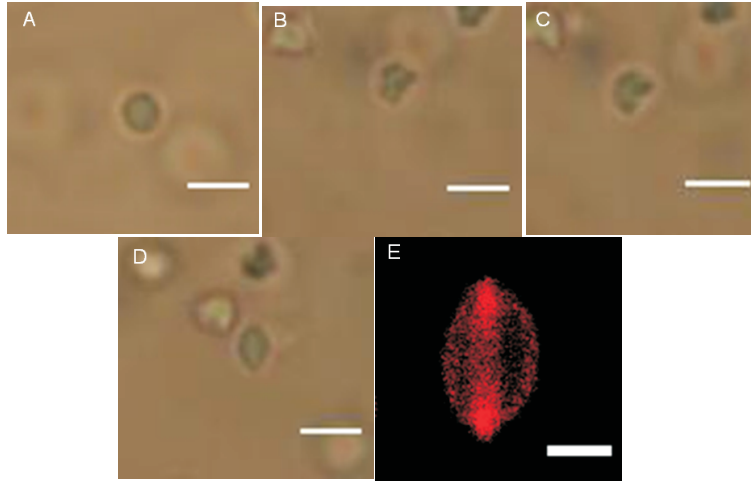


FIGURE 3.6. Optical microscope images of the morphology of extremely thin microcapsules,  $d/R_t < 0.005$  during the release of oil at (A)  $t = 0$  sec, (B) and  $t = 120$  sec, (C)  $t = 125$  sec and, (D)  $t = 163$  sec. (E) Confocal picture of a coffee bean particle. All scale bars represent  $2 \mu\text{m}$ .

### 3.3.2 Reversed Buckling/Loading

Here we introduce an efficient way to load hydrophobic chemicals including fluorescent dyes into preformed  $TC - PDMS$  microcapsules, by reversing the buckling process. Microbowls ( $d/R_t = 0.04$ ) obtained by controlled buckling were used for loading with an apolar liquid (oil). Loading of buckled shells with oil was done by making use of the elasticity of the shell. We did this by adding a small excess of the oil to a suspension of microbowls already present in surfactant solution from a buckling experiment. We started with the silicone oil octamethylcyclotetrasiloxane (*OMCTS*,  $C_8H_{24}O_4Si_4$ ). It was confirmed earlier that 90% of the *PDMS* oil inside the spherical microcapsule is *OMCTS* and the rest includes slightly longer linear oligomer chains and cyclic trimers [79, 90]. Thus most of the oil already present inside the capsules is *OMCTS*. The microbowls used for loading had a dimple to diameter ( $\delta/2R_t$ ) ratio of 0.78. *OMCTS* was dyed with an oil soluble dye, pyrromethene 546, for identifying its presence inside the capsule. Confocal snapshots at different stages of encapsulation of *OMCTS* by the microbowls is shown in figure 3.7A-D. Over a period of 6.5 h, the depression in the microbowls slowly decreased until they finally became spherical (figure 3.7D). Not only the *OMCTS* but also the dye was encapsulated in the microcapsule. Both oil and dye are poorly soluble in water making this process of diffusion of oil and dye through the aqueous phase slow. The presence of surfactant micelles probably helped speed up this process. Once the shell was fully relaxed no further change in shape was observed. Apparently, the elasticity of the shell prevented further uptake of oil. Similarly, we tested whether hydrocarbons of different carbon

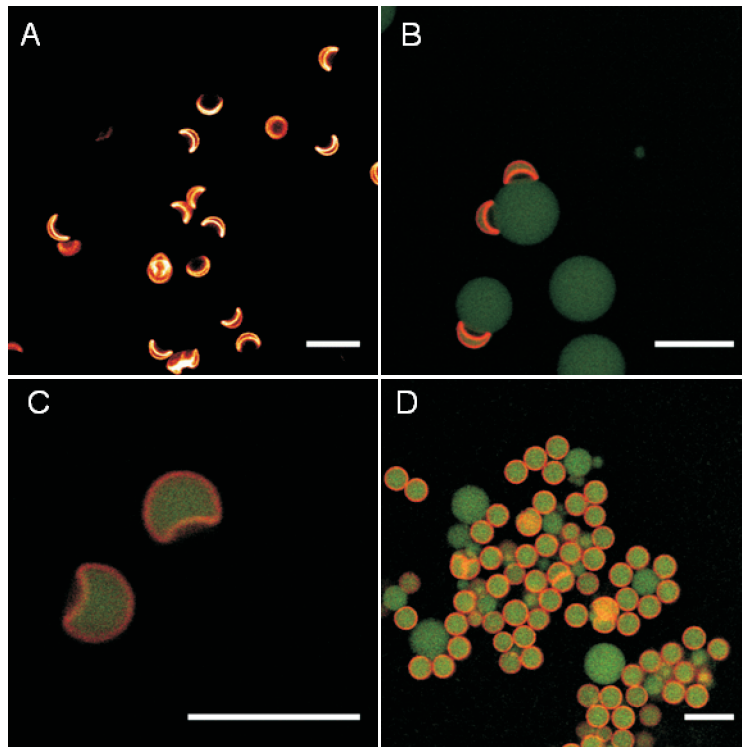


FIGURE 3.7. Confocal pictures of (A) microbowls ( $d/R_t = 0.04$  and  $\delta/2R_t = 0.78$ ) before loading and (B) 0.5 h, (C) 2.5 h, and (D) 6.5 h after addition of silicone oil, *OMCTS*. The shell is shown in red and the green color shows the dyed oil. All scale bars represent  $10 \mu\text{m}$ .

chain-length or molecular weight could also be encapsulated in the microcapsules. For hydrocarbons, the solubility of the oil in water plays an important role in the speed of encapsulation. In general, the solubility of hydrocarbons in water decreases with increasing chain-length.

We started with a lower cyclic hydrocarbon cyclohexane ( $C_6H_{12}$ ). The microbowls used for encapsulation and the method of preparation were similar to that of *OMCTS*. Confocal images of microbowls at different stages after addition of cyclohexane is shown in figure 3.8A-D. We observed that the bowls fully relaxed to spheres already within minutes, probably due to the relatively high solubility of cyclohexane in water. But in addition to elastic recovery, the microcapsules surprisingly continued absorbing oil forming dumbbell like particles. In figure 3.8A and C one part of the dumbbell is the spherical microcapsule (with a red shell) and the other part is the oil droplet (without a red shell). The images were taken from a capillary, prepared soon after mixing, by avoiding the presence of any excess cyclohexane phase. This prevented further growth of oil droplets from that shown in figure 3.8A. Over the next several hours, in the same capillary we observed the slow detachment of the oil droplet from the microcapsules, increasing the contact angle between the oil and the capsule from  $\theta$

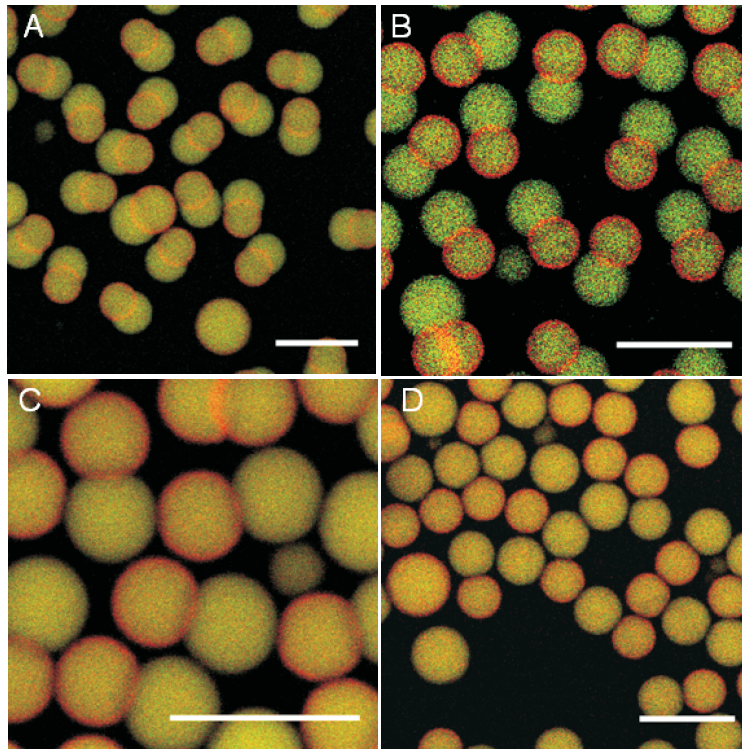


FIGURE 3.8. Confocal pictures of microbowls ( $d/R_t = 0.04$  and  $\delta/2R_t = 0.78$ ) after addition of cyclohexane (A) 25 min (B) 4 h, (C) 8 h, and (D) 10 h. The oil droplet sticking to the shells slowly detaches from the shell in time. The shell is shown in red and the green color shows the dyed oil. All scale bars represent  $10 \mu\text{m}$ .

$= 63.1^\circ \pm 2.8^\circ$  to  $180^\circ$ , figure 3.8A-D. The detachment possibly could have happened due to the slow adsorption of Pluronic surfactant, already present in the sample, to the oil-water interfaces causing a dewetting of the oil droplet from the shell. However, in the suspension with excess cyclohexane the droplets continued to grow larger while staying attached to the shells.

Apparently, in the cyclohexane case, apart from elasticity of the shell, there was an additional force that drove the uptake of cyclohexane by the bowls. Since  $\delta/2R_t = 0.78$ , the bowls still contained about 32% of the original *PDMS* at the start of the experiment. The difference in the composition of oil inside and outside the bowls creates an osmotic pressure difference. Due to the entropy of mixing, even after the shell had reached its original spherical shape, more and more cyclohexane molecules continued to diffuse into the shell. We hypothesize that this leads to the swelling of the capsule and consequent stretching of the *TC* – *PDMS* shell. However, since stretching is energetically costly elastic energy is minimized by pushing out the oil through the pores in the shell and nucleating a liquid droplet on the outside of the shell. In these

experiments with microbowls we were not able to observe the initial swelling of the capsules because the dumbbell structure was formed too soon after mixing, as micelles enhanced the transport of oil. We therefore repeated the swelling experiment with fully *PDMS* filled *TC - PDMS* shells ( $\delta/2R_t = 0$ ), in the absence of any surfactant. The capsules were therefore still spherical. Figure 3.9 shows the swelling and subsequent formation of oil droplets after addition of fluorescently labeled cyclohexane into a suspension of spherical microcapsules. The initial average size of the microcapsule was  $3.92 \mu\text{m}$ , measured from image figure 3.9A. Five minutes after addition of cyclohexane fluorescence was detected from inside the capsule, which indicated that the swelling process had started. We measured a maximal average increase in the size of the capsule by  $0.8 \mu\text{m}$  in diameter about 30 min after addition (figure 3.9B). It has been shown that the relation describing the stretching of a spherical shell due to a positive pressure  $P$  is [123]

$$R^2 - \frac{2Ed}{P(1-\nu)}(R - R_t) = 0 \quad (3.3)$$

Where  $R$  is the radius of swollen capsule. Using this, we find  $P(1-\nu)/E = 0.01$ . Assuming values of  $E = 200 \text{ MPa}$  [116] and  $\nu = 0.3$ , we calculate the pressure exerted on a capsule wall to be  $P=2.98 \text{ MPa}$ , a reasonable value for an osmotic pressure. The magnitude of this osmotic pressure is higher than the critical buckling pressure  $P_c = 0.38 \text{ MPa}$  for these capsules. This indicates the major role of the osmotic pressure in the overloading of capsules with cyclohexane. Later, about 1.5 h after addition, we could see an oil droplet partly enclosing the microcapsule figure 3.9C. The size of the capsule at this stage had returned to its initial value of  $3.92 \mu\text{m}$ . The fluorescence profiles (figure 3.9D) across the diameter of the capsule before and after addition of cyclohexane clearly show the changes in capsule size. The contact angle of  $22.6^\circ \pm 3.5^\circ$  between the oil and the capsule is much smaller than it was in figure 3.8A, for the same size oil droplet, probably due to the absence of surfactant this time. Interestingly, the part of the shell at the oil-water interface was also found to take on the curvature of the oil droplet, making the shell slightly nonspherical (figure 3.9C). This kind of deformation of a soft elastic surface by liquid drops onto which they are placed was reported in reference [128]. It was shown that this deformation of the elastic surface is due to the combined action of Laplace pressure inside the drop and the interfacial tension at its periphery. This also indicates the flexibility of our shells. The capsule wall was not ruptured during the swelling process. This we tested by adding Pluronic surfactant to the above suspension (shells with oil droplets). The shells buckled and formed microbowls, in the same way as with freshly prepared spherical shells.

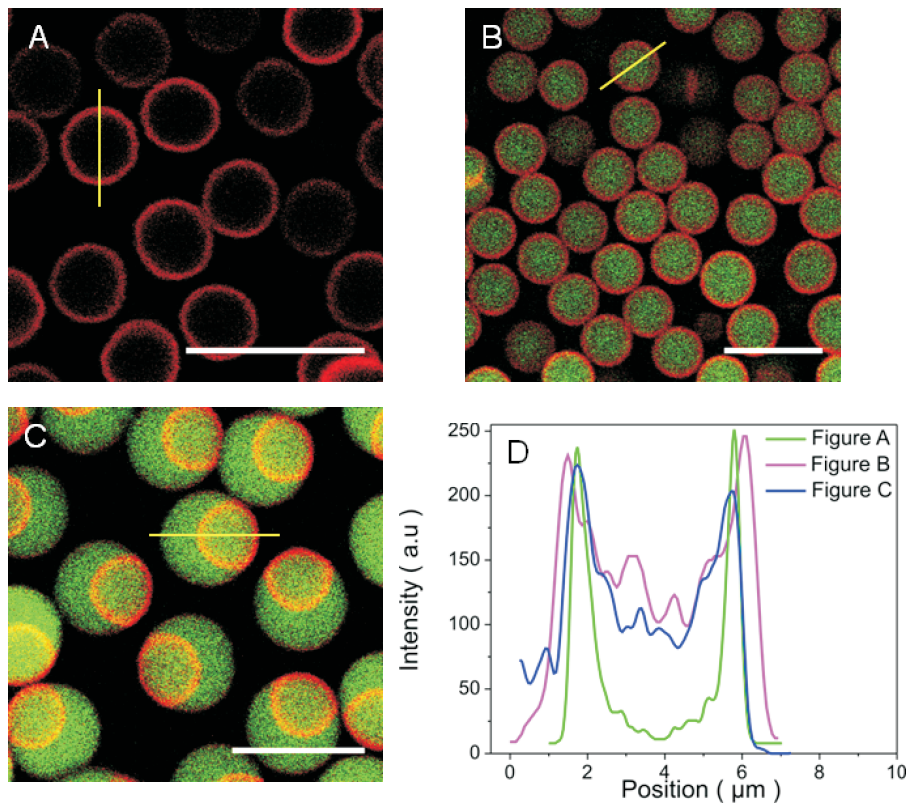


FIGURE 3.9. Confocal pictures of spherical  $TC - PDMS$  microcapsule ( $d/R_t = 0.04$ ) (A) before addition of cyclohexane and after addition of cyclohexane (B) 0.5 h, (C) 1.5 h. Shells are shown in red and cyclohexane in green. (D) A fluorescence profile across the diameter of typical capsules from all 3 confocal pictures. The intensity is the fluorescence from the capsule wall (red). The slightly larger values of intensity from the interior of the capsules in (B and C) compared to (A) is due to the cross-talk of fluorescence emission signal from the dye in the shell ( $RITC$ ) to that of the emission from the dye in the droplet (Pyromethene 546). To reduce pixel noise we applied a Gaussian filter (2 pixels) prior to plotting the fluorescence profile. All scale bars represent  $10 \mu\text{m}$ .

For a longer chain hydrocarbon, hexadecane ( $C_{16}H_{36}$ ), rather than overloading, the microbowls ( $\delta/2R_t = 0.56$ ) formed deeper dimples than the original as shown in figure 3.10A and B. Apparently, this time the  $PDMS$  was completely extracted from the capsules by the hexadecane rather than the reverse. This indicates that the rate of diffusion of  $PDMS$  in water exceeds that of hexadecane. Even after a period of two years these microbowls didn't fully relax to spheres, but there was a slight change in the shape of the bowls, due to a slight loading of hexadecane. Figure 3.10C is the confocal image of the microbowls in different orientations, loaded with a little hexadecane. This image was only taken two years after addition, and so we don't know how long this slight

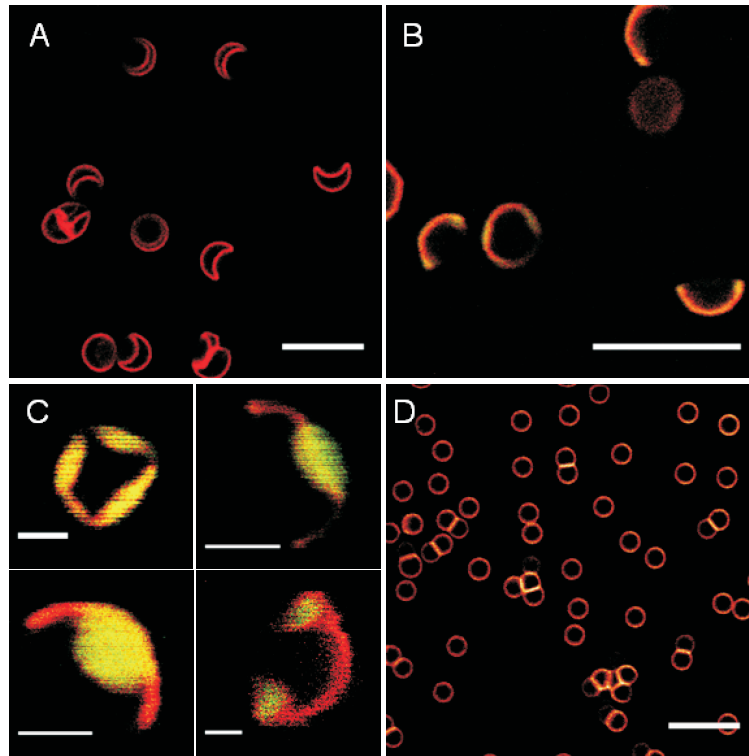


FIGURE 3.10. Confocal pictures of microbowls ( $d/R_t = 0.04$  and  $\delta/2R_t = 0.56$ ) : (A) before addition of hexadecane, (B) one day after addition, when the dimple has grown deeper, and (C) after a period of two years where the bowls are loaded with a small amount of hexadecane. (D) Spherical microcapsules ( $d/R_t = 0.05$ ) one year after addition of decane. Scale bars in (A), (B) and (D) represent  $10 \mu\text{m}$  and (C) represent  $2 \mu\text{m}$ .

shape transformation took, but probably much less than two years. That the microbowls didn't fully relax back is most likely because of the strong van der Waals forces at regions where the inner walls of the bowl touch. The presence of hexadecane was only detected from regions where the walls were not in contact. Thus the amount of hexadecane loaded in the capsules was low compared to *OMCTS* and cyclohexane. From the theory of Ostwald ripening we know that the ripening rate is proportional to the product of the solubility ( $C_\infty$ ) of the oil and its diffusion coefficient ( $D_0$ ), both of which decrease with increasing molecular weight. Of the other hydrocarbon oils we tested, hexane, 2, 2, 4-trimethylpentane, decane, dodecane and tetradecane, we qualitatively found that the product of solubility and diffusion coefficient of decane ( $C_{10}H_{22}$ ) was more or less the same as the *PDMS* oil inside the capsule (predominantly *OMCTS*). In the presence of dodecane and tetradecane microbowls formed deeper dimples, whereas with 2, 2, 4-trimethylpentane and hexane they formed dumbbells. Figure 9d shows a confocal image of spherical microcapsules ( $d/R_t = 0.05$ ) taken about one year after addition of

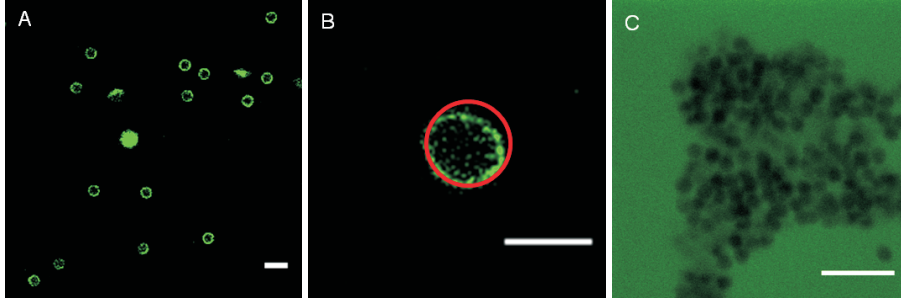


FIGURE 3.11. Confocal image of microcapsules ( $d/R_t = 0.04$ ): (A) 20 min after addition of a  $QD$ -toluene solution ( $CdSe$  with an average 3 nm size and coated with stabilizer oleic acid), (B) a fully relaxed microbowl ( $\delta/2R_t = 0.56$ ) with a toluene bulge marked by red circle that run through the perimeter of the shell at oil-water interface, taking the curvature of the oil droplet. (C) Slightly dried shells kept in direct contact with  $QD$  solution for three days. Scale bars in (A) and (C) represents 10  $\mu\text{m}$  and (B) represent 5  $\mu\text{m}$ .

decane to *PDMS* filled spherical capsules. Even after one year the capsules had not changed their shape. The shells remained spherical because the rate of diffusion was almost the same in both directions and the elasticity of the shell was also strong enough to withstand small volume changes. Meanwhile, for a much thinner shell,  $d/R_t = 0.006$  the elasticity of shell proved not strong enough to slight volume changes. This caused buckling, even with decane. The difference in the behavior of the shells in the presence of hydrocarbons lead to selective encapsulation of oils, which is most likely a general feature related to solubility and is of interest to explore further in future work.

Finally, we checked if nanoparticles, for example quantum dots ( $QD$ 's), can be loaded in the microcapsules along with apolar liquids. The  $QD$ 's that we used were  $CdSe$  particles of average size 3 nm dispersed in toluene and stabilized with oleic acid [119]. This suspension was added to microbowls of  $\delta/2R_t = 0.56$  and  $d/R_t = 0.04$  after the buckling experiments and examined under the confocal microscope about 20 min after addition (figure 3.11A). The microbowls fully relaxed to spheres within minutes but there was no fluorescence from the interior of the capsules. This indicated that the capsules can be loaded with toluene but that the shells are not permeable to the  $QD$ 's. In addition to elastic recovery, a toluene droplet formed outside the capsule similar to the case of loading with cyclohexane. This was a clear indication that the oil is loaded by the capsules, but the  $QD$ 's are not. Nevertheless, we also confirmed the impermeability of the shell to these  $QD$ 's by bringing them in direct contact with the microcapsules. For this experiment we added the  $QD$  solution to *PDMS* filled spherical microcapsules of  $d/R_t = 0.04$  lightly dried in an oven at 50  $^{\circ}\text{C}$  to remove the aqueous phase. The capsules got aggregated during drying, but the capsule wall was not permeable for 3

nm  $QD$ 's, indicated by the absence of fluorescence from inside the spheres. This also sets a threshold to the maximum size of materials than can be loaded in these capsules.

### 3.4 CONCLUSIONS

We demonstrated a new method to encapsulate and release hydrophobic liquids and dissolved molecules like a fluorescent dye in and from elastic *Tetraethoxysilane-crosslinked-PolyDiMethylSiloxane (TC – PDMS)* microcapsules. With the addition of surfactant micelles it is possible to solubilize the encapsulated oils, which leads to controlled buckling of the capsules. This buckling leads to the formation of anisotropic colloidal microbowls with a uniform and tunable dimple depth. For certain parameters the bowl shape underwent a further transition to well-defined shapes of interest for *e.g.* creating unique lock-and-key interactions. Additionally, there was a parameter range where a final transition to a coffee-bean shape was observed. The slow dissolution of oil, on the order of several minutes, allowed us to observe the morphology changes of the shells and hence the individual buckling events for different  $d/R_t$ . Elasticity of the shell and left over *PDMS* oil inside the capsule provided two driving forces for the uptake of hydrophobic oils and dye placed in contact with an aqueous suspension of microbowls, thereby efficiently encapsulating them in the capsules. We found that low molecular weight oils were readily encapsulated, whereas higher ones caused the capsules to empty even further and the amount loaded was rather low. Failure to load capsules with  $QD$ s of 3 nm size revealed the approximate upper limit for materials that can be loaded into the capsules in this manner. The proposed method of controlled buckling and subsequent loading from/into preformed *TC – PDMS* capsules can be further extended to drug molecules, provided they are hydrophobic and small enough to pass through the shell of the capsules.

### 3.5 ACKNOWLEDGMENTS

We would like to thank Mark Boneschanscher for his help in *AFM* measurement on capsules, Wiel Evers for providing the *CdSeQD*'s and Nina Elbers for careful reading of the chapter.



# 4

## 3D image processing on jammed packings of monodisperse elastic shells

A systematic image analysis routine to identify the 3D coordinates of monodisperse, fluorescently labelled elastic shells in jammed packings is described in this chapter. The shells in a jammed packing are deformed in such a way that at each contact one of the shells buckled with a dimple and the other remained spherical, closely resembling overlapping spheres. Using confocal microscope, we obtained 3D stacks of images of jammed shells which are subsequently processed in *ImageJ* software to find their coordinates. The determination of 3D coordinates involved three steps: locating the edge of shells in all 2D slices, analyzing their shape and subsequently finding their 2D coordinates, and finally determining their 3D centers by grouping the corresponding 2D coordinates. From this analysis routine the position of particles are obtained with sub-pixel accuracy. Additionally, from the 3D stack of confocal images we also identified the shells that underwent buckling and formed a dimple in a contact pair and hence the number of dimples per particles (buckling number,  $N_\delta$ ), which is a unique property of these packings.

## 4.1 INTRODUCTION

Jammed matter is an emerging class of complex systems consisting of disordered dense packings of particles as diverse as granular materials, colloidal suspensions, droplets, bubbles, pastes and gels. In jammed packings particles are in contact with each other so that they exert forces on their neighbors. The collection of contact forces creates a force network, which forms the skeleton of jammed matter. There are only a few systems for which these contact forces can be measured experimentally, either in 2D or even fewer in 3D.

Experiments to study the distribution of contact forces in granular materials started with measurements of forces exerted by the grains against a constraining surface using a carbon-paper technique [19, 33, 129, 130]. In this technique all constraining surfaces of the system were lined with a layer of carbon paper covering a white paper. Grains pressed the carbon onto the white paper and left marks at the contact regions whose size and intensity depends on the magnitude of the normal force on the corresponding grain. By using image analysis software and calibration curves, the contact forces at the surface were extracted. Another attempt to measure forces exerted on individual grains was using a high precision electronic balance, introduced by Lvoll *et al.*, [131].

In addition to boundary forces, inter particle force analysis in the bulk was also achieved recently, that enabled to investigate the spatial structure of the force network and the geometry of the packing. Majmudar *et al.* [32] measured the normal and tangential forces inside a 2D system of bidisperse photoelastic disks that were subjected to pure shear and isotropic compression. The stress induced birefringence of the disks also allowed in situ visualization of force chains in their system. The system under stress was imaged through crossed circular polarizers. From the images contact forces were obtained by fitting the observed photoelastic pattern inside each disk to the 2D elasticity solution [117] for the stress inside a disk. Although this system is promising, the deformation per disks was less than 1% of their average diameter in the compressed state [132], which prevented the system from reaching higher volume fractions, far beyond jamming point. Soft deformable particles are interesting in this aspect, as these particles can be packed to reach in principle a volume fraction of unity.

Compressed emulsions and foams are the most widely studied experimental soft frictionless systems nowadays [27, 28, 93, 133, 134]. Katgert *et al.* extracted various statistical and geometrical quantities in a 2D static packing of foam bubbles through image analysis. Brujic *et al.* [27, 93] introduced a method for measuring the contact force distribution within the bulk of a 3D compressed emulsion system using confocal microscopy. The oil droplets were index matched and fluorescently labeled and were compressed by an external pressure through centrifugation. Using image analysis routines like the Fourier Filtering Method the positions and radii of the polydisperse

emulsion droplets were extracted and the spheres were reconstructed. By analyzing either the size of the contact area or the enhanced fluorescence intensity at contact regions, the degree of deformation and hence the inter droplet normal force was calculated. Confocal microscopy was also used by Zhou *et.al.* [133] in 3D piles of frictionless liquid droplets labelled with a monolayer of fluorescent nanoparticles to obtain 3D images. Apparently, there are only a few soft jammed matter systems that have been studied and even fewer in 3D. Spherical particles with a solid elastic shell can be used to obtain local contact forces. Because of the flexibility or deformability of the shell these particles, along with other soft particles, foams and emulsion droplets, can be an interesting subclass of soft granular system for jammed matter research. The solid elastic shells are the particles (capsules) prepared by coating polydimethylsiloxane (*PDMS*) oil droplets by a Tetraethoxysilane-Crosslinked-PolyDiMethylSiloxane (*TC - PDMS*) shell and replacing the liquid interior with an index-matching mixture after removing the droplets by dissolution in ethanol, as described in chapter 2. By using confocal microscopy we will study quantitatively in 3D the microstructure and force networks in these jammed packings of elastic shells.

Confocal microscopy has already become a versatile tool in colloid science, in particular to obtain quantitative information on a single particle level [135–140]. The key feature of this technique is the use of a pinhole aperture that is confocal with the focal plane. The pinhole rejects most of the out-of-focus light arriving from the sample, producing a sharp image that represents a thin cross-section of the sample. 3D reconstruction of the sample is achieved by assembling a series of thin optical slices taken along the axial direction. Confocal microscopy coupled with image analysis techniques has provided a wealth of information on the structure of colloidal crystals, glasses and gels and their behavior under external fields [135–140]. Many of such quantitative studies are performed on spherical colloids that are homogeneously labelled with a fluorescent dye. It was for the first time demonstrated by our group [135–139] that the locations of these particles can be measured with sub-pixel accuracy. The 3D image stacks were processed by image processing algorithms developed by Crocker and Grier [141]. The algorithm works by searching for the local brightness maxima in the image within a characteristic length scale and determine the candidate particle locations, i.e. the nearest pixel to the true location as the starting value for a 2D fit making use of the spherical symmetry. Subsequently, the position is refined to sub-pixel accuracy by taking the first moment of the intensity distribution within a window around each candidate particle location. This algorithm was also extended to locate positions of anisotropic colloids like ellipsoids made by stretching spherical colloids [142], rod-like colloidal particles [143, 144] and colloidal clusters build up from spherically symmetric blocks [145–148], that are in almost all cases uniformly labelled.

Here we describe the image processing routines to investigate the structure and contact forces in jammed packings of fluorescently labelled elastic shells, especially their coordinates and deformation. Using laser scanning confocal microscopy in fluorescence mode we could image deep in the sample, above 50  $\mu\text{m}$  and acquire 3D stacks of images of index matched shells. The system was jammed such that all the particles remained static on our experimental time scale, except for a few percent at low densities close to random close packing. When the shells were jammed, at high packing fractions they underwent large deformation and formed dimples at contact areas. This resulted in asymmetrical shapes. This asymmetry both in intensity distribution and shape of these deformable shells precluded a straightforward use of available particle finding and tracking algorithms. Therefore, we developed new routines to analyze these particles in 3D. This was made possible by the fact that the deformed particle's shape can be well described by a spherical envelope containing one or more spherical dimples, like overlapping spheres. The analysis routine is based on processing the 3D stack of images, where each particle is distributed in a few slices, using *imageJ* algorithms [149–151]. The algorithms take into account the edge and shape of the individual shells in 2D slices to reconstruct the particle in 3D.

## 4.2 CONFOCAL MICROSCOPY

### 4.2.1 Sample preparation

The shells used for jamming studies were prepared in three steps: first a polydimethylsiloxane (*PDMS*) oil-in-water emulsion (total volume 750 mL) was made by mixing 6.8% v/v of dimethyldiethoxysilane (*DMDES*) monomer and 22.7% v/v ammonia using a Turrax homogenizer as described in chapter 2 (Experimental section). In the second step a tetraethoxysilane - crosslinked - polydimethylsiloxane shell was coated around the droplets by adding 8 mL tetraethoxysilane (*TEOS*) and 8 mL *DMDES* simultaneously after diluting the emulsion (550 mL) with aqueous solution (total volume 1725 mL) of 2.3 wt% *PVP*. The shell was fluorescently labelled by adding 0.330 mL of rhodamine B-isothiocyanate (*RITC*) dye solution coupled with 3-aminopropyltriethoxysilane (*APS*) (refer chapter 2 for dye preparation) to the reaction mixture during shell growth. Finally, after 2 days of coating the oil filled shells were transferred to anhydrous ethanol to dissolve the *PDMS* core. The particle radius was  $R_t = 2.74 \pm 0.03 \mu\text{m}$  with polydispersity 3% and shell thickness  $56 \pm 2 \text{ nm}$ . The radius of the droplet template was measured by static light scattering (*SLS*) and the shell thickness was obtained from atomic force microscopy (*AFM*) as described in chapter 2.

For confocal measurements a concentrated suspension of ethanol filled shells were dispersed in an index matched solvent of 52.6% v/v dimethyl sulfoxide (*DMSO*) and 47.4% v/v ethanol. This mixture had a refractive index of  $n_D^{20} = 1.42$ . We prepared

jammed states of these shells by centrifugation. A few drops of the suspension of shells were put in a capillary of dimensions  $0.1 \times 1 \times 50$  mm (depth  $\times$  width  $\times$  length, VitroCom). One side of the capillary was filled with candle wax after filling it with the shells. We used the wax to support the shells after they had been centrifuged in the solvent. Both ends of the capillary were then closed with *UV* glue (Norland, no.68). The sample was centrifuged twice to produce a dense packing, at 2000g for 25 mins and 1000g for 15 mins with the capillary length along the direction of gravity.

#### 4.2.2 Image acquisition

3D image stacks of the dense packing of hollow shells were acquired with a Nikon C1 confocal microscope with a  $63\times$  NA 1.4 oil immersion objective (Nikon) in fluorescence mode. The capillary was mounted on a microscope stage tilted 90 degrees with respect to gravity. This way the capillary could remain in an upright position so as not to disturb the packing. The *RITC* dye in the shell was excited with a 543 nm *HeNe* laser. The sample was scanned with a pixel dwell time  $3.12 \mu\text{s}$  and frame rate 0.196 fps. While scanning in the  $Z$  direction the laser power was increased typically from 4-7% to 10-12% of total power. We did this to compensate for the intensity drop deep in the sample caused by the index mismatch between the sample ( $n_D^{20} = 1.42$ ) and the immersion medium ( $n_D^{20} = 1.5$ ) [152]. An image stack comprised of  $1024 \times 1024 \times 790$  voxels with a voxel size of  $0.0976 \times 0.0976 \times 0.1094 \mu\text{m}^3$ , giving a total 3D image stack of  $99.94 \times 99.94 \times 86.43 \mu\text{m}^3$ . Acquisition of this image stack approximately took 67 mins. The voxel size in  $Z$  was corrected for index mismatch with a scaling factor 0.91 [152, 153]. During scanning there was no drift in the suspension and the particles were tightly packed such that they did not undergo Brownian motion.

### 4.3 IMAGE PROCESSING

Figure 4.1 shows confocal images (16 bit) of  $XY$ ,  $YZ$  and  $XZ$  slices out of a full 3D data stack. The image quality is good enough, even in  $Z$ , to perform a quantitative structure and contact force analysis. It can be seen that every particle deforms in a rather regular way: the overall shape remains spherical, but at points of contact with a neighbor the particle either received or produced a spherical indentation from/in its neighbors. It is this regular shape-deformation that allows us to determine well-defined particle centers and hence the contact forces between them. The image processing routine we have developed to find the positions of the hollow shells in 3D consists of three steps: locating the edge of the individual particle distributed in several slices, analyzing their shape in each slice to obtain their 2D centers and radii, and finally grouping their radii and centers to reconstruct the particles in 3D. The image processing was implemented using the free image processing software package *ImageJ* [149].

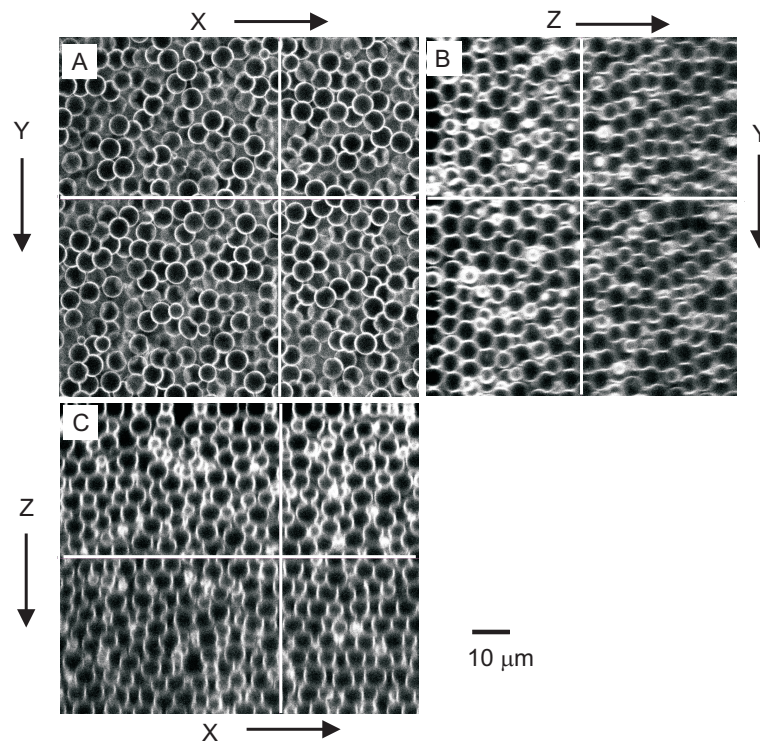


FIGURE 4.1. (A) Confocal microscopy images of dense packing of fluorescent shells  $XY$ , (B)  $YZ$  and (C)  $XZ$  slice. Image size in  $XY$  is  $1024 \times 1024$  pixels and 790 slices in  $Z$ .

The first three steps in image analysis are described in sections 3.3.1 to 3.3.3. Finally, in section 3.3.4 we describe a method to identify the dimpled or deformed particle in each contact pair.

#### 4.3.1 Edge detection

In dense packings of elastic shells, the shells are in close contact with their neighbors and even undergo deformations at contact points. Figure 4.2A shows a part of a 2D confocal image from a 3D stack of compressed shells. In the image the brightest pixels correspond to the fluorescence intensity from the shell part of the particles. These pixels form contours that delineate the shapes of the deformed particles. The black region enclosed within each white contour and in the space between particles corresponds to the index matching solvent mixture (*DMSO* + ethanol). The width of the white contour cannot be directly compared to the thickness of the shell, or even of two shells in direct contact, because the actual shell thickness (56 nm) is well below the lateral resolution of the microscope ( $\sim 200$  nm). But a difference in the contour width and in brightness is visible in regions where the particles are in contact compared to the non-contact regions. At the contact regions the contour is wider and brighter due to the double contribution to the fluorescence intensity from both the particles in a pair. In the images the contrast between the shell region and the interior is not the same for

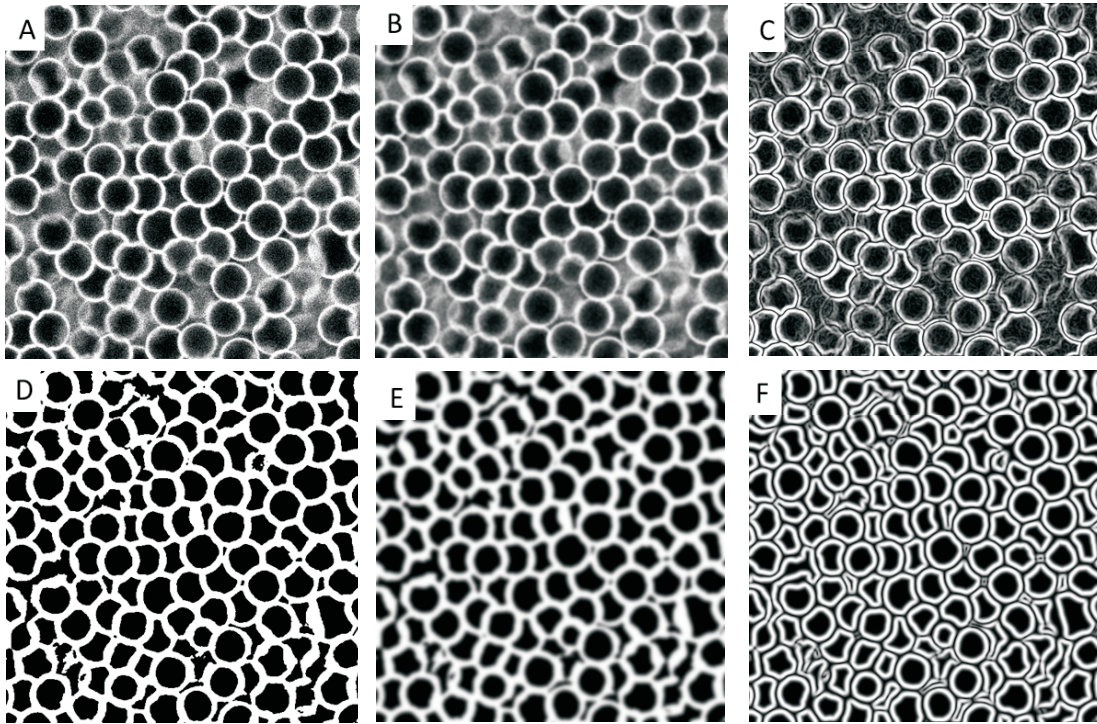


FIGURE 4.2. Different stages of edge detection: (A) 2D confocal image of hollow fluorescent shells, (B) smoothed image,  $\sigma = 1.5$  pixels, (C) edges detected with the Sobel algorithm directly on image B, (D) binary image after local thresholding of image B, (E) greyscale image obtained by convolution of the binary image with a gaussian,  $\sigma = 1.5$  pixels, and (F) edges detected with Sobel algorithm in image E. Image size is  $544 \times 544$  pixels.

each particle. This is caused by a convolution of the thin shell and the 3D point spread function [153]. The lateral contrast of a spherical fluorescent shell is highest when the focal plane intersects it near the equator and decreases moving towards the poles.

To identify the position of individual particles in these dense packings we first needed to distinguish or separate each particle from its neighbors. We did this by finding the edge of the particle. The edge of an object in an image is the set of locations where the intensity or brightness changes sharply. In the confocal image sharp intensity variations occur near the shell (white contour), which corresponds to the boundary of the particle. We used the Sobel edge detection algorithm to detect these edges [154]. The algorithm works on a gradient or first derivative method. The gradient method detects edges by looking for the maximum and minimum in the first derivative of the image. Before applying the Sobel algorithm we performed a few operations on the original 2D image shown in Figure 4.2A.

First the image was smoothed with a Gaussian blur filter of standard deviation  $\sigma = 1.5$  pixels to suppress noise in the image shown in Figure 4.2B. However, smoothening does not resolve the non-uniform brightness of white contours and poor contrast in some particles. We found that applying the Sobel algorithm directly on a smoothed image resulted in broken edges for some particles, as seen in Figure 4.2C. To overcome this problem we first applied a threshold to the greyvalue of pixels in the smoothed image. The value of the threshold for each pixel was decided locally by a local thresholding algorithm [155]. Among the local thresholding algorithms we found the mean algorithm to work best in these images. With this algorithm, each pixel is set at a threshold value which is equal to the mean of the greyvalue of its neighbors within a window of size 25 pixels, approximately the radius of the particle. This resulted in a binary image shown in Figure 4.2D. In the third step the binary image was converted back to greyscale image by convolving it with a gaussian function of  $\sigma = 3$  pixels, Figure 4.2E. The greyscale image after thresholding and convolution clearly has a much higher contrast and more uniform brightness in the shell regions compared to the one before, Figure 4.2B. We did this step to make the profile of the intensity near the shell smoother. This conversion makes the location of the edge and the shape of the detected particle closer to the actual particle. In the final step we applied the Sobel algorithm. Figure 4.2F shows the gradient image of particles separated from their neighbors by edges represented by white pixels. The image Figure 4.2F also contains features enclosed by edges that do not resemble particles in regions where they are barely visible. These features were removed in later stages of the image processing.

### 4.3.2 Shape determination and fitting

The second step in finding the positions of the particles includes analyzing the shape of the individual shells bounded by their edges in figure 4.2F. In ImageJ there is an algorithm called *Analyze Particles* [149] which counts and measures objects in binary or thresholded images. It works by scanning the image until it finds the edge of an object. By applying this algorithm on the thresholded image, figure 4.3A from edge detection we obtained figure 4.3B. Note that during this step the objects close to the edge of the image volume without a closed contour were not detected. To remove false objects that do not resemble the particles in figure 4.3A we limited the circularity of the objects to 0.2-1.0. Objects outside this limit mainly consisted of out-of-focus particles that appear fused together in the original image. This creates voids or black regions in the image. This does not mean that there are particles missing from our analysis. These particles will be identified in subsequent slices in the stack. Any remaining false objects were removed in a later step of the analysis. Figure 4.3C shows the zoomed in ( $210 \times 210$  pixels) view of objects highlighted and marked with numbers.

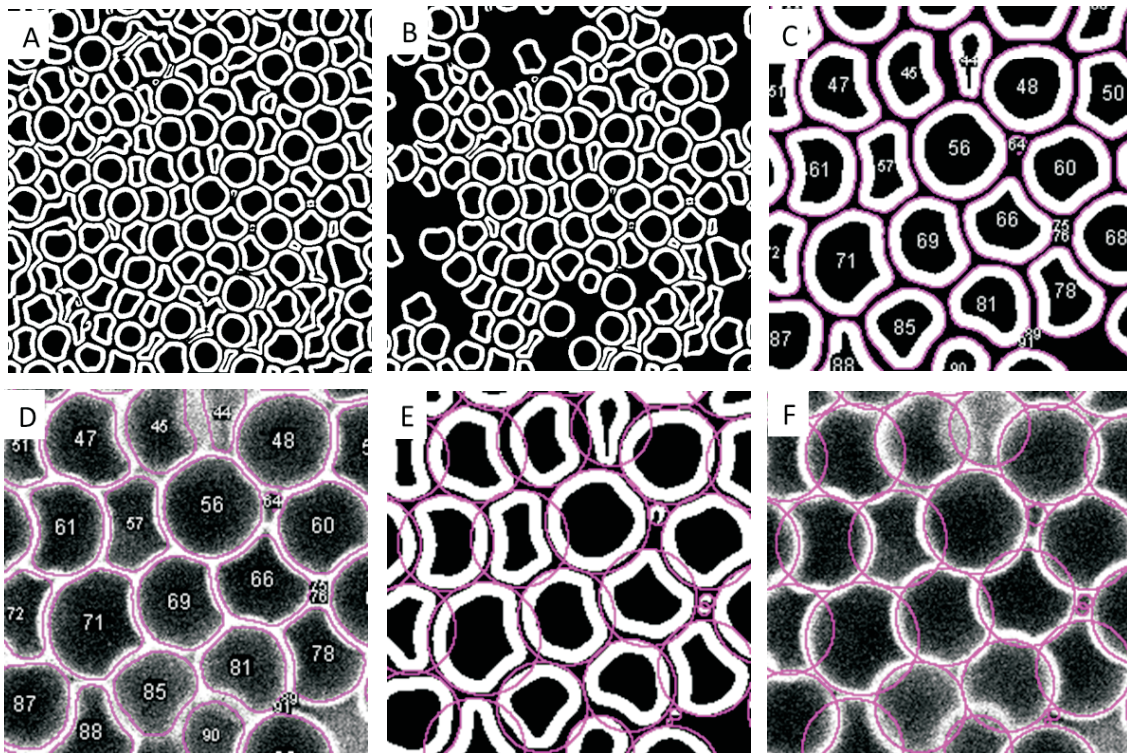


FIGURE 4.3. Different stages of shape determination: (A) Binary image of particles obtained from the edge detection step, (B) particles detected using the analyze algorithm, (C) zoomed in view of image B with particles labelled and highlighted, (D) overlay of the original confocal image and the detected particles, (E) the detected particles enclosed by the *SEC*'s and (F) overlay of the original particles and the *SEC*'s that enclose them. Image size of A and B are  $544 \times 544$  pixels whereas C, D, E and F are  $210 \times 210$  pixels. The pixel size is  $0.0976 \mu\text{m}$  in all images.

To check how well the edge and the shape of the detected particles match with the original particles, we overlaid the processed image with the original image as shown in figure 4.3D. The shapes of the detected particles closely resemble the actual shapes of the particles. However, the detected particles are not touching each other anymore, though the shells were in contact in the original image. The image processing has introduced a gap of a few pixels wide between neighboring particles. For shape analysis we ignored these pixels, but we took them into account in the final stage of finding the positions and radii of the particles.

Furthermore, since the shells were spherical initially before compression, the geometric 2D center of the detected particles in each slice does not correspond to the center of the original shells in that slice. Instead, we determined the 2D center of the original particle in each slice by fitting the smallest circle that still encloses the detected particle shape as shown in figure 4.3E. We used the algorithm called *Smallest*

*Enclosing Circle (SEC)* [149] in ImageJ for fitting the circle. The algorithm takes all the  $XY$  coordinates in the perimeter of the detected particle and calculates iteratively the geometric center and radius of the circle that includes the farthest coordinate from the center. Figure 4.3F shows the overlay image of the original shells and the corresponding  $SEC$ 's. The perimeter of the circles run almost exactly through the convex contours of the original particles. The overlap areas of the circles correspond to the area of the dimples.

### 4.3.3 Centroid and radius determination

From the shape detection step we obtained the radii and centers of  $SEC$ 's that enclose the detected particles in all 2D slices in a 3D stack. Figure 4.4A shows the probability distribution of radii of  $SEC$ 's,  $R_{SEC}$ , from the stack of image volume  $99.94 \times 99.94 \times 86.43 \mu\text{m}^3$ , after filtering out the rest of the false objects, based on size, that were not removed in the shape detection stage. Here we also compensate for the gap between the detected particles in each slice by increasing the radii of the  $SEC$ 's by half the width of the gap, which was 2 pixels in the image. The peak in the distribution occurs at around 29 pixels, close to the measured radius of the original particles, which was 28 pixels. The tail of the distribution indicates the radii of cross-sections near the equator of the particles and also the presence of a few large particles in the packing.

In the final stage of locating particle position we grouped the  $SEC$ 's that belong to the same particle and reconstructed the actual particle. We grouped the  $SEC$ 's by searching for similar  $XY$  centers within a defined interval in  $Z$ . The interval in  $Z$  was set at a value less than the diameter of the particle, as the particles were not nicely detected near the poles. For these particles of diameter 50 pixels in  $Z$  we set the interval at 35 pixels. To reconstruct the original particle from the collection of  $SEC$ 's obtained for each particle, we considered the plot of the radii of the  $SEC$ 's against their corresponding  $Z$  position in the stack. An example is shown in Figure 4.4B. These data points were then fitted with the equation of a circle,  $R_{SEC}^2 = R_t^2 - (Z - Z_c)^2$  (Figure 4.4B). The fit gives the center  $Z_c$  and the total radius of the particle,  $R_t$ . The  $X$  and  $Y$  coordinates of the center of the particle were obtained by taking the average of  $X$  and  $Y$ 's of the set of  $SEC$ 's that make up each particle. The average of the standard deviations in the  $X_c$  and  $Y_c$  was 80 nm and  $Z_c$  was 40 nm (estimated from the fit), which are below the pixel size. The relatively high value of error in  $X_c$  and  $Y_c$  compared to  $Z_c$  most likely originated from the slight inaccuracies involved in the shape determination and fitting of  $SEC$ 's. For some particles we found that the  $Z_c$  deviated from the actual center. This was caused by the overlap of  $SEC$ 's from particles lying exactly on top of one another and also from the contribution of  $SEC$ 's of any remaining false objects. A typical graph of such a particle with incorrect  $Z_c$  is shown in the inset

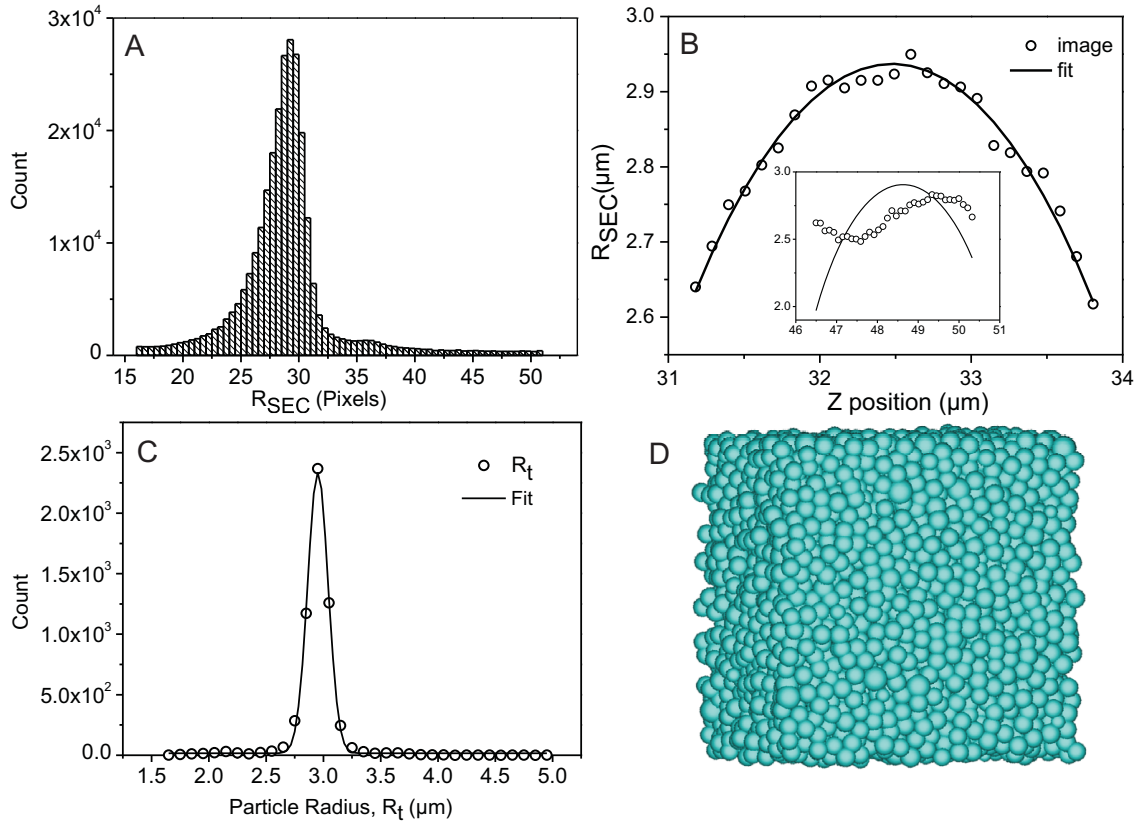


FIGURE 4.4. (A) Distribution of radii of the  $SEC$ 's,  $R_{SEC}$  enclosing the detected particles in each slice in a 3D stack of images. (B) Plot of  $R_{SEC}$  vs corresponding  $Z$  position of a particle. The line is the best fit of a circle through the data points with fit parameters:  $Z_c = 32.48 \pm 0.01 \mu\text{m}$  and radius of the particle  $R_t = 2.937 \pm 0.002 \mu\text{m}$ . Inset plot corresponds to an incorrectly fitted particle (C) Distribution of the particles radii  $R_t$ . We measured an average radius  $2.95 \mu\text{m}$  with a standard deviation  $0.17 \mu\text{m}$  obtained from a Gaussian fit (line) (D) 3D reconstruction of particles in an image volume  $99.94 \times 99.94 \times 66 \mu\text{m}^3$  at a volume fraction 0.908.

of Figure 4.4B. We sorted out these particles by setting a threshold for the standard error in  $Z_c$  obtained from the fit.

We identified 5753 particles in a volume of  $99.94 \times 99.94 \times 66 \mu\text{m}^3$ . This number (5753) does not include the particles close to the edge in the  $X$  and  $Y$  direction as they were not identified during image analysis. Note that a particle near the edge is only identified if its full volume reside inside the image volume. We also excluded about four layers of particles in the  $Z$  direction due to slight ordering near the wall. Figure 4.4C shows the distribution of radii  $R_t$  of the identified shells. This distribution is nicely symmetric with average radii of particle  $R_t = 2.95 \mu\text{m}$  with a standard deviation  $0.178$ , this corresponds to 6% polydispersity. The radius of the particles obtained from image analysis is close to the value that was obtained from  $SLS$ , which is more accurate, but

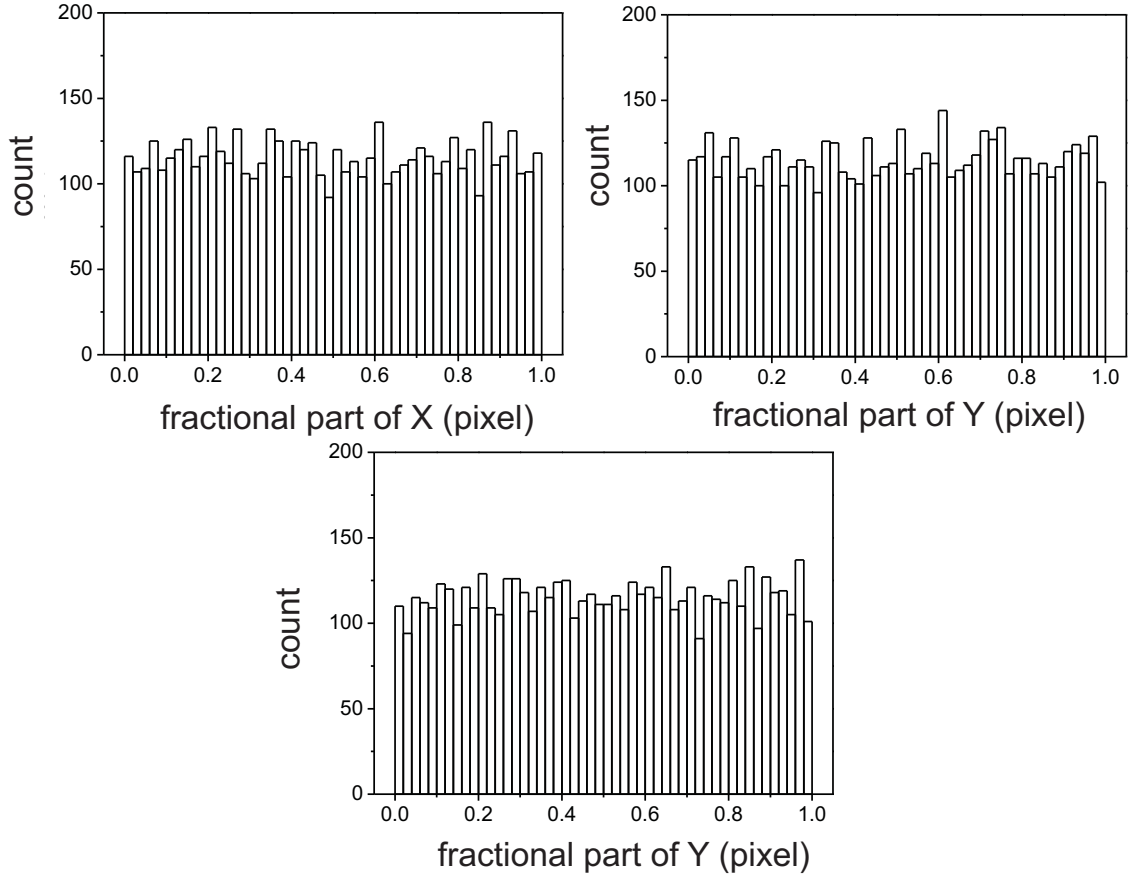


FIGURE 4.5. Distribution of the fractional part of the particle coordinates  $X_c$ ,  $Y_c$  and  $Z_c$  found using the image analysis routine in an image volume  $99.94 \times 99.94 \times 66 \mu\text{m}^3$ .

polydispersity is slightly higher resulting from the inaccuracies in image analysis. In these 5753 particles there were 1.4% particles with an incorrect  $Z_c$ , which is a relatively small fraction. These particles along with the small fraction of small particles (1.8%) and large particles contribute to the flat tail of the distribution of  $R_t$ . Figure 4.4D shows the 3D reconstruction of the packing containing 5753 particles.

To test the accuracy of the algorithms in locating the position of particles we checked for pixel biasing [139]. Figure 4.5 shows the density distribution of the fractional part of  $X_c$ ,  $Y_c$  and  $Z_c$  of the particles measured in pixels. The top part of the histogram is almost flat in all the three graphs. This is again a clear sign that particles are located with sub-pixel resolution. However, we did see a strong bias in the fractional part of pixel for the 2D centers,  $X_{SEC}$  and  $Y_{SEC}$  at 0 and 0.5 (not shown). This also may be the reason for the higher value of the error in  $X_c$  and  $Y_c$  compared to  $Z_c$ .

The volume fraction of this packing was 0.908. This value was obtained by summing the volumes of 5753 spheres and subtracting their overlap volume in an image volume

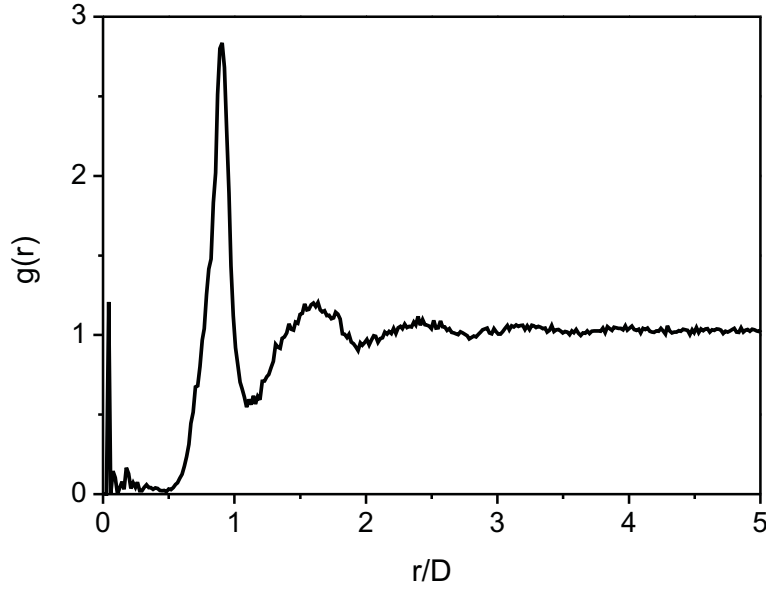


FIGURE 4.6. Radial distribution function  $g(r)$  for the same volume fraction.

of  $(99.94 - 2R_t) \times (99.94 - 2R_t) \times 66 \mu\text{m}^3$ . The image size was reduced by  $R_t$  from all sides in the  $X$  and  $Y$  directions to compensate for the particles that are missing near the edge. The value of volume fraction obtained from the image analysis is highly sensitive to the radius of the particles obtained. Therefore, the absolute volume fraction may contain an error of about 0.04. Figure 4.6 shows the radial distribution function of this packing. The shape of the distribution is similar to that of a liquid but the first peak of the distribution appears at a radial distance ( $r$ ) less than the diameter of the particle ( $D$ ). This was caused by the large deformation of the shells. The 1.4% incorrectly fitted particles are responsible for the sharp peak at  $r/D \approx 0$ .

#### 4.3.4 Dimple detection

In a dense packing of hollow shells, the shells undergo deformation upon contact. The deformation is such that one of the shells buckles with a dimple and the other one remains spherical at the contact area as shown in the cartoon in figure 4.7A. We proceeded to identify the particle in contact pairs that has the dimple. The dimpled particle was detected by drawing a line that connects the 3D centers of neighboring particles and then locating the position of the maximum in the fluorescence intensity along the line. The position of the maximum will be closer to the center of the particle that is dimpled. The lines that connect 3D centers of pairs of particles in a stack were drawn by the *3D Bresenham algorithm* [156]. This algorithm is widely used to draw pixelated lines connecting two end points in a digital image. The algorithm takes the 3D coordinates of the centers in a pair of particles as the end points and generates intermediate coordinates iteratively. Out of the three coordinates  $X$ ,  $Y$  and  $Z$  of the

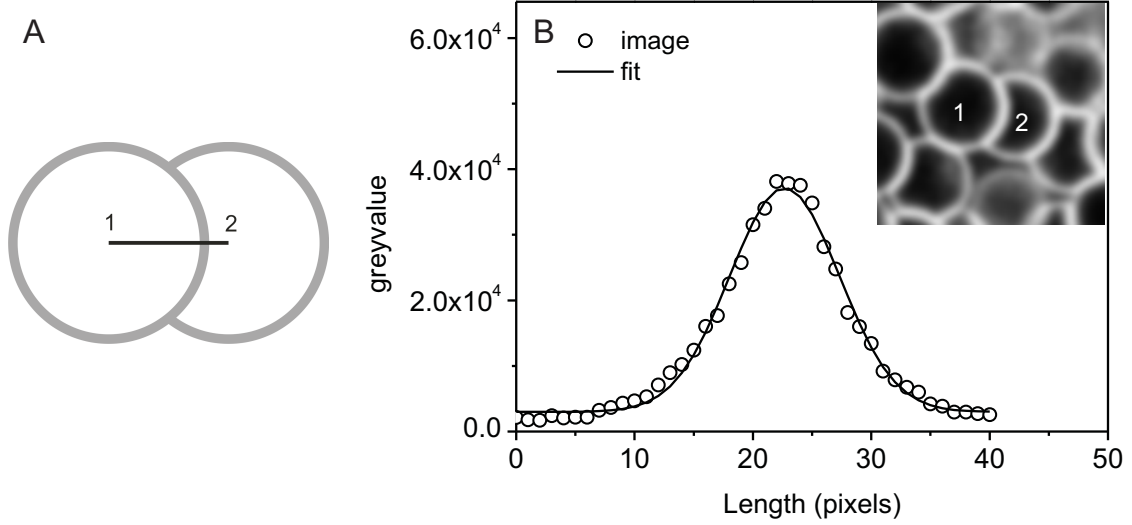


FIGURE 4.7. (A) Cartoon of a pair of hollow particles with particle 2 dimpled by particle 1 and a line connecting their centers. (B) The greyvalue distribution of pixels that make up the line of length 40 pixels, joining the 3D center of particles 1 and 2, in the inset confocal image. The line in the graph is a gaussian fit with peak center at 22.69 pixels.

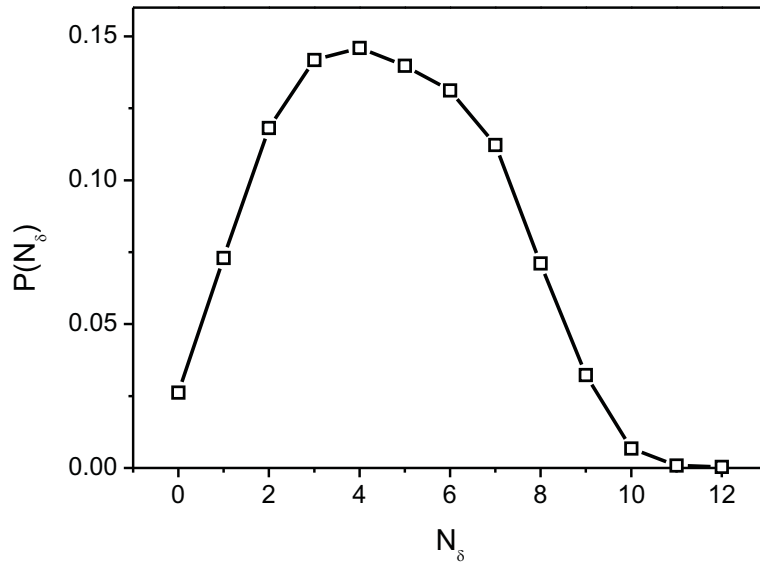


FIGURE 4.8. Distribution of number of dimples per particle (buckling number),  $N_\delta$  in a jammed packing of shells of volume fraction 0.908.

particle, one coordinate is decided by the slope of the line. The remaining two are determined by a decision variable that decides on one of the two choices for the next pixel in a line based on the relative positions of the true line and the midpoints of the pixels.

Before applying the algorithm the original confocal images in the stack were smoothed by a gaussian blur filter of  $\sigma = 3$  pixels. Figure 4.7 (B) is a greyvalue or intensity profile taken along the line that joins the 3D centers of particles marked 1 and 2 in the inset confocal image taken from a packing of volume fraction 0.908. In the profile circles denote the greyvalues of the pixels along the line connecting the centers, as obtained from the image. The line is the corresponding gaussian fit. The position of the center of the peak is found to be closer to particle 2 and hence particle 2 must be the dimpled particle, which is actually true. Similarly we identified the dimpled particles in all contact pairs in the whole packing. Out of 26131 contact pairs in this packing only 0.19% resulted in a wrong peak center and 4 pairs with position of peak at equal distance from the center of particles in a pair. Figure 4.8 shows the distribution of number of dimples per particle in this packing. On average there are 4.92 dimples per particle in this packing.

#### 4.4 CONCLUSIONS

We described an image analysis routine to identify the position of particles with a fluorescent elastic shell in a 3D jammed packing. The shells deform one another by producing dimples in their neighbors. The image processing results in a set of overlapping spheres that closely represents the experimental system. Using confocal microscopy we obtained 3D stacks of images. Images were processed in ImageJ software to detect the edges and thereafter analyzing the shape of the particles. This gave the 2D centers of particles distributed in the 2D slices. The 3D center of each particle in the full 3D data set was obtained by grouping the 2D centers and their respective radii and thereafter fitting a circle through the radii of each particle at different positions in the axial direction. A check for pixel biasing revealed the accuracy of the routine in finding the position of the particles with sub-pixel accuracy.

For the jammed packing of volume fraction 0.908, the radial distribution function was found to resemble a liquid phase with nearest neighbor distances less than the particle diameter, resulting from the deformation of the shell. Furthermore, we developed a routine to identify the dimpled particle in a contact pair by determining which particle center is closest to the intensity maximum of the shell. The buckling number  $N_\delta$  for the sample of volume fraction 0.908 was found to be 4.92. Knowledge of coordinates of the particles enable a systematic study of 3D jammed packings of elastic shells, including the structure and the contact forces, which will be described in the subsequent chapters.

#### 4.5 ACKNOWLEDGMENTS

We would like to thank Gerhard Blab for helping in modifying ImageJ algorithms, Anjan Gantapara for writing code for the grouping of the *SEC*'s and with Mathematica.

Also, we wish to thank Johan Stiefelhagen for providing the code for radial distribution function and Bas Kwaadgras for his help in solving programming related issues.

# 5

## 3D microstructure and contact forces in jammed packings of elastic shells - static compression

We report here a quantitative study of the 3D packing geometry and contact force network in monodisperse elastic shells under unidirectional compression. Unlike other experimental systems with soft deformable particles the shells were found to be deformed in such a way that the volume of the shell was not conserved. It was found that if two shells were forced into contact one of the two buckled reversibly and formed a spherical dimple at the contact region. From the depth of the dimple we determined the magnitude of the normal component of the contact force using the force law from the non-linear theory of elasticity of thin shells. The theory predicts a square root dependence of contact force on deformation. We found a heterogeneous distribution of the contact force magnitudes with little evidence of long-range force chains in the packings. The power law scaling of contact number and pressure with excess density showed a deviation from theoretical and computer simulation predictions. Another unique property that we investigated is the buckling number, i.e. the number of dimples per particle, which was found to show a similar scaling as that of the contact number with excess density.

## 5.1 INTRODUCTION

Jamming is a key feature of many disordered systems with slow relaxation dynamics such as granular materials, glasses, compressed emulsions and foams [29, 31]. For frictionless spheres at zero temperature and zero shear, interacting with finite-range repulsive potentials the onset of jamming occurs when the spheres just start to touch each other (but still at zero pressure) at a critical volume fraction  $\varphi_c$ , that was found to coincide with random close packing fraction  $RCP \approx 0.64$  [30, 157]. Above  $\varphi_c$ , the particles start to overlap and exert forces on each other. Hence the pressure becomes non-zero and the system starts to become rigid.

The distribution of contact forces  $P(f)$  between particle pairs has been studied in experiments and simulations, in both 2D and 3D [18, 19, 26–28, 30, 32, 33, 93, 129, 130, 133, 134, 157, 158]. The universal feature of the probability distribution  $P(f)$  of inter particle contact forces from these studies, is an exponential decay of forces above the mean value. Moreover, a transition to a Gaussian-like distribution has been observed for deformable soft particles, at higher volume fractions beyond  $\varphi_c$  [28, 93, 133, 159, 160]. Recently, in simulations and experiments, it has been reported that the mechanical and geometric properties of jammed packings of soft spheres show power law scaling with the excess volume fraction  $(\varphi - \varphi_c)$  [30, 92, 157, 161, 162]. The contact number  $Z$  is found to scale as  $(\varphi - \varphi_c)^\beta$  above  $\varphi_c$ , where  $\beta = 0.5$ , regardless of dimension and interaction potential [28, 30, 92, 132, 134, 157, 161–164]. The pressure is expected to scale as  $(\varphi - \varphi_c)^{\alpha-1}$  where the value of the exponent was found to depend on the interparticle force law [30, 92, 132, 134, 157, 161–163].

In this chapter we investigate the structure of, and contact force network in, dense 3D packings of  $5.47 \mu\text{m}$  diameter elastic monodisperse shells under static compression for a range of volume fractions, above the jamming threshold. This system constitutes a new experimental system to study the jamming transition that shares similarities with other systems, but differs in some respects, as is discussed in more detail below. The shells were fluorescently labeled, index matched and compressed by centrifugation in a capillary, after which 3D structure was investigated with confocal microscopy. In a dilute state shells underwent slight Brownian motion (self-diffusion coefficient =  $0.07 \mu\text{m}^2/\text{s}$ ), but when the density was increased particles came in close contact and were arrested in a jammed state. The interactions between shells are considered to be purely repulsive, since the shells remained spherical in the absence of compression and did not stick to each other.

Unlike other soft particles studied so far, the shells were found to be deformed in such a way that the volume of the shell was not conserved. This distinguishes them from emulsions and foams, jammed packings of which have also been studied [27, 28, 93, 134, 164]. In each contact, one of the shells buckled with a dimple at the contact region,

while the other one remained spherical. From the depth of the dimple, which can be quantified in 3D with a confocal microscope in combination with image processing (see chapter 4), we determined the magnitude of the normal component of the contact force using a force law from the non-linear theory of elasticity of thin shells [117, 118]. This theory predicts a square root dependence of the contact force on deformation. This differs from the harmonic force law that is used to describe emulsion droplets and foam bubbles [27, 28, 93, 134, 164], as well as the Hertzian force law applies to solid spheres for example glass beads. Moreover, we find that the deformation of our shells was reversible upon release of external stress. The shells are frictionless, but when they buckle with a dimple, a particle making an indentation remains locked inside the dimple of its neighbor and therefore tangential forces can come into action at high volume fractions.

For the present study we only consider the normal forces and we analyzed the distribution of contact forces normalized by the mean force for a range of volume fractions. From the contact forces and the distances between the particle pairs we determined the global pressure and how it scales with the packing density. The structure of dense packings of shells was also investigated by analyzing the radial distribution functions  $g(r)$  and the average contact number per particle. A check for any local order in these packings was also performed by calculating the local bond order parameter. In addition, we also studied the buckling number distribution of contacting particles, which is a unique property of this system.

## 5.2 EXPERIMENTAL METHOD

### 5.2.1 Sample preparation

Amorphous packings of fluorescently labeled (shells are prepared using the Turrax homogenizer method described in chapter 2) and index matched deformable shells at different volume fractions were obtained by centrifugation. We prepared two capillaries (capillary 1 and 2) from the same batch of particles for this purpose and a third from another batch (described below). The particles were  $R_t = 2.74 \pm 0.03 \mu\text{m}$  in radius with polydispersity  $\sim 3\%$  and shell thickness  $d = 56 \pm 2 \text{ nm}$  ( $d/R_t = 0.02$ ). The radius of the droplet template was measured by static light scattering (*SLS*) and the shell thickness was obtained from atomic force microscopy (*AFM*). For confocal measurements the shells were dispersed in an index matched solvent of 52.6% v/v dimethyl sulfoxide (*DMSO*) and 47.4% v/v ethanol. This mixture had a refractive index of 1.42. A few drops of concentrated suspension of shells were put in two capillaries of dimensions  $0.1 \times 2 \times 50 \text{ mm}$ , capillary 1, and  $0.1 \times 1 \times 50 \text{ mm}$ , capillary 2 (depth  $\times$  width  $\times$  length, VitroCom). A few millimeters on one side of both the capillaries was filled with candle wax. Both ends of the capillaries were then closed with UV glue (Norland, no.68) and

the glue was cured under UV lamp for 40 mins. The candle wax acted as a pedestal that lifted the whole sediment above the drop of glue.

Capillary 1 was centrifuged at 2000g for 10 min with the capillary length along the direction of gravity. This created a sediment of height 7 mm with higher densities of shells closer to the wax interface. The density decreased with increasing height in the sediment, moving away from the wax interface. In addition to serving as a support for the sediment, we found that the wax tended to take up a small amount of solvent resulting in some solvent leakage from the capillary during centrifugation. This solvent leakage further enhanced the density of the shells and their subsequent deformation near the vicinity of wax-sediment interface. The capillary still contained a surplus of solvent on top of the sediment after centrifugation.

Capillary 2 was centrifuged twice: at 2000g for 25 min and 1000g for 15 min, because after the first centrifugation there was no leakage of solvent and hence only a low volume fraction of the shells. After the final centrifugation a surplus of solvent was almost absent inside the capillary, as the pure solvent leaked through the wax. However, we found regions of high volume fraction of shells opposite to the sediment-wax interface. These high density regions perhaps resulted from the drainage of solvent and subsequent compression by capillary action. The height of the sediment in this capillary was approximately 14 mm.

Another capillary, capillary 3 (dimensions same as capillary 1) was prepared with a batch of shells of average radius  $R_t = 2.02 \pm 0.03 \mu\text{m}$  and shell thickness  $d \approx 90 \text{ nm}$  (both measured from *SLS*) with  $d/R_t = 0.04$ . These shells were prepared as described in chapter 3. The sample was centrifuged at 2000g for 10 min to obtain compressed shells.

### 5.2.2 Image analysis

3D image stacks of elastic shells of different packing densities were acquired from the capillaries 1 and 2 (a schematic of a typical capillary is shown in figure 5.1) from different heights in the sediment as described in chapter 4. Only one volume fraction was acquired from capillary 3. The capillary was mounted on a Nikon C1 confocal microscope with the microscope stage tilted 90 degrees with respect to gravity. This way the capillary could remain in an upright position so as not to disturb the packing. The first image stack was taken 5 h after centrifugation. Most of the image stacks, except the lower packing fractions were acquired within a duration of 1-3 days after sample preparation. During this period we didn't observe a noticeable relaxation of the shells in the sediment. The low density regions in the capillary were scanned randomly at various times within a period of 1 month. The capillary was kept undisturbed during this period. The height of the sediment was measured to be nearly the same as the original height during this period.

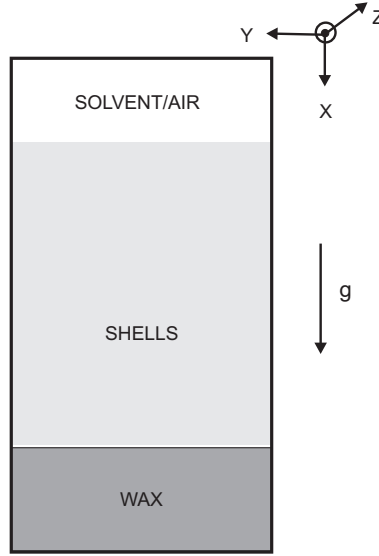


FIGURE 5.1. Schematic of the capillary after centrifugation. The shells sediment in the direction of the centrifugal field (as shown by the arrow next to  $g$ ). The leakage of solvent through the wax plug resulted in either a small amount of surplus solvent above the sediment or an empty space. During imaging the capillary was placed in an upright position with gravity pointing down (as shown by the arrow next to  $g$ ).

The coordinates of particles and their radii in each packing at different densities were obtained using the image processing routines explained in chapter 4. The error in coordinates of the particles are approximately 80 nm in  $X$  and  $Y$ , and 40 nm in  $Z$ . Table 6.1 gives an overview of each packing at different volume fractions obtained from all the capillaries. The radii of the particles (for the batch  $d/R_t = 0.02$ ) were measured to be almost the same for all packings with an average polydispersity about 6%. For all these packings the 3D imaging volume was fixed at  $99.94 \times 99.94 \times 86.43 \mu\text{m}^3$  taken with voxel size of  $0.0976 \times 0.0976 \times 0.1094 \mu\text{m}^3$  (for the one packing of shells of  $d/R_t = 0.04$  the volume was  $77.07 \times 69.96 \times 39.27 \mu\text{m}^3$  taken with voxel size of  $0.0846 \times 0.0846 \times 0.1094 \mu\text{m}^3$ ).

The volume fractions of these packings were calculated by summing the volumes of the spheres and subtracting their overlap volume in an image volume of  $(99.94 - 2R_t) \times (99.94 - 2R_t) \times 66 \mu\text{m}^3$ . Here,  $R_t$  corresponds to the average radius of the particle obtained from image analysis for each packing fraction. The image size was reduced by  $R_t$  from all sides in the  $X$  and  $Y$  directions to compensate for the particles that are missing near the edge (not identified during image analysis). Note that a particle near the edge is only identified if its full volume resides inside the image volume. In addition to that, we also avoided about four layers of particles in the  $Z$  direction due to slight ordering near the wall. The error in the absolute value of volume fraction due to the

reduction of image volume by  $R_t$  to compensate for the missing particles near the edge is rather low, approximately 0.005. But the value of volume fraction obtained from the image analysis is highly sensitive to the radius of the particles obtained [165]. Therefore, the absolute volume fraction may contain an error of about 0.04. The lowest volume fraction that we could analyze where the particles in the image volume remained static, except for a few rattlers, was about 0.663. Some of these particles were undergoing Brownian motion in the void space between contacts. Most of these particles were identified using the algorithms.

### 5.3 RESULTS AND DISCUSSIONS

#### 5.3.1 Microstructure of compressed shells

##### *Radial distribution function $g(r)$*

From the particle coordinates we calculated the radial distribution function  $g(r)$ , which is the probability of finding a particle at a distance  $r$  from a given reference particle [1]. Figure 5.2 shows  $g(r)$  for shells ( $d/R_t = 0.02$ ) compressed at different volume fractions  $\varphi$ . The shape of the distribution resembles the structure of a liquid, but was less well-defined than that of a hard sphere packing at the same  $\varphi$  [140, 166]. Besides, the amplitude of the peaks decayed and the width of the peaks increased with increasing  $\varphi$ . This behavior is just the opposite to that of liquids, which have  $\varphi$  lower than the jamming point. The  $g(r)$  of the  $\varphi = 0.663$  peaks at  $r = D$  ( $D$  is the diameter of particle), confirming that this packing is close to the jamming point. The full width half maximum of this peak is  $0.08D$ , which is nearly equal to the sum of the polydispersity ( $0.06D$ ) in radii of the particles and the error in the determination of the distance between the centers of the two particles ( $2 \times 80 \text{ nm}$ , or  $0.027D$ ). Moreover, the first peak of  $g(r)$  occurred at radial distances,  $r/D \leq 1$  and also shifted to even smaller distances as the volume fraction is increased in the packing. The shift and broadening of the first peak upon increasing the density resulted from the increase in deformation of the shells by their contacting neighbors. Similar behavior of  $g(r)$  was predicted in simulations on soft granular particles [30, 160, 167]. The small sharp peaks near  $r/D \approx 0$  are the contributions from the small fraction of incorrectly identified (false) particles ( $< 2\%$ ) by our image analysis procedures (Table 6.1).

For two of the packings, the one at  $\varphi = 0.810$  and another at  $\varphi = 0.835$ , the position and width of the first peak of  $g(r)$  do not fall in the trend displayed by the other samples. Besides,  $\varphi = 0.810$  showed a split second peak (shown also in the inset) which was not seen in  $\varphi = 0.835$ . The splitting of second peak has been reported for hard-sphere glasses [168–170], but is known to occur close to the glass transition, which is not the case here. In a recent simulation by Silbert *et.al.* [167] a similar split second peak was observed in  $g(r)$  for a zero-temperature, disordered, monodisperse soft-sphere

Image stack	No. of particles	false (incorrect) particles(%)	No. of contacts	$R_t(\mu\text{m})$	$\phi$	$\langle F \rangle$ ( $\mu\text{N}$ )
$S1^*$	6417	1.3	29117	2.928	0.892	0.082
$S2^*$	6093	1.85	28210	2.926	0.913	0.079
$S3^*$	5955	1.9	26682	2.958	0.900	0.079
$S4^*$	5844	1.3	25473	2.956	0.895	0.078
$S5^*$	5753	1.4	26131	2.952	0.908	0.077
T1	3810	1.2	17774	2.171	0.906	0.289
$S6^*$	5737	1.8	25084	2.962	0.897	0.078
S7	5307	1.65	24368	3.002	0.888	0.074
S8	5163	1.16	22996	2.991	0.883	0.071
$S9^*$	4964	1.2	21094	2.962	0.852	0.070
$S10^*$	4714	0.9	19581	2.954	0.835	0.065
S11	4570	0.37	18154	2.967	0.806	0.060
$S12^*$	4552	0.8	18522	2.948	0.810	0.062
S13	4475	1	17751	2.948	0.793	0.059
S14	4339	0.25	17113	2.968	0.791	0.058
S15	4294	1	16178	2.942	0.765	0.057
S16	4264	0.9	15694	2.938	0.763	0.055
S17	4254	0.18	16388	2.967	0.776	0.056
S18	4196	0.7	14992	2.937	0.752	0.053
S19	4084	0.6	13722	2.926	0.726	0.050
S20	4030	0.39	12985	2.929	0.721	0.048
S21	4024	0.54	13691	2.934	0.723	0.049
S22	3913	0.3	11903	2.922	0.701	0.046
S23	3889	0.35	11733	2.925	0.699	0.046
S24	3933	0.7	11375	2.930	0.693	0.048
S25	3828	0.47	10380	2.919	0.677	0.045
S26	3647	0.13	8495	2.933	0.663	0.037

TABLE 5.1. The details of image stacks of different densities obtained from image analysis algorithms from capillaries 1 and 2, containing shells of  $d/R_t = 0.02$ . Stacks highlighted by \* were taken from capillary 2 and the image stack T1 corresponds to sample of shells of  $d/R_t = 0.04$  (capillary 3).

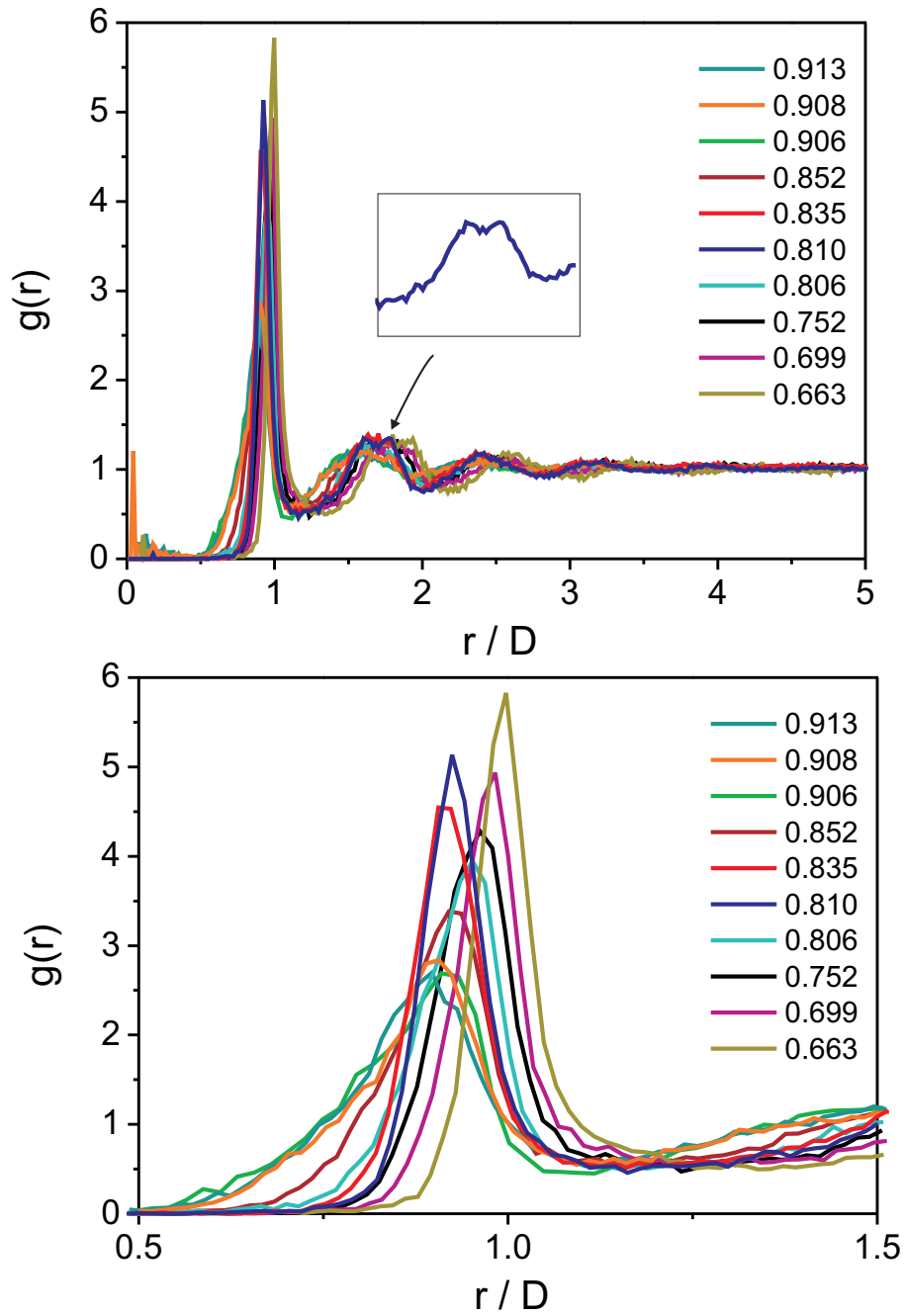


FIGURE 5.2. Radial distribution function of compressed deformable shells for a range of experimental volume fractions. The radial distances for each packing is normalized by their corresponding average particle diameter obtained from image analysis. Inset figure shows the split second peak of  $\varphi = 0.810$  packing. Volume fraction  $\varphi = 0.906$  represents the shells with shell thickness to diameter ratio,  $d/R_t = 0.04$ . The bin size is 0.1.

packing at the jamming/unjamming transition. However, this split second peak has not been observed in experimental jammed systems of monodisperse spheres, for example in monodisperse soft colloidal particles made from a thermosensitive hydrogel [171]. The splitting in the second peak was reported to be a likely indication of local order in the particle positions [170]. But, upon visualization of the 3D image stack we did not see a local crystalline order in these packings. So to quantitatively measure the degree of the local symmetry involved in these packings compared to others, we performed a local bond order calculation as follows.

The bond orientational order parameters of a particle  $i$  is defined by a complex vector,

$$q_{lm}(i) = \frac{1}{N_b(i)} \sum_{j=1}^{N_b(i)} Y_{lm}(r_{ij}) \quad (5.1)$$

where  $N_b(i)$  is the number of nearest neighbors of particle  $i$ ,  $r_{ij}$  is the vector from the center of particle  $i$  to particle  $j$  and  $Y_{lm}$  are the spherical harmonics (with  $m = -l$  to  $m = +l$ ). The sum runs over all neighbors of particle  $i$ . Neighbors are usually defined as all particles that are within a given cut off distance around a particle. To distinguish between a disordered and a crystalline environment of a particle  $i$  from these sets of bond orientational order parameters, we calculated both the local bond order parameter (Steinhardt order parameter)  $q_l(i)$  [172] and the average of bond orientational order parameters from equation 5.1 over particle  $i$  and all its neighbors *i.e.*  $\bar{q}_l(i)$ , following the method of Lechner and Dellago [173]. The distributions of the averaged local bond order parameter are narrower because of the averaging and the fact that it takes into account the second shell of neighbors, whereas the Steinhardt order parameter is limited to the first shell. Hence, this makes it also suitable for identifying the type of crystal structure.

The Steinhardt local bond order parameter is,

$$q_l(i) = \sqrt{\frac{4\pi}{2l+1} \sum_{m=-l}^l q_{lm}(i)^2} \quad (5.2)$$

and its averaged form is,

$$\bar{q}_l(i) = \sqrt{\frac{4\pi}{2l+1} \sum_{m=-l}^l |\bar{q}_{lm}(i)|^2} \quad (5.3)$$

where,

$$\bar{q}_{lm}(i) = \frac{1}{N_b(i) + 1} \sum_{j=0}^{N_b(i)} q_{lm}(j) \quad (5.4)$$

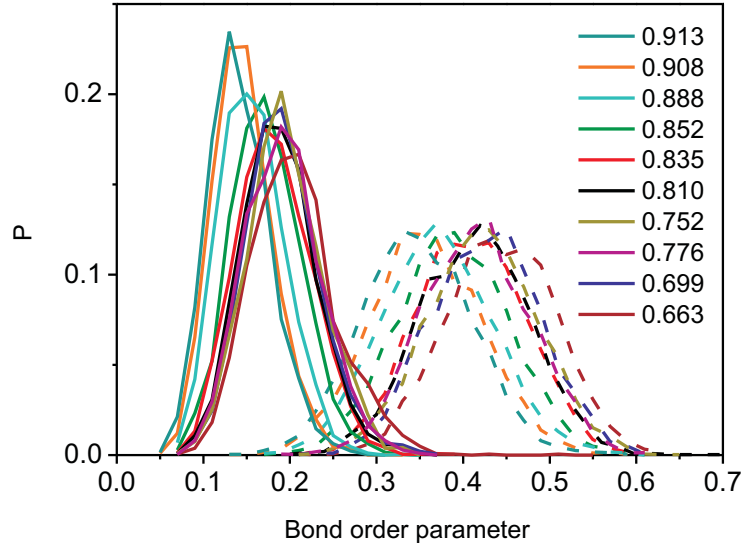


FIGURE 5.3. Probability distribution of  $q_6$  (dashed lines) and  $\bar{q}_6$  (solid lines) in a packing of elastic shells for a range of volume fractions. The bin size is 0.02.

Here, the sum runs over all neighbors of particle  $i$  plus the particle  $i$  itself. The cut off distance that we set for the present system was taken to be the position of the first minimum in the  $g(r)$  ( $r/D = 1.24$ ). The results of local bond order parameter  $q_6$  (dashed lines) and its averaged form  $\bar{q}_6$  (solid lines) are shown in the figure 5.3. The values of the order parameter tend to be higher when the local order resembles a bcc or fcc crystalline structure and the values are lower when the local environment is a glass or fluid-like [174]. As expected, the distribution of  $q_6$  is relatively broad compared to  $\bar{q}_6$ , making it difficult to distinguish between amorphous and crystalline structures, but from both distributions it seems like there is little or no order in these packings. Besides, the distribution for various volume fractions are well distinguishable from one another and shift to lower  $q$  values with increasing volume fraction, indicating that the packings became more disordered at higher compression. Apparently, this time all the volume fractions follow the same trend (in both  $q_6$  and  $\bar{q}_6$ ), including  $\varphi = 0.810$  and  $\varphi = 0.835$  that showed a different behavior in  $g(r)$  that pointed towards a more crystalline order compared to other packings. But that is not reflected in the local bond order parameter which is also supported by a visual inspection, which is not as we expected and presently not yet fully understood.

*Contact number ( $Z$ ) and buckling number ( $N_\delta$ )*

Another geometric feature that describes the structure of an amorphous packing is the number of contacts per particle  $Z$ . We determined the number of contacts for each shell from the coordinates of their centers and radii. A pair of particles is considered

Fit parameter	with rattlers		without rattlers	
	$\varphi_{exp}$	$\varphi_{th}$	$\varphi_{exp}$	$\varphi_{th}$
$Z_0$	$11.395 \pm 0.747$	$6.613 \pm 0.033$	$10.818 \pm 0.531$	$6.506 \pm 0.262$
$\varphi_c$	$0.683 \pm 0.003$	$0.700 \pm 0.005$	$0.681 \pm 0.003$	$0.695 \pm 0.004$
$\beta$	$0.681 \pm 0.041$	$0.490 \pm 0.038$	$0.653 \pm 0.030$	$0.485 \pm 0.030$

TABLE 5.2. Values of fit parameters obtained from the power law fit of scaling of  $\langle Z \rangle$  with both experimental and theoretical volume fractions.

as a contact pair if the distance between their center is less than or equal to the sum of their radii. The chances of missing a contact in our system are determined by the resolution in finding the particle position, which is less than one pixel, about 80 nm. The distributions of the contact number  $Z$  for a few samples at different volume fractions are shown in figure 5.4A. Only particles that are at least one particle diameter away from the edges of the image volume were considered for the  $Z$  distribution. This is to avoid an under-estimation of the average contact number, as there will be many contacts that are missing for the particles identified near the edge. In figure 5.4A, with increasing volume fraction the peak of the distribution shifts to higher values of  $Z$ . Furthermore, the distribution is almost symmetric for all volume fractions. The particles with fewer than 4 contacts in the lowest volume fraction samples, for  $\varphi < 0.726$ , represent the rattlers present in the system, which completely vanish at higher compression.

Next, we investigated the scaling of the average contact number  $\langle Z \rangle$  with volume fraction  $\varphi$ , moving away from the jamming point to higher densities. Numerical studies on jamming of frictionless systems found that the contact number obeys a universal power law scaling of the form  $Z - Z_c = Z_0(\varphi - \varphi_c)^\beta$ , where  $\beta = 0.5$  for all potentials, dimensions and polydispersities [30, 164].  $Z_c$  is the contact number at the jamming point, or critical volume fraction  $\varphi_c$ . For frictionless particles this is equal to the isostatic value (minimum number of contacts required for mechanical stability),  $Z_c = 2D$ , where  $D = 3$  is the dimension of the system. Figure 5.4B is the plot of  $\langle Z \rangle$  with the experimental volume fraction ( $\varphi = \varphi_{exp}$ ) obtained by subtracting the overlap volume from the total volume of the spherical shells. The plot also contains contact numbers measured by excluding the rattlers (marked in \*). Except for the lowest volume fraction  $\varphi_{exp} = 0.663$  the difference in  $\langle Z \rangle$  is rather negligible. We fix the value of  $Z_c = 6$  and fitted the data points including the rattlers and avoiding the data point at  $\varphi = 0.663$ , since the measured  $\langle Z \rangle$  was less than the isostatic value 6 ( $\langle Z \rangle = 5.15$  (with rattlers) and  $\langle Z \rangle = 5.65$  (without rattlers)) with the above mentioned power law equation. Table 5.2 shows the values of the fit parameters with and without rattlers. The values are nearly the same in both cases. The relatively high value of  $\varphi_c = 0.683 \pm 0.003$  compared to random close packing *RCP* (0.64) results most likely from the

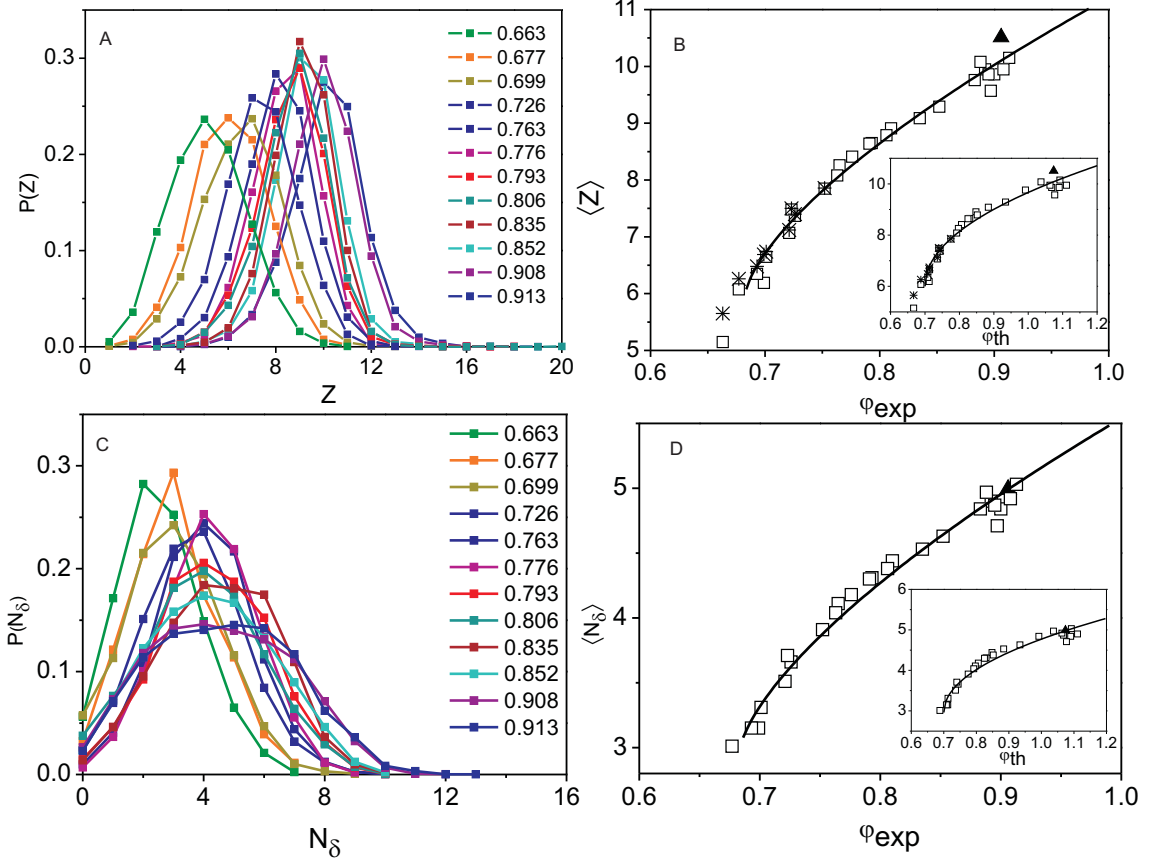


FIGURE 5.4. (A and C) Distribution of contacts per particle,  $Z$ , and number of dimples per particle,  $N_\delta$ , for a range of experimental packing fractions in the sample of shells of  $d/R_t = 0.02$ . (B) Scaling of the average contact number,  $\langle Z \rangle$  with experimental volume fractions  $\phi_{exp}$ . Solid line is a fit of the form  $\langle Z \rangle = 6 + Z_0(\phi - \phi_c)^\beta$ , with an exponent  $\beta = 0.681$ . The data marked in \* denote the average value of  $Z$  without rattlers. (D) Scaling of the average number of dimples,  $\langle N_\delta \rangle$  with experimental volume fraction. Solid line is a fit of the form  $\langle N_\delta \rangle = 6/x + Z_0/x(\phi_{exp} - \phi_c)^\beta$  which gives  $x = 2.024$ . Inset plots in (B and D) represent scaling of  $\langle Z \rangle$  and  $\langle N_\delta \rangle$  with theoretical volume fractions (see text for explanation). The solid triangle in the scaling plots corresponds to the sample of shells of  $d/R_t = 0.04$ .

uncertainty in the absolute value of the volume fraction obtained from image analysis. Note that an error of just 2% in the microscope's calibration can already account for this difference in volume fraction. Since, all the volume fraction values will have the same systematic deviation, the exponent of the scaling should not be affected by the error in  $\phi$ .

The obtained value of the scaling exponent  $\beta = 0.681 \pm 0.041$  is slightly higher than the value obtained in simulations, which is  $\beta = 0.50$ . The value of the prefactor

(Table 5.2) is also higher than the reported simulation value  $Z_0 = 7.7$  [30] but close to the value found in 3D compressed polydisperse emulsion  $Z_0 = 10.6$  [163]. In the recent article on 2D foams by Katgert and van Hecke [28] nearly the same value of  $\beta = 0.70$  was reported for the scaling of  $\langle Z \rangle$  with experimental volume fraction. But these authors also suggested that this results from the discrepancy between the way in which  $\varphi$  is calculated in simulations and in experiments. In simulations the volumes of the spheres are fixed and the volume fraction is calculated by counting the number of particles in the periodic box. So when spheres overlap, the overlap volume is counted double which is only counted once in the experiment and this leads to higher values of  $\varphi$ . With theoretical  $\varphi$  they obtained a scaling exponent  $0.50 \pm 0.020$  [28], in excellent agreement with simulations.

Similarly to compare with simulations we convert our experimental  $\varphi$  to theoretical value  $\varphi_{th}$  by adding the overlap volume to  $\varphi_{exp}$  ( $\varphi_{th} = \varphi_{exp} + V_{overlap}/V_{total}$ ), which gives values higher than unity. With  $\varphi_{th}$  we found a similar power law scaling of  $\langle Z \rangle$ , shown in the inset plot with exponent  $0.490 \pm 0.038$ , in good agreement with numerical simulations [30,164] and 2D experiments on frictional particles [132], frictionless systems like foams [28] and emulsions [134,163]. Note that in 2D frictional disks [132] and 3D emulsions [163] a value of  $\beta$  close to 0.50 was found using the experimental volume fraction, without applying the double counting of overlap volume. In 2D frictional disks [132] the scaling of  $\langle Z \rangle$  was analyzed for a small range of volume fractions ( $(\varphi - \varphi_c) \sim 0.01$ ) and within this range  $\varphi_{exp}$  and  $\varphi_{th}$  remained nearly the same. Instead, for 3D emulsions  $(\varphi - \varphi_c) \sim 0.2$ , the same as in our system of shells. However, in emulsions the volume of the droplet is conserved, which is not the case for our shells. We suspect this may be the origin of the higher exponent found in our system of shells.

Since at each contact only one of the shells is dimpled and the other remains spherical, we expect that the average number of dimples *i.e.* the buckling number is half the average number of contacts. And so we expect a similar power law scaling for  $\langle N_\delta \rangle$  with volume fraction. The shells with dimples are identified based on the method described in chapter 4. Figure 5.4D is a plot of the scaling of  $\langle N_\delta \rangle$  with the experimental volume fraction. The line is a power law fit of the form  $\langle N_\delta \rangle = 6/x + Z_0/x(\varphi - 0.683)^{0.681}$ , where only  $x$  was varied. The best fit gives the value of  $x = 2.024 \pm 0.008$ , as predicted. For the theoretical volume fraction  $\varphi_{th}$  a value of  $x = 2.026 \pm 0.012$  was found, inset plot in figure 5.4D.

While the average dimple number is simply half the average contact number, there is no such relation between their distributions. The plots of the distribution of the number of dimples per particle,  $N_\delta$ , at different volume fractions are shown in figure 5.4C. Clearly, for a particle with an average number of contacts, all or none of the contacts or any number in between may result in a dimple. Therefore, the width of the dimple distribution should be wider than half the width of the contact number

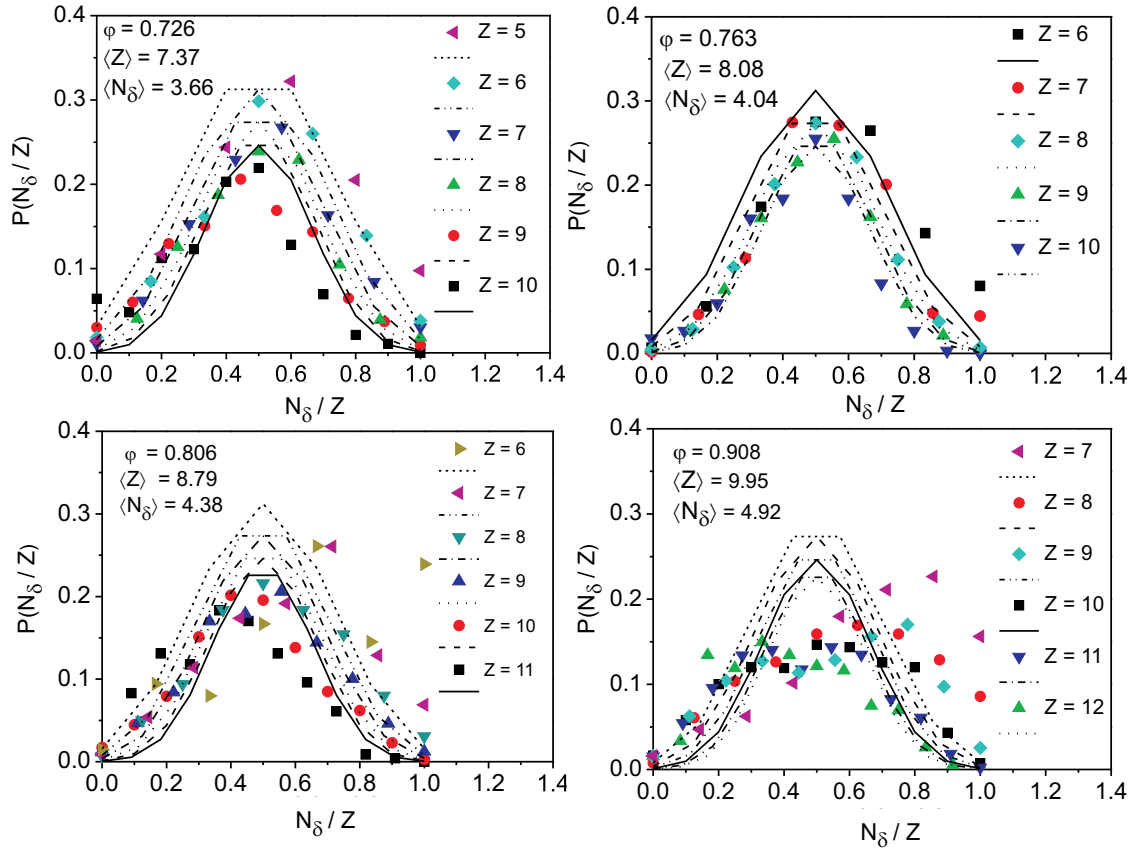


FIGURE 5.5. Distribution of fraction of contacts that result in a dimple for volume fractions  $\phi = 0.726$ ,  $\phi = 0.763$ ,  $\phi = 0.806$  and  $\phi = 0.908$ . Symbols indicate probability of  $N_\delta/Z$  for experimental value of  $Z$  and the lines denote the binomial distribution.

distribution. This is indeed found to be the case. From the distribution of dimples it is not quantitatively clear yet what fraction of contacts of a particle results in a dimple, and if dimpling one way or the other is a random process. So we determined the probability distribution of the fraction of contacts that leads to a dimple ( $N_\delta/Z$ ) among all particles with the same contact number in the packing at four different volume fractions (figure 5.5). The symbols indicate the probability of  $N_\delta/Z$  for experimental value of  $Z$ . The lines correspond to a binomial distribution, which in this case is the discrete probability of getting  $N_\delta$  dimples out of  $Z$  contacts given by the form  $P(N_\delta, Z) = Z!/((N_\delta!)(Z - N_\delta)!)p^{N_\delta}(1 - p)^{(Z - N_\delta)}$  ( $p = 0.5$ , the probability for a contact of a particle to become a dimple).

For the lowest volume fractions  $\phi = 0.726$  and  $\phi = 0.763$  the shape of the distribution of fraction of dimpled contacts is in reasonably close agreement with their respective binomial distributions, especially for the value of  $Z$  equal to the average value  $\langle Z \rangle$  in the packing. For higher volume fractions the deviations from the binomial distribution

become significantly larger, indicating that dimpling becomes non-random. For particles with a number of contacts above or below the average the distribution shows the most deviation from the random probability: the distribution became asymmetric. For  $Z < \langle Z \rangle$  the probability is high at large values of  $N_\delta/Z$  and for  $Z > \langle Z \rangle$  the probability is high at small values of  $N_\delta/Z$ . This means that particles with a small number of contacts tend to receive more than their fair share of dimples. Instead, particles having a large number of contacts tend to make a dimple on their neighbors. This behavior can be understood from the fact that the volume enclosed by the shells is not conserved. A particle with many dimples will have a smaller size and can therefore accommodate only a small number of contacting neighbors. Conversely, a particle that has almost no dimples has its original size and is therefore in contact with more than the average number of neighbors.

### 5.3.2 Contact forces in compressed shells

#### *Force law*

In a system of compressed spherical elastic shells, the shells become deformed at regions where they are in contact with each other. Figure 5.6A and B shows confocal images of compressed shells ( $d/R_t = 0.02$ ) at volume fractions  $\varphi = 0.699$  and  $\varphi = 0.908$ . At low  $\varphi$  the deformation of the shells were not prominent; obviously in the image there is no noticeable change in the shape of the contact region. However, for  $\varphi = 0.908$  the shells were clearly deformed and the contact regions were buckled with shells making or receiving an indentation from their neighbors. By measuring the depth of the indentation *i.e.* overlap width between the contact pairs  $\delta$ , we determined the magnitude of the inter particle force at each contact. For a pair of shells of radii  $R_i$  and  $R_j$  the overlap width  $\delta_{ij}$  is given by

$$\delta_{ij} = (R_i + R_j) - \ell_{ij} \quad (5.5)$$

where  $\ell_{ij}$  is the distance between their centers.

The force law we used to determine the magnitude of normal contact force is derived from the theory of elasticity of thin shells [117, 118]. Under a small localized load a thin elastic shell is predicted to respond linearly to the indentation magnitude up to about the shell thickness ( $d$ ). Beyond this regime the shell undergoes *mirror buckling*. This leads to an inversion of curvature of the shell *i.e.* the formation of a dimple at the contact region. The major part of the elastic energy is then concentrated in the *bending strip* near the edge of the dimple, whose radius grows with the indentation. The magnitude of the applied force is then proportional to the square root of the indentation,

$$F \sim E \frac{d^{5/2}}{R} \sqrt{\delta} \quad (5.6)$$

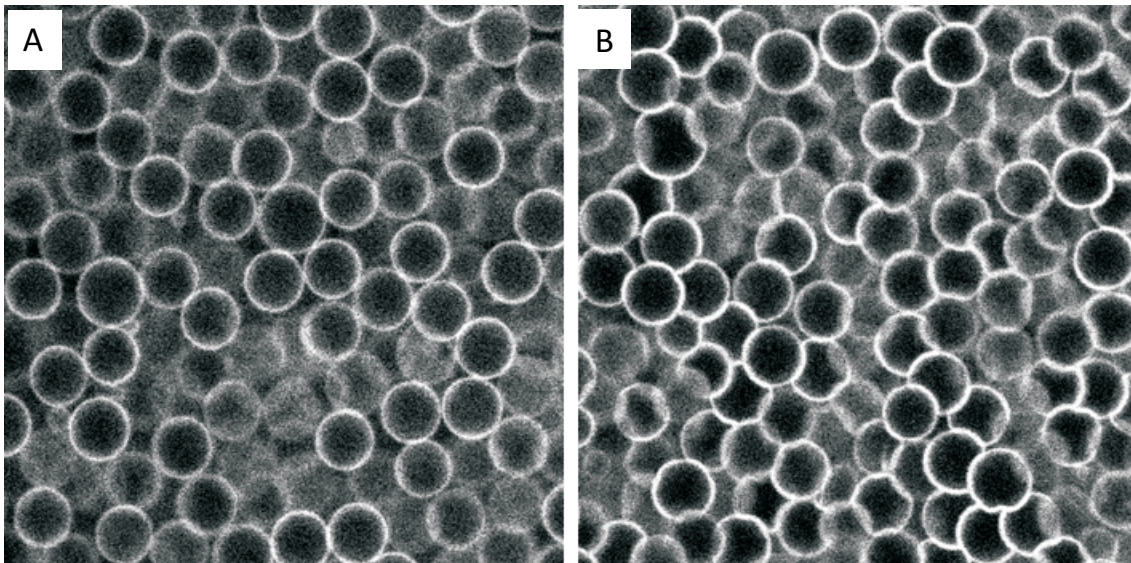


FIGURE 5.6. Confocal pictures of shells at volume fractions (A)  $\varphi = 0.699$  and (B)  $\varphi = 0.908$ . Image size is  $550 \times 550$  pixels.

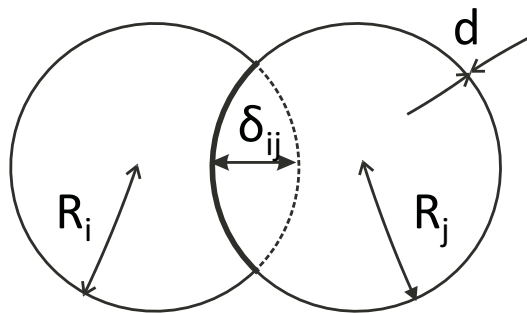


FIGURE 5.7. Schematic of a contact pair where, particle  $j$  of radius  $R_j$  makes an indentation in particle  $i$  of radius  $R_i$ . The depth of the indentation is  $\delta_{ij}$  and  $d$  is the thickness of the shell.

where  $E$  is the Young's modulus of the shell,  $R$  is the radius of the particle. The above solution for the deformation of a shell was obtained through a geometric approach and following the assumption that the applied load is conservative, i.e, the work it performs under deformation of the shell depends only on the final shape and not on the path it followed [117, 118]. Equation 5.6 was derived for a point load but the final shape is a spherical dimple, which is the same as for a pair of contacting equal-sized spheres. If the shape is the same as for a point contact, the elastic energy is also the same (if it is conservative). Then the restoring force between the spheres is the same as the force applied by a point load, as it is the derivative of the elastic energy. We therefore expect equation 5.6 to hold in our experiment, where two spherical shells of almost equal radii and elasticity are in contact and only one of the shells is dimpled at the contact point

as shown in figure 5.7. The precise form of equation 5.6 was derived by Pogorelov [118]. Thus, for a contact pair with overlap depth  $\delta_{ij}$ , the magnitude of the contact force is,

$$F_{ij} = \frac{0.534\pi}{1 - \nu^2} \frac{Ed^{5/2}}{\sqrt{R}} \sqrt{\frac{\delta_{ij}}{R_{ij}}} \quad (5.7)$$

Where the Poisson ratio,  $\nu = 0.3$  and Young's modulus  $E = 200$  MPa [116]. To obtain more accurate forces we use the ratio  $\delta_{ij}/R_{ij}$  obtained from the microscope data, and  $R$  from the (more accurate) light scattering measurement.

In the case of a large deformation of a closed spherical shell the question of their permeability or volume conservation must also be considered [175]. The volume of an impermeable shell with an incompressible fluid is constrained. This leads to an additional restoring force arising from the stretching of the shell to keep its volume conserved while the particle is deformed. This contribution to the force is proportional to the third power of the indentation [175],

$$F \sim \frac{2\pi}{3} \frac{Ed}{R^2} (\delta)^3 \quad (5.8)$$

Clearly in the packing of elastic shells filled with index matched solvent, the shells were fully permeable to the solvent on the time scale of deformation, which resulted in the formation of dimples. However, if instead of solvent filled shells, shells filled with polydimethylsiloxane (*PDMS*) oil were compressed, the content could not leave the shells to mix with the index matching water/glycerol mixture, and the shells had to deform in such a way as to conserve their inner volume. Figure 5.8 B is a confocal image of shells filled with *PDMS* oil confined between two glass plates. Clearly in this volume conservation deformation case, the deformation is completely different. The shells are flattened at the contact regions and are bulged at non-contact areas. The final shape of the shell was similar to that of the oil droplets in compressed emulsion [27,93]. From experiments on the release of oil from inside the shell by micelles it had become evident that the shells were permeable to the inner oil (chapter 3). However, in the compression experiment there were no micelles to solubilize that oil and therefore the shell acted like an impermeable membrane for the oil inside.

Furthermore, for volume fractions of shell, close to the jamming threshold, we expect majority of contacts where shells are deformed by only a small force. From elasticity theory, for a small deformation the force should vary linearly with indentation magnitude [176,177],

$$F = \frac{2}{\sqrt{3(1 - \nu^2)}} Ed^2 \frac{\delta_{ij}}{R_{ij}} \quad (5.9)$$

Theoretically, the value of overlap depth  $\delta_{ij}$  where the linear and the square root behavior of force intersect is at about twice the shell thickness. However, from *AFM*

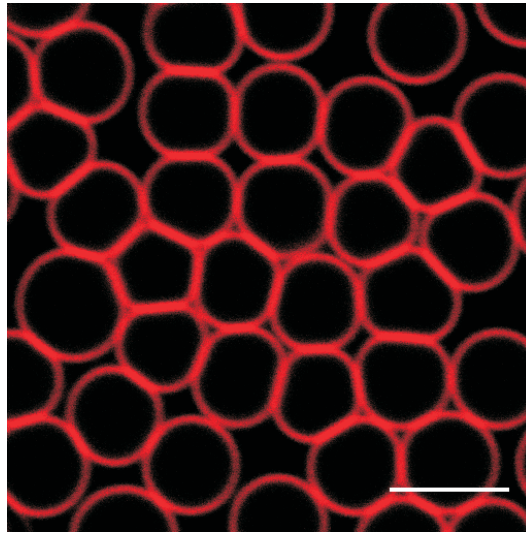


FIGURE 5.8. Confocal image of shells filled with *PDMS* oil, dispersed in an index matched water/glycerol mixture, confined between two glass plates. The red contours are the shell. The deformation of these shells were completely different from that in the force measurements. The scale bar represent  $5 \mu\text{m}$ .

experiments [116] on our shells this transition was measured at an indentation depth close to the shell thickness  $d$ . Therefore, we checked the fraction of contacts in all the packings at different densities for which,  $\delta_{ij} < 2d$  and  $\delta_{ij} < d$ , shown in figure 5.9. At low volume fractions the number of contacts with  $\delta_{ij} < 2d$  is rather high, but decreased rapidly with increasing volume fraction. Though there is a high fraction of contacts below  $2d$ , the magnitude of forces obtained from the linear and non-linear force law are not too different for these small deformations. Thus, in principle the distribution of the contact force magnitudes should be unaffected by this transition. However, attempting to use the correct force law for the small forces led to artificial kinks in the force distributions. To avoid this we decided to stick with the non-linear square root law for determining the contact force for all the contacts in our compressed shells.

#### *Extreme compression - Wrinkling of shells*

Here we discuss our observations on extremely compressed shells that are highly deformed inside the capillary. This takes place beyond the volume fractions we used for the force network analysis. Figure 5.10 shows a series of confocal pictures of jammed shells with increasing density near the capillary wall (A and B) and in the bulk (C and D). As expected, the shells are deformed at contact regions where one of the shells is dimpled by the other as shown in figure 5.10A at a volume fraction,  $\varphi = 0.908$ . There are many shells that remain spherical, making indentations in their neighbors in the 2D image. Moreover, there are still void spaces between the shells; that means the packing can go further to higher densities. Now, if the shells are compressed further, they come

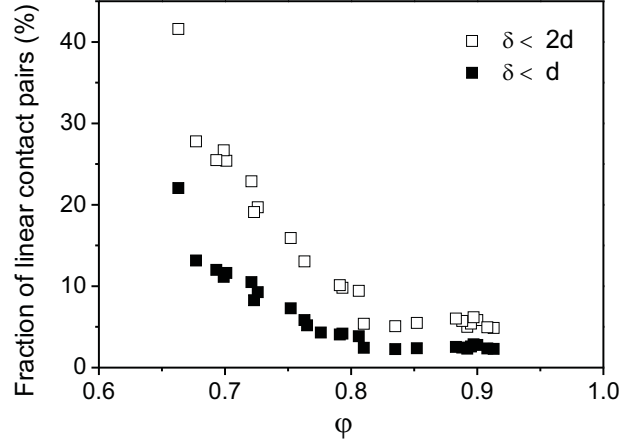


FIGURE 5.9. Plot of fraction of contacts below  $\delta = d$  and  $\delta = 2d$  for different volume fractions.

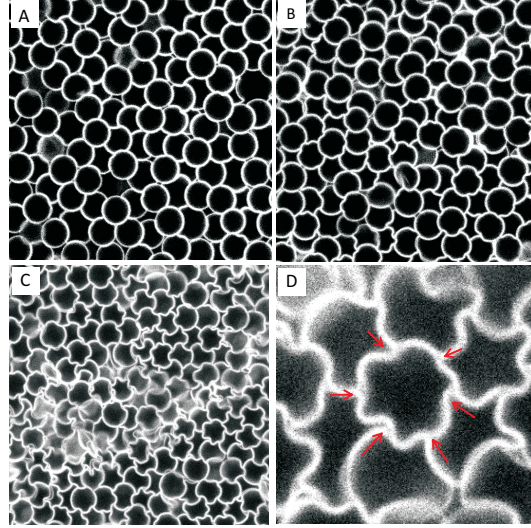


FIGURE 5.10. Confocal images of jammed shells with increasing volume fraction, near the capillary wall at (A)  $\phi = 0.908$  and (B)  $\phi = 0.895$ . (C) Image taken from bulk at even higher compression  $\phi = 1$  (not considered for force analysis) and (D) a zoomed in view of a shell with wrinkles. The arrows points to the dimple created on this shell by its neighbors.

closer to each other, occupying nearly all the interstitial spaces, shown in figure 5.10B. In this sample there were a few shells whose contour appeared to be slightly wrinkled. By "wrinkle" we mean the formation of more than one dimple at the contact region between a contact pair. The new dimples were formed on the shells which initially remained spherical at the contact region. They appear to have formed when one of the shells invaded the remaining interstitial space. In this case the square root relation of contact force on depth of the indentation between a pair of particles, with one dimple,

cannot be expected to be valid anymore. Moreover, the image analysis routines become unreliable for these shapes. For this sample volume  $\varphi = 0.895$ , though this  $\varphi$  value obtained from image processing is slightly lower from the expected value, the wrinkling of shells was not yet prominent in the bulk. So, we still included this packing for contact force analysis.

However, at even higher compression, almost all the shells started to wrinkle, even in the bulk and formed a highly interlocked cogwheel-like structures, shown in figure 5.10C. This image was taken in the bulk. This high packing fraction of shells, which must be close to unity was partly obtained by slow solvent evaporation. Figure 5.10D is a zoomed in picture of a shell with six neighbors in one plane. The arrows points to the dimples formed on this shell by its neighbors. The dimples were most likely created by the force exerted by the sharp cusp of neighbor particles. Samples with this high compression were excluded from the analysis.

#### *Relaxation of compressed shells*

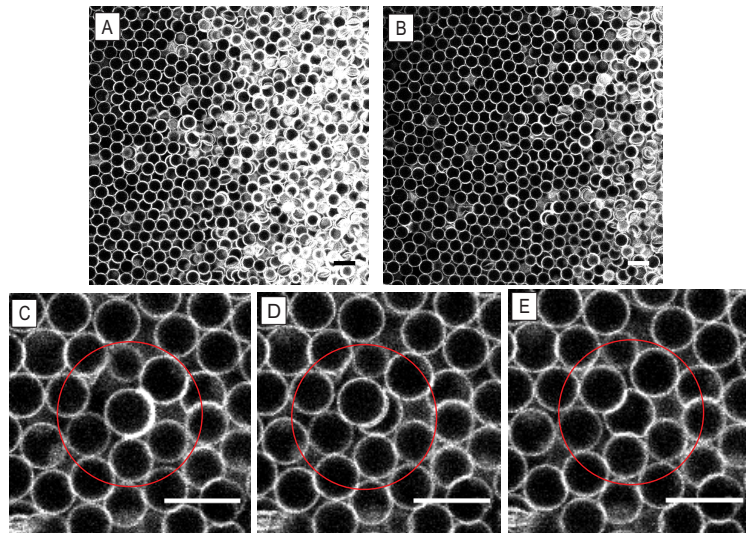


FIGURE 5.11. Confocal images of compressed shells upon release of stress. (A) Shells in the sediment close to the wax interface. (B) Same spot taken 40 mins after image (A). Elastic recovery of a highly deformed shell from a bowl shape to almost spherical shape at (C) 0 sec, (D) 38 sec and (E) 76 sec. All the scale bar represent  $10 \mu\text{m}$ .

Figure 5.11 shows confocal images of the relaxation of highly compressed deformable shells upon release of the stress. The shells were prepared in the same way as capillary 2 and the height of the sediment was around 5 mm. The pressure was released by rotating the capillary 90 degrees from its initial upright position. This released pressure on the packing of the shells in the sediment which started to drift and expand in the direction perpendicular to gravity. Figure 5.11A is a confocal image taken from a region close

to the bottom of the sediment. In the right hand side of the image shells are highly deformed and some are even hard to recognize individually. Image 5.11B is the same spot taken 40 min after acquisition of image 5.11 A. The number of highly deformed shells is clearly less in this image due to the expansion and small flow in the sediment. While the packing of the shells was expanding they also recovered their initial spherical shape, which is a clear indication that they can reversibly sustain large forces and that the interaction between the shells is purely repulsive. Figure 5.11C, D and E show the elastic recovery of an extremely deformed, almost completely emptied shell during stress release. In figure 5.11C this shell can be seen as a thick white hemispherical segment running through the contour of a spherical particle (in the center of the red circle), with an overlap depth  $\delta_{ij} \approx (R_i + R_j)$ . After 38 sec the overlap depth was reduced by 43% and subsequently by 78% from the initial depth as shown in figure 5.11D and E. Here the applied stress from its contact neighbor was released when the neighbor was pushed to an adjacent void space.

*Probability distribution of contact force magnitude -  $P(f)$*

Magnitudes of contact forces were calculated for all particle pairs with overlap depth  $\delta_{ij} > 0$ . The average contact force and the number of contacts obtained for each volume fraction are listed in Table 6.1. The error in force magnitude in our experiment depends on the error in the overlap depth, which in turn is limited by the resolution in finding the coordinates of the shells. The coordinates of the shells were obtained with sub pixel accuracy with error less than one pixel size ( $0.080 \mu\text{m}$  in  $X_c$  and  $Y_c$  and  $0.040 \mu\text{m}$  in  $Z_c$ ). This leads to an error of approximately  $\pm 0.026 \mu\text{N}$  in contact force magnitudes, which is close to the value of average force measured in the packing at lowest volume fraction.

Figure 6.6 shows the distribution of the contact force magnitude normalized by the average contact force for packings at different experimental volume fractions above the jamming threshold. The distribution has a broad peak around the mean and a tail that extends to large forces, about  $3.5\langle F \rangle$  ( $f = F/\langle F \rangle$ ). This reflects the heterogeneity in contact forces in these disordered packings. At larger forces, above the mean, the probability is found to decay exponentially for the lowest volume fractions and to crossover to a Gaussian for the highest volume fractions, similarly to the results reported for simulation and experiments on 2D and 3D soft granular systems [28,93,133,159,160]. The tail of the distributions can approximately be fitted with an exponential and Gaussian function for the lowest and highest volume fractions, shown in figure 6.6. Note that the distribution of the contact force for  $\varphi = 0.906$ , made of shells of  $d/R_t = 0.04$  also shows a similar shape.

The packings  $\varphi = 0.810$  and  $\varphi = 0.835$ , which do not fall in the trend of other packings in  $g(r)$  exhibited a similar discrepancy in force distribution as well ( $\varphi = 0.835$  is not shown).  $P(f)$  of these packings showed a slightly higher peak near the mean

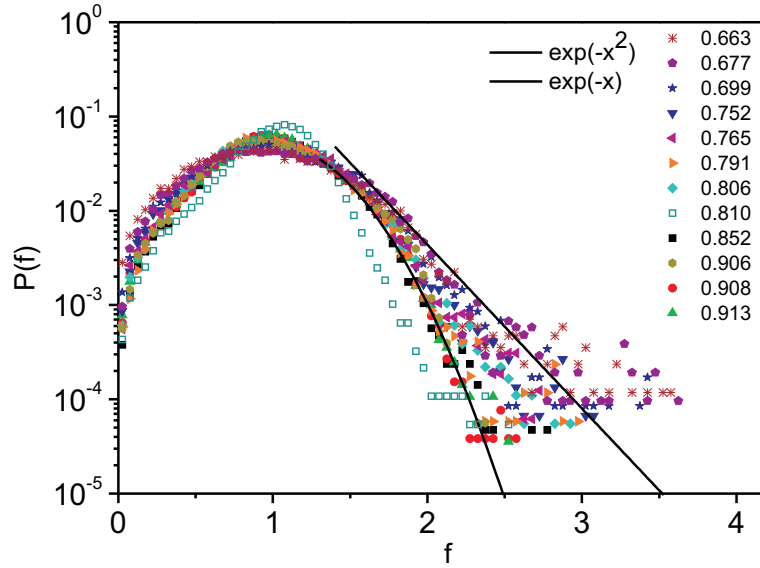


FIGURE 5.12. Probability distributions of contact forces normalized by the average contact force,  $P(f)$  ( $f = F/\langle F \rangle$ ) for a range of experimental volume fractions above the jamming point. Solid lines are exponential and Gaussian fits for the lowest and highest volume fractions. The open symbol represent the packing  $\varphi = 0.810$  that has a higher peak near the mean value and a steeper tail compared to other volume fractions.

force and a steeper tail compared to all other volume fractions (figure 6.6). In a 2D experimental study on the effect of particle order on the distribution of contact forces by Blair *et al.* [129], they observed a similar higher peak near the mean value, as well as a slightly steeper exponential decay at large forces for a crystalline packing. This result hints again the slight order in our packing of shells at  $\varphi = 0.810$  and  $\varphi = 0.835$ .

*Scaling of Pressure,  $P$*

From the contact forces measured between particle pairs we calculated the pressure at each packing density and thereby investigated how pressure scales with volume fraction for the packing of shells, above the jamming threshold. The global pressure is determined by  $P = \sum_i \sum_{j>i} F_{ij} l_{ij} / V$ , [134,162] where  $V$  is the total image volume,  $l_{ij}$  is the distance between the centers of the contact pairs. The calculated value of  $P$  varied from  $3.05 \text{ kPa}$  to  $19.68 \text{ kPa}$  for the experimental range of  $\varphi$ . The non-zero value of the pressure at the lowest value of  $\varphi$  resulted from the error in the measurement of overlap depth and radii of shells. Since the contact forces must be positive this leads to a finite pressure where it should be almost zero. Therefore, we subtracted from the measured pressures an amount  $P_c = 4.46 \text{ kPa}$ , which is the pressure close to  $\varphi_c$  obtained from the power law fit of  $Z$ .

Numerical simulations predicted a scaling for the pressure  $P = P_0(\varphi - \varphi_c)^{\alpha-1}$  [30] with the exponent the same as for the force law. Here  $\alpha$  is the exponent of the interaction

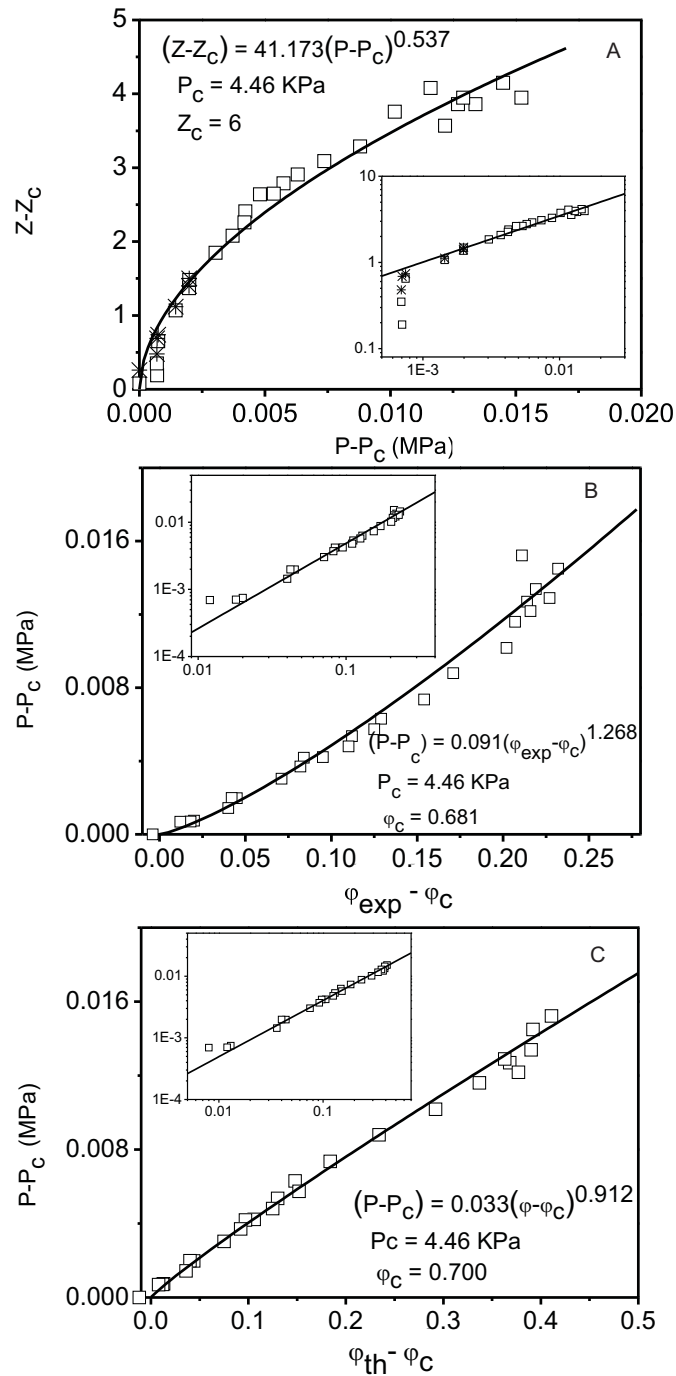


FIGURE 5.13. Scaling of (A) the excess contact numbers  $Z$  with pressure  $(P - P_c)$  and (B and C) the variation of pressure with volume fraction above jamming point for experimental and theoretical value of  $\varphi_c$ . The inset plots are shown on log-log scale. The data points marked in \* in (A) are the contact numbers avoiding the rattlers.

potential, which is 2 for harmonic interaction and 2.5 for a Hertzian. For our system of shells we expect  $\alpha = 1.5$ , as the force is proportional to the square root of the deformation, and hence a square root scaling of pressure with density. Furthermore, a comparison of predicted square root scaling of both excess contact number and pressure with volume fraction has to give  $(Z - Z_c) \propto (P - P_c)$ . However, we found a non-linear variation, shown in figure 5.13A. The data is fitted with a power law with an exponent  $0.537 \pm 0.031$  and prefactor  $41.173 \pm 6.107$ . Besides, the scaling of the excess pressure with excess volume fraction (experimental volume fraction) was found to deviate from a square root law, figure 5.13B. Nevertheless, the data obeys the power law  $(P - P_c) = 0.091(\varphi - \varphi_c)^{1.268}$ , where the prefactor and the scaling exponent were fixed and obtained by combining the scaling laws  $Z - Z_c = 11.395(\varphi - 0.683)^{0.681}$  and  $Z - Z_c = 41.173(P - 4.45)^{0.537}$ . Similarly for the theoretical volume fraction we obtained  $(P - P_c) = 0.033(\varphi_{th} - \varphi_c)^{0.912}$ , figure 5.13C. Similar deviations from the predicted power law were also observed for emulsion droplets, both in 2D and 3D [134,163]. However, in 2D photoelastic disks the reported value of  $(\alpha - 1) = 1.1$  was in good agreement with simulation results, but the range in the density was rather narrow, only 1% [132].

#### *Force network*

We analyzed the spatial orientation of contacts in the compressed shells for different volume fractions to check for an anisotropy in stress distribution, as the shells were subjected to unidirectional compression. We determined the angle of the contacts carrying forces above the mean with respect to the direction in which gravity acted. The probability distribution of these angles ( $\theta$ ) normalized by the unit solid angle for different volume fractions is shown in figure 5.14. For higher volume fractions the probability of the angles is found to be more biased in the direction of gravity (along the length of capillary, see figure 5.1), figure 5.14A. This is of course the direction in which the shells were compressed. In contrast, for most of the lower volume fractions the distribution is much more isotropic and even slightly higher in the direction perpendicular to gravity, especially for the lowest  $\varphi$ 's. These are the packings acquired at a position away from the bottom of the sediment and close to the top of the sediment in capillary 1 where the weight from the shells from top is much smaller. The shells in this region were mainly confined by the capillary wall along the  $Y$  and  $Z$  directions (see figure 5.1).

The spatial distribution of the contact forces in our compressed shells can be visualized by representing the forces by tubes connecting the centers of the contact pairs. Figures 5.15A and B shows the force network in an image volume at volume fractions  $\varphi = 0.699$  and  $\varphi = 0.908$ . Only larger forces above 1.5 times the average force are shown in the figure. The thickness of the tube and its color are proportional to the force magnitude. In both the packings, in addition to many isolated segments there are force chains that branch and merge. The presence of force chains, *i.e.* contacts carrying large force, were seen before in experiments on 2D frictional photoelastic disks under

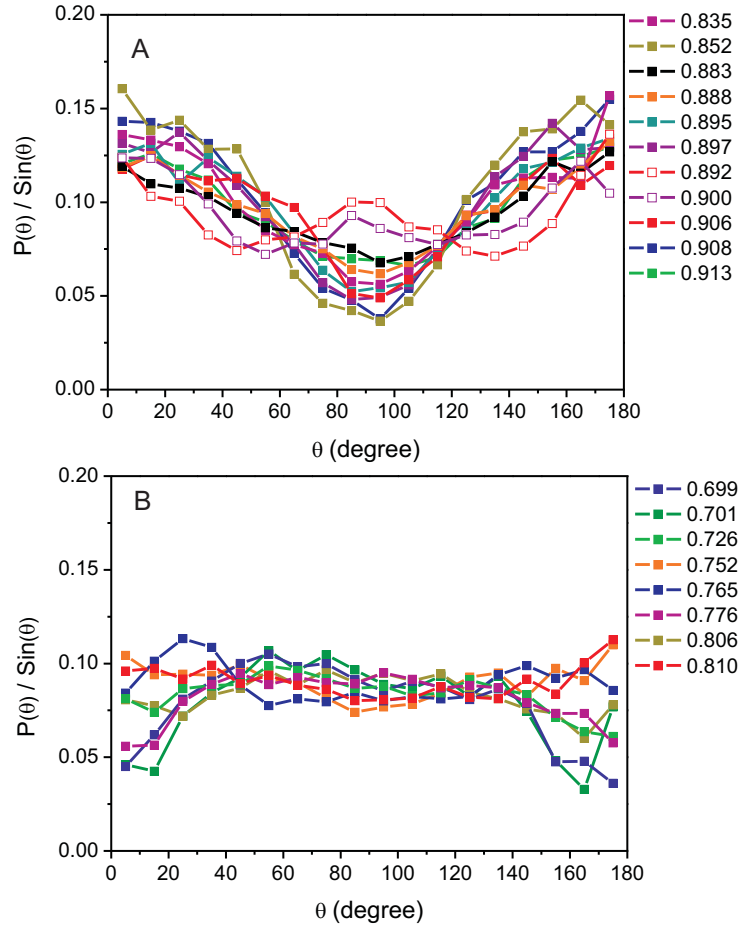


FIGURE 5.14. Probability distribution of angles with respect to gravity (X-axis) for contacts carrying above average force, for (A) high  $\varphi$  and (B) low  $\varphi$ .

shear [32], bidisperse emulsion droplets in quasi-2D experiment [134] and in polydisperse 3D piles of frictionless liquid droplets under uniaxial compression [133]. But they were not seen in the 3D emulsion system studied by Brujic *et al.*, where the droplets were compressed by centrifugation [27, 93]. In their admittedly small sample volume, the forces appeared to be uniformly distributed in space and the average stress was found to be independent of direction, indicating isotropy.

To further investigate the structure of force chains, mainly the tendency to form linear chains, we used a definition for the force chain that avoid the branching and merging of force network, described in the article by Desmond *et al.* on a 2D bidisperse system of emulsion droplets [134]. From their definition a force segment belongs to a force chain if it is one of the two largest forces on both particles joined by the force segment. By this way the maximum number of forces on a particle is limited to two, thereby avoiding branching of the chains. In addition to this we set the limit of minimum length of a

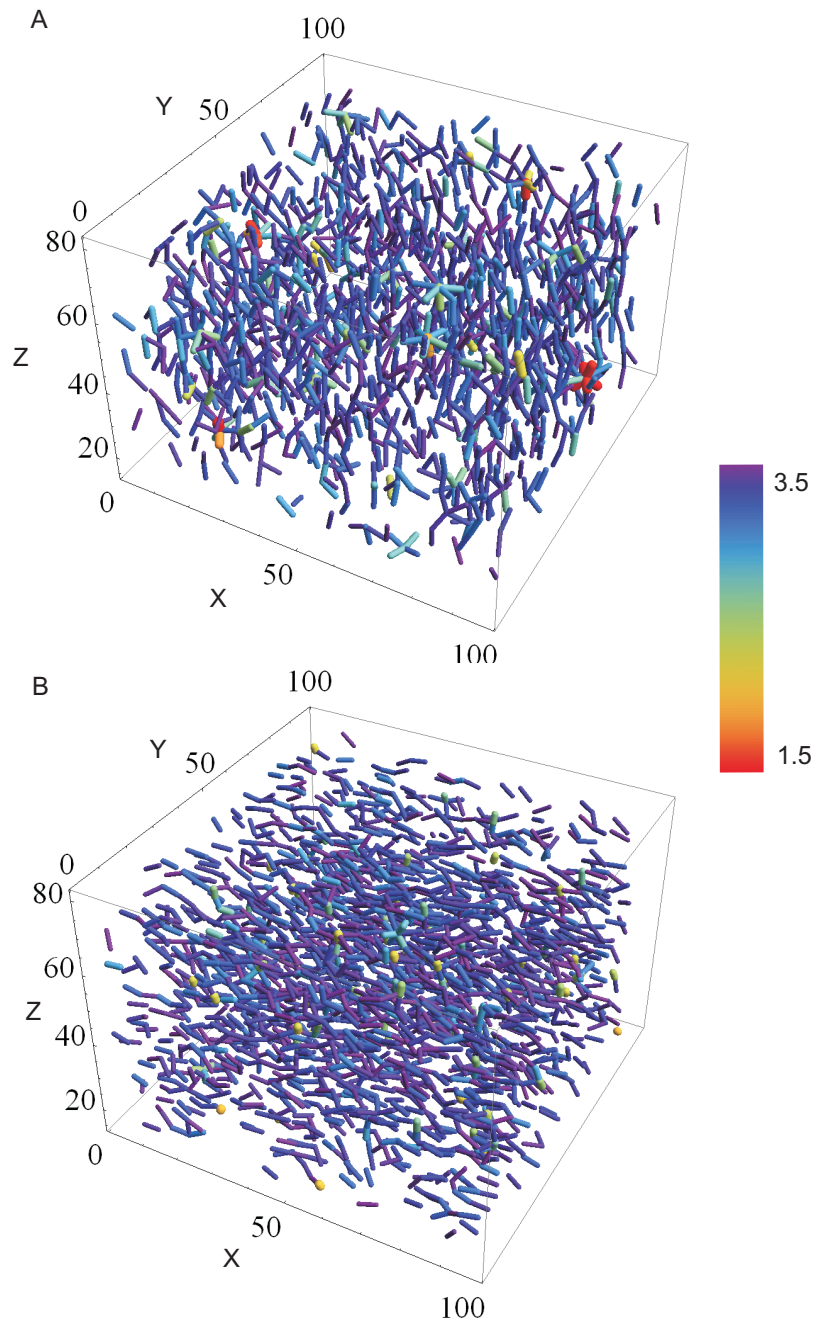


FIGURE 5.15. Force network in compressed shells in a lowest and highest packing fractions, (A)  $\varphi = 0.699$  and (B)  $\varphi = 0.908$  for forces greater than 1.5 times average value. Forces, in units of the average force  $\langle F \rangle$  are represented by tubes connecting the centers of contact pairs where the thickness and color of the tube is proportional to the magnitude of the normal force. Red indicates a force 3.5 times larger than the average force. The  $X$ -axis is the direction of gravity.

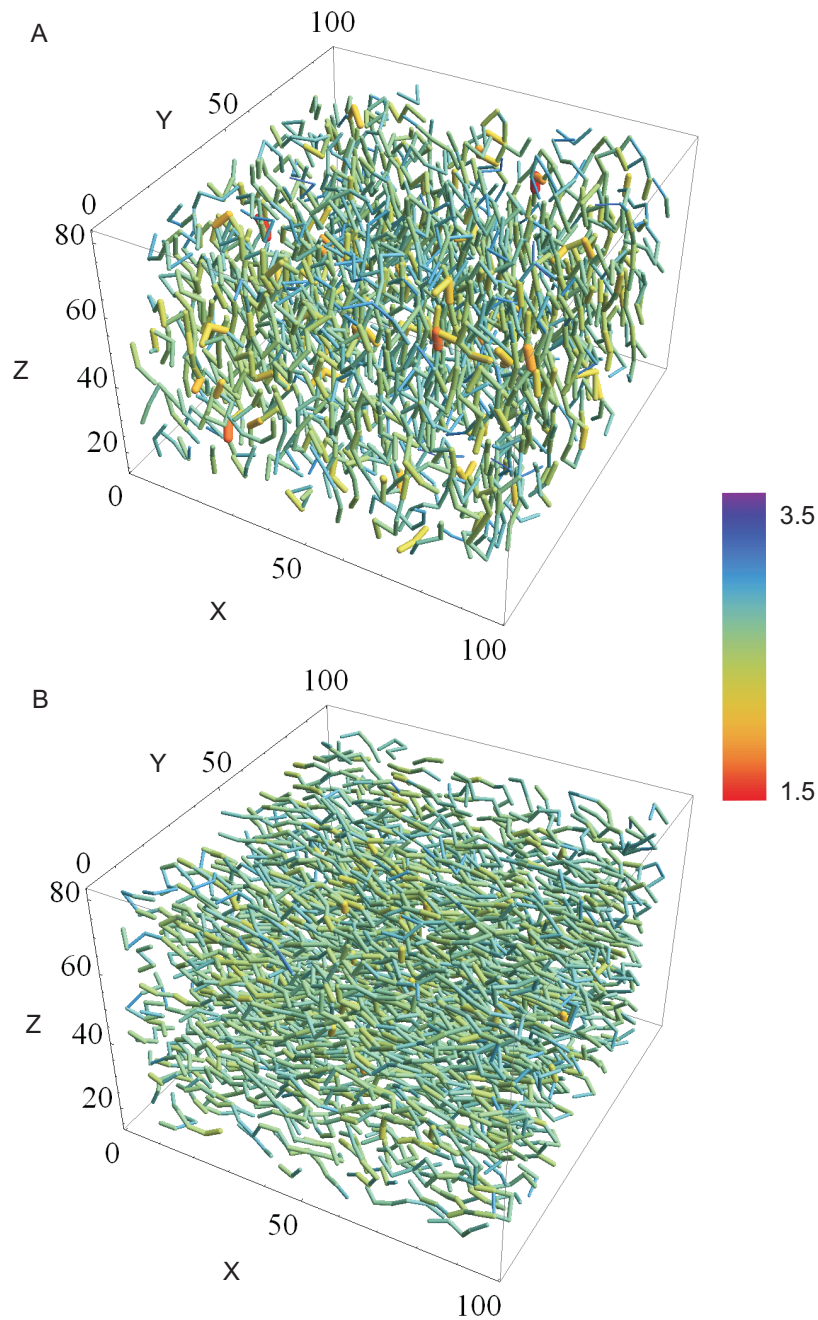


FIGURE 5.16. Force network in compressed shells for the lowest and highest packing fractions (A)  $\varphi = 0.699$  and (B)  $\varphi = 0.908$  based on the definition of one of the two largest forces on both particles. Forces, in units of the average force  $\langle F \rangle$ , are represented by tubes connecting the centers of contact pairs where the thickness and color of the tube is proportional to the magnitude of the normal force. Red indicates a force 3.5 times larger than the average force. The  $X$ -axis is the direction of gravity.

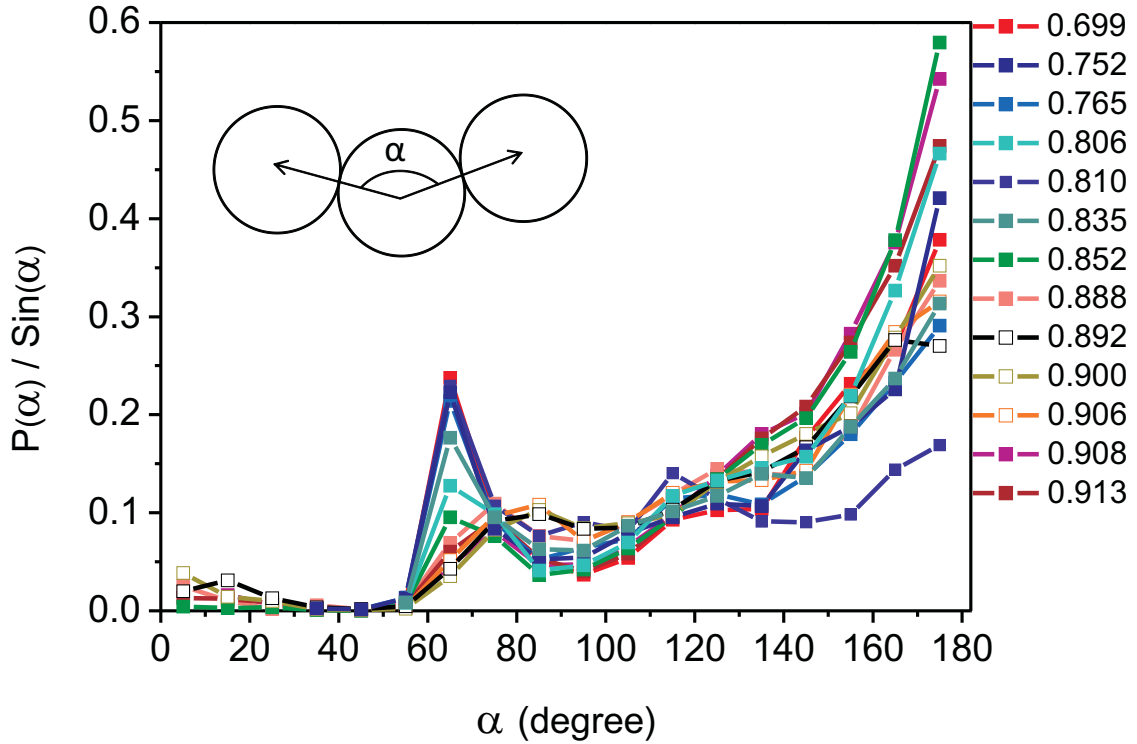


FIGURE 5.17. Probability distribution of the angle between the force segments in force chains normalized by the solid angle for different volume fraction of compressed shells.

force chain to three particles or two force segments. Note that in this definition even small forces below average can also become a part of force chain, provided it is the largest for the given particle and its contacting neighbor. Figure 5.16A and B shows the force chains based on the above definition in our compressed shells for the volume fractions  $\varphi = 0.699$  and  $0.908$ . At  $\varphi = 0.699$  the chains are highly tortuous with an average length of  $4.45\langle 2R_t \rangle$ . However, at  $\varphi = 0.908$  there are a few chains that appears to be linear and aligned along the gravity axis ( $X$ -axis). The average length of the chains in this packing is  $5.23\langle 2R_t \rangle$ . The force chains are found to be rather short in all sample volumes at different  $\varphi$  (Table 6.2).

To quantify the linearity of the force chains, we plotted the probability of the angle ( $\alpha$ ) between the force segments in a force chain normalized by the unit solid angle, as shown in figure 6.9. The probability  $P(\alpha)/\sin(\alpha)$  is non-uniform: it has a small peak at  $\alpha$  around  $60^\circ$  and a high peak near  $180^\circ$ . For all volume fractions the probability is strongly suppressed for  $\alpha < 60^\circ$  due to the narrow size distribution of the shells. The peak around  $60^\circ$  indicates an enhanced tendency for large forces to form trimers in the system; a similar peak was also observed in experiments on monodisperse compressed emulsions [133]. However, the peak height is rapidly reduced with increasing deformation of the particles, *i.e.* with increasing  $\varphi$ . In addition to this the center of

Image stack	$\varphi$	average chain length $\times \langle 2R_t \rangle$	Persistence length ( $\ell^*$ ) $\times \langle 2R_t \rangle$
S23	0.699	4.45	2.31
S18	0.752	4.35	2.26
S15	0.765	5.25	2.08
S11	0.806	5.68	2.85
S12*	0.810	5.33	1.61
S10*	0.835	4.30	2.22
S9*	0.852	5.89	3.43
S1*	0.885	4.86	2.27
S7	0.888	4.65	2.32
S3*	0.900	6.10	2.43
T1	0.906	4.96	2.62
S5*	0.908	5.23	3.49
S2*	0.913	6.21	3.11

TABLE 5.3. The value of average length and persistence length of force chains for different  $\varphi$ .

the peak is seen slightly shifted to higher angles with increasing  $\varphi$ , for example at  $\varphi = 0.892, 0.900, 0.906$  (marked in open symbols)  $\alpha$  is close to  $90^\circ$ , where all other volume fractions show a dip in the distribution. This could perhaps happen when the neighbors of a particle started overlapping each other. For the packing,  $\varphi = 0.810$ , which showed a deviation in  $g(r)$  from other volume fractions, we find more or less three prominent peaks: around  $60^\circ, 120^\circ$  and near  $180^\circ$ , which again is a sign that there is a local ordering in the sample. However, sample  $\varphi = 0.835$  whose first peak in  $g(r)$  was similar to  $\varphi = 0.810$ , only has two peaks - at  $60^\circ$  and  $180^\circ$  with a slightly higher probability at  $60^\circ$  compared to its nearest lower volume fractions. Note that, except for  $\varphi = 0.810$  the rest of the volume fractions had a higher probability close to  $180^\circ$ , which strongly indicates a preference for a linear alignment of force segments in force chains. The peak height is maximum for the highest volume fractions.

From the distribution  $P(\alpha)/\sin(\alpha)$  we measured the persistence length of the chains for a range of volume fractions. Similar to polymers, the persistence length of a force chain is a measure of the average length beyond which the chain has forgotten its original direction. Numerically its value is obtained from the relation [178],

$$\ell^* = \langle 2R_t \rangle / (1 - \langle \cos(180 - \alpha) \rangle) \quad (5.10)$$

where  $\langle 2R_t \rangle$  is the mean diameter of the particle. Table 6.2 shows the average length and persistence length of force chains for the volume fractions plotted in figure 6.9. The value of the persistence length is smaller than the average length of the chain, with the lowest value for the packing  $\varphi = 0.810$ , and also compared to the system size. We therefore do not find a long-range chain like correlation in our system of compressed shells in 3D. In 2D and 3D systems of frictionless emulsion droplets the persistence length of the chains were  $2\langle 2R_t \rangle$  [134] and  $10\langle 2R_t \rangle$  [178], respectively. Our value of the persistence length is more closer to the bidisperse 2D emulsion system by Desmond *et al.* [134] and shows a little evidence for linear force chains.

## 5.4 CONCLUSIONS

We studied the structure and contact force distribution in mostly random packings of monodisperse, fluorescently labeled and index-matched shells under static compression in 3D for a range of experimental volume fractions, above the jamming threshold. The high deformability of the shells enabled us to go far beyond the jamming threshold. Contrary to other jammed systems studied so far these shells do not conserve their volume upon deformation. The radial distribution function,  $g(r)$  for all packings was found to resemble the structure of a liquid where the deformation of the particles broadened and shifted the first peak of  $g(r)$  to radial distances less than the diameter, in contrast to amorphous packings of hard particles. The analysis of the local bond order parameter showed that the shells at all volume fractions were mostly disordered, even the two packings that did not fall in the trend exhibited by other volume fraction samples in  $g(r)$ .

From the analysis of the scaling of the average contact number  $Z$  with volume fraction we obtained a higher value of the power law exponent for the experimental volume fractions and almost the same value  $\beta = 0.50$ , as predicted in numerical simulation for theoretical volume fractions. In addition to the scaling of the contact number we also investigated the scaling of the average number of dimples *i.e.* the buckling number,  $N_\delta$ . As expected the coefficients of the power law scaling with volume fractions were just half the coefficients in the scaling of  $\langle Z \rangle$ . This is due to the fact that at each contact only one of the shells is dimpled and the other remained spherical. Further analysis on the randomness of this process of dimpling one way or the other revealed that the process is volume fraction dependent. At higher volume fractions dimpling became non-random, that means particles with a small number of contacts tend to receive more than their share of dimples; on the other hand particles having a large number of contacts tend to make a dimple on their neighbors.

By measuring the depth of the deformations at contact regions we determined the magnitude of normal force between pairs of particles, which is proportional to the square root of the deformation. The shape of the distribution of the contact forces

normalized by the average force was almost similar for all volume fractions, except that the probability for large forces (above average) decayed faster than exponential at higher compressions. Although the force in our system of compressed shells obeys a square root law, we obtained a higher exponent for the scaling of the global pressure with excess packing density. Moreover, in our 3D compressed shells we found only the presence of short force chains with a length on the order of  $4\langle 2R_t \rangle - 5\langle 2R_t \rangle$ , though the forces were slightly anisotropic in the system due to the unidirectional compression in the preparation of the sample.

## 5.5 ACKNOWLEDGMENTS

We thank Bas Kwaadgras for his help in the algorithm for the quantitative analysis of the force chains, Thijs Besseling and Ernest van der Wee for performing the local bond order calculations. Johan Stiefelhagen is thanked for fixing problems with Mathematica programs.



# 6

## 3D microstructure and contact forces in jammed packings of elastic shells - shear

We describe here our preliminary results on effects of shear on 3D structure of force networks in a jammed packing of our elastic shells. The packing of shells was subjected to a small shear strain, up to 0.216, at an extremely low shear rate, using a parallel-plate shear cell that was coupled to a confocal microscope. We observed a shear induced anisotropy in both pair correlation function and contact force network, however no appreciable change was seen in the number of contacts per particle.

## 6.1 INTRODUCTION

Unlike fluids, jammed materials like emulsions, granular matter, foams and glasses are rigid and possess a yield stress. The yielding of a jammed solid is different from its crystalline counterpart, due to the lack of order in a dense packing of particles. Yielding is associated with local plastic or irreversible rearrangements of particles. One of the key features that greatly changes with an applied stress is the force network. The force network is found to become anisotropic under shear deformation [18, 26, 32, 179–182].

Here we discuss preliminary results on the behavior of a jammed suspension of fluorescently labeled and index matched deformable shells of size  $4.32 \mu\text{m}$  under steady shear in 3D. Our results are preliminary, because although it is demonstrated that a significant shear can be applied on this system, the conditions to prevent slip at the walls were not yet optimized. The shells were sheared in a home-built parallel plate shear cell mounted on top of an inverted confocal microscope. This parallel plate shear setup was specifically designed to be used with a confocal microscope as it has the ability to independently move both the upper and lower plate. In this way the relative velocities between the plates, and thus the shear-rate, can be kept constant, while the plane which has a zero-velocity with respect to the microscope can be moved up and down. By having the focal plane of the confocal microscope coincide with that of the zero-velocity plane, quantitative real space imaging becomes possible even in concentrated particle systems during shear [183]. In the present study however, the shear rates used were so small that we did not need to use both plates and shear was applied simply by only moving the upper plate.

The volume fraction of the sample studied was higher than the jamming point for frictionless spheres ( $\varphi > 0.64$ ) such that the shells were already deformed in the sample. We investigated the effect of a simple shear which involved compression, extension and a solid rotation of the shells on the structure of jammed shells. This was performed by looking at the projection of the radial distribution function  $g(r)$  in the shear velocity-gradient plane and the changes in the number of contacts per particle for different values of strain ( $\gamma < 1$ , see Figure 6.2). Furthermore, we analyzed the changes in the probability distribution of the contact forces and the anisotropy in the force network in the packing that resulted from the applied shear deformation.

## 6.2 EXPERIMENTAL METHOD

### 6.2.1 Sample preparation

A parallel plate shear cell mounted on top of an inverted confocal scanning laser microscope (Leica TCS-SP2) was used to study the real-space behavior of jammed deformable shells under shear. Details of the design and layout of the shear cell are

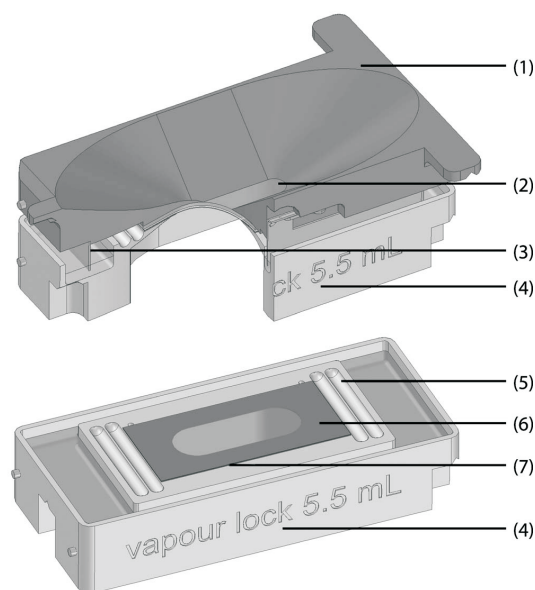


FIGURE 6.1. The top and bottom cassettes of the shear cell [183]. The lower picture is the bottom cassette, and the upper picture shows the pair of cassettes (with a part cut out) placed on top of each other. (1) Top cassette, (2) microscope slide glued to top cassette that allows for light scattering, (3) metal vapor lock that seals the sample, (4) bottom cassette, (5) gully that can be filled with solvent to control vapor pressure, (6) microscope glass slide and (7) paper glue mask.

described in [183]. The sample was placed between two parallel microscope glass slides that were attached to a bottom and top cassette respectively as shown in Figure 6.1.

On the bottom cassette a glass coverslip (Menzel Gläser, no.1.5, thickness 0.15-0.17 mm) of 24 x 50 mm and on the top cassette a microscopy glass slide (Menzel Gläser, thickness 1-1.5 mm) cut to 9 x 29 mm were attached following the method described in reference [183]. In order to apply a shear strain to the sample, these cassettes were placed in translational stages that were displaced by piezostepper motors. Before loading the sample the glass plates were aligned parallel to each other with adjustment screws. This is important in order to create a uniform and parallel shear flow. The alignment was determined with confocal microscopy in reflection mode using an Argon 488 nm laser and an air objective (20x 0.7 NA, Leica). After alignment the objective was changed for an oil immersion objective (63x 1.4 NA, Leica) that was used for imaging, and the gap width was set ( $h \approx 46 \mu\text{m}$ ). The vapor barrier of the bottom cassette was filled with water and a few droplets of solvent were dropped into the vapor gully to minimize evaporation of the sample. After that, a drop of sample was placed on the glass slide of the bottom cassette. Finally, the top cassette (with the metal vapor lock attached to it) was lowered on top of the sample.

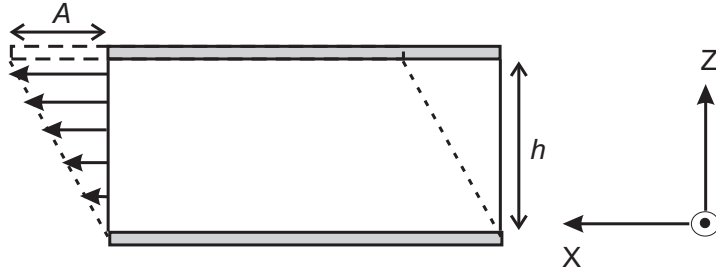


FIGURE 6.2. Schematic of the shear cell. The sample between the glass plates is strained by moving the top plate a distance  $A$  in the direction of the  $X$  axis that together with the  $Y$  axis forms planes parallel with the imaging planes of the microscope. The movement of the plate creates a velocity field along the  $X$  axis of the microscope and a gradient along the  $Z$  axis. The curl of the field, the vorticity, is oriented along the  $Y$  axis

Figure 6.2 shows a schematic representation of the shear cell. The top plate (gray) was moved from its initial position by a distance  $A$  with a velocity  $v_t$  that can be set during the experiment. The bottom plate was kept stationary. The movement of the plate creates a velocity field along the  $X$  axis of the microscope and a gradient along the  $Z$  axis. The curl of the field, the vorticity, is oriented along the  $Y$  axis.

In our experiment a shear force was applied to the system by moving the top plate to an amplitude of  $A = 20 \mu\text{m}$  in steps of  $5 \mu\text{m}$  with a slow, constant speed  $v_t = 10 \text{ nm/sec}$ , to limit the chances of wall slip. This corresponds to a shear rate of  $\dot{\gamma} \equiv v_t/h = 0.217 \times 10^{-3} \text{ s}^{-1}$  and a total shear strain  $\gamma \equiv A/h = 0.434$  in steps of 0.11. The sample consisted of shells of radius  $R_t = 2.16 \pm 0.03 \mu\text{m}$  (measured from static light scattering (*SLS*)) with polydispersity 3% and a shell thickness  $d = 30 \text{ nm}$  ( $d/R_t = 0.013$ ), measured by atomic force microscopy *AFM* (shells prepared using Turrax homogenizer method, see chapter 2).

### 6.2.2 Data acquisition and image analysis

The 543 nm laser line of a He-Ne laser was used for imaging. Scanning along the  $Z$ -axis was done using a piezo focusing drive (Physik Instrumente). The sample was left to equilibrate for 15-20 mins. Before shearing the sample a  $XYZ$  stack was acquired for a reference. Then the top plate was moved  $20 \mu\text{m}$  with a speed  $10 \text{ nm/s}$  in successive steps. After each step a  $XYZ$  stack of the sample volume was taken. An image stack comprised of  $1024 \times 1024 \times 352$  voxels with a voxel size of  $0.1037 \times 0.1037 \times 0.0945 \mu\text{m}^3$ , giving a total field of view  $106.25 \times 106.25 \times 33.26 \mu\text{m}^3$ . The voxel size in  $Z$  was corrected for index mismatch with a scaling factor 0.91 [152, 153]. The acquisition time for each image stack was approximately 25 mins. The 2D confocal images of the sample in a  $XZ$  plane before and after shear where the top plate had travelled  $5 \mu\text{m}$  from the initial position are shown in Figure 6.3A and B. The shells are clearly jammed and

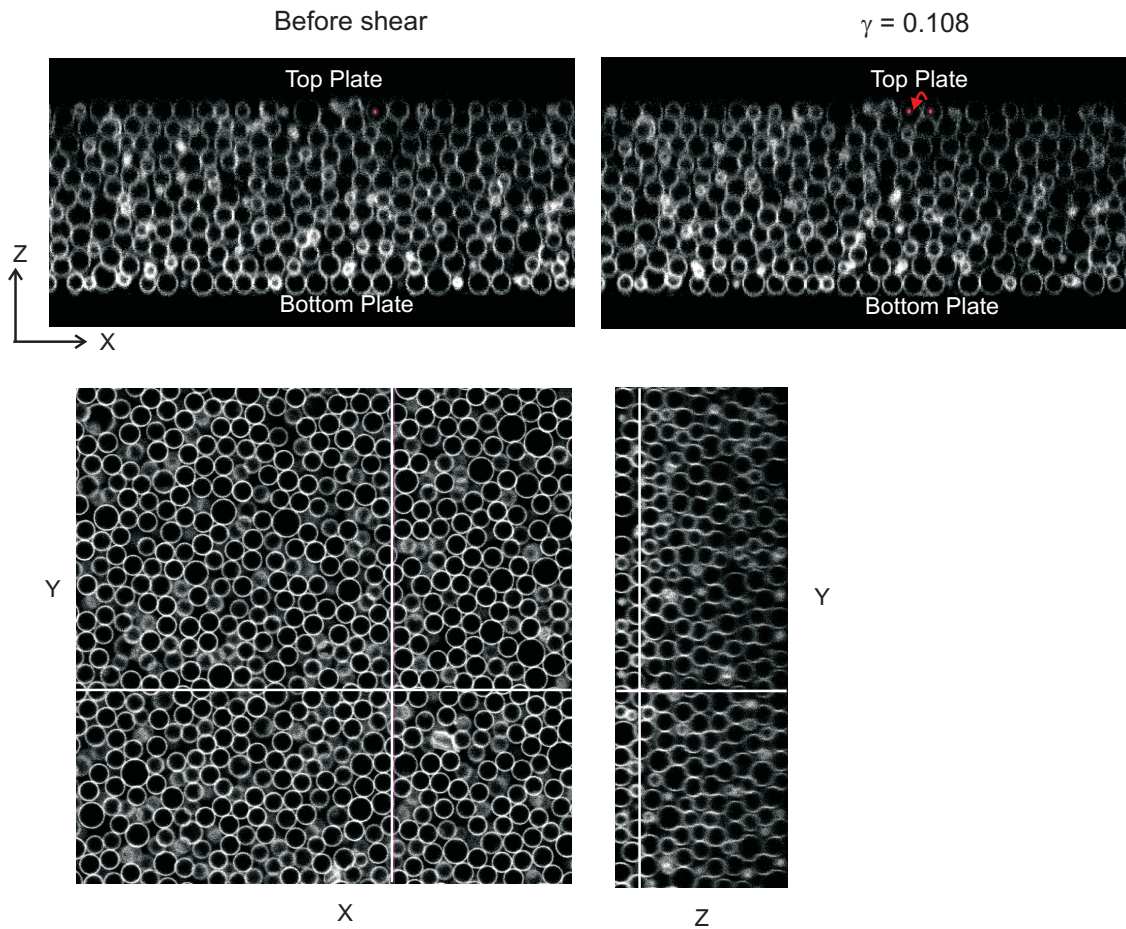


FIGURE 6.3. 2D confocal images of a concentrated suspension of shells both before (A) and after (B) the sample had been strained by moving the top plate a distance of  $5 \mu\text{m}$  in the negative  $X$ -direction (velocity axis) of the image. The red dot marked at the center of a shell in the image before shear shows its initial position which is shifted by an amount  $\approx 4.29 \mu\text{m}$  to the right, shown by the arrow, after shearing the sample. Image size is  $512 \times 262$  pixels. Confocal images of shells in a  $XY$  (C) and  $YZ$  plane (D). Image size is  $1024 \times 1024$  pixels and 352 slices in  $Z$ .

deformed between the parallel plates and the shells near the top plate were displaced by almost the same amount as the distance travelled by the plate.

The coordinates of the particles were obtained through the image analysis procedure described in chapter 4. Table 6.1 gives an overview of the sample before shear and at different values of the shear strains. We measured the actual strain in the sample by measuring the change in position of the shells near the top plate from their initial position after each step of shear, as shown in Figure 6.3. By looking at the displacement of shells at other positions we found that the shear was uniform throughout the gap. The measured strain was found to stay behind the applied strain, especially for the

Image stack	Applied strain	Measured strain	No. of particles	image volume	No. of contacts ( $\mu\text{m}^3$ )	$\phi$	$\langle F \rangle$ ( $\mu\text{N}$ )	$\sigma_F / \langle F \rangle$ (%)
Before shear	0	0	5321	290444	21504	0.835	0.0147	29.25
Shear1	0.108	0.093	4697	264465	19237	0.784	0.0158	32.27
Shear2	0.217	0.169	4613	264470	18733	0.758	0.0161	34.78
Shear3	0.326	0.204	4592	264675	18502	0.755	0.0160	35.00
Shear4	0.434	0.216	4775	264631	19416	0.778	0.0155	36.12

TABLE 6.1. The details of image stacks obtained from image analysis algorithms from the sample before undergoing shear and after the sample had been strained by a total strain 0.434 in four steps.

largest strain. For shear 4 the measured strain was just half the total applied strain and thereafter the shells hardly followed the plate movement due to complete slip at the moving upper plate. Note that we tried a few methods to avoid wall slip, for example by introducing roughness on to the plate on the order of 80 nm by abrasion and 5  $\mu\text{m}$  by adsorbing polymethylmethacrylate particles to the plate. Both methods failed to prevent the wall slip, on the contrary, the rough plates were found to enhance slipping of the shells near the plate. Normal glass plates without any kind of treatment were found to work better for the shear experiment. Moreover, we also noticed that repeated use of the same glass plates for shearing of the shells also enhanced wall slip. Most likely this is caused by the adsorption of polyvinylpyrrolidone (*PVP*) that stabilizes the shells to the glass plate, modifying the plate surface and thereby preventing the shells from sticking to the plate. This hypothesis needs to be investigated further. For the experiments reported in this chapter, where the slow small strain was applied sequentially, the plates were not new and they were used beforehand a couple of times and this might have led to the slipping near the shearing surface.

The number of particles listed in the table was obtained from an image volume after avoiding almost a layer of particles close to both the glass plates. From the  $Z$ -coordinates obtained from the analysis we found a 9% reduction in the height  $h$  for the sample just after the first shear step which then later remained unchanged. This reduction in the gap width between the plates resulted probably from the relaxation of the bottom plate, which was slightly deformed by the weight of the top cassette when it was put on, and was transferred through the suspension of the jammed shells.

The volume fractions of these packings were calculated by summing the volumes of the spheres and subtracting their overlap volume in an image volume, and are listed in Table 6.1. The image volumes correspond to the product of the length in  $X$  and

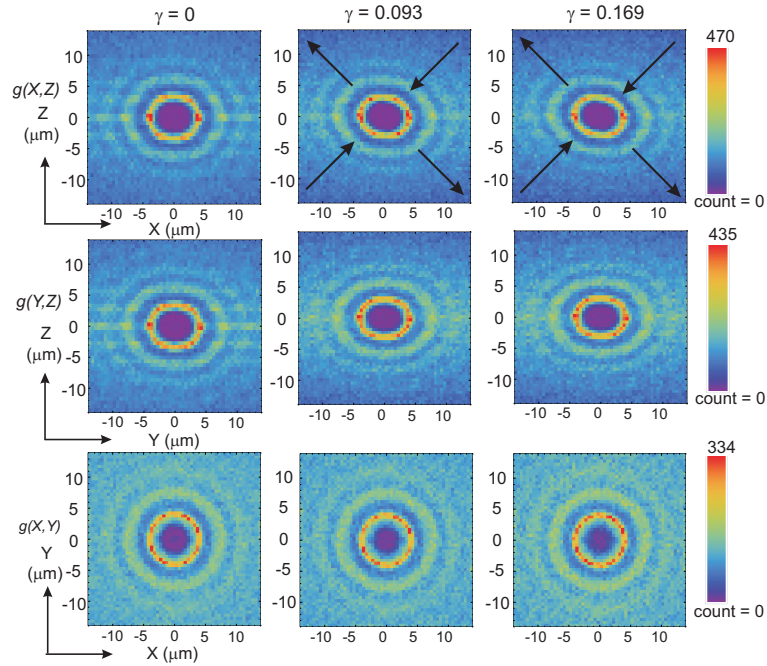


FIGURE 6.4. Probability of inter particle distances in different planes  $XZ$  (velocity-gradient),  $YZ$  (vorticity-gradient) and  $XY$  (velocity-vorticity) for the shells before subjecting to shear and after the sample was sheared by an amount  $\gamma = 0.093$  and  $\gamma = 0.169$ . Bin size in  $X$ ,  $Y$  and  $Z$  are  $0.498 \mu\text{m}$ ,  $0.498 \mu\text{m}$  and  $0.504 \mu\text{m}$  respectively. Shear induced extension and compression are illustrated by the arrows.

$Y$  directions that are reduced by an amount  $R_t$  (average radius obtained from image analysis) from both sides to compensate for the particles that are missing near the edge (not identified during image analysis) and in the  $Z$  direction after avoiding almost a layer of particles close to both the glass plates. The difference in the image volume and in the number of particles mostly resulted from the reduction of gap width due to the relaxation of the bottom plate combined with slight discrepancies in the cut-off values chosen along the gap width to remove particles close to the wall. The average radius of the particles measured from the image analysis algorithm was  $R_t = 2.20 \mu\text{m}$  with average polydispersity 5%. This size is very close to the size obtained from light scattering.

## 6.3 RESULTS AND DISCUSSIONS

### 6.3.1 Structure of deformable shells under shear

#### *Radial distribution function $g(r)$*

The shear induced microstructure of our suspension of deformable shells was analyzed by calculating the radial distribution function  $g(r)$ , which is the probability of finding

a particle at a distance from a given reference particle [1]. Because of the anisotropy introduced by the shear to illustrate the 3D  $g(r)$  in different planes, we made 2D cuts of a finite thickness along different planes. For example,  $g(X, Z)$  is calculated by considering all pair separations in which the magnitude of the  $Y$  component of the separation satisfies  $|Y| < R_t$ .

Figure 6.4 shows  $g(X, Z)$ ,  $g(Y, Z)$  and  $g(X, Y)$  for the sample before and after applying shear, for two measured consecutive strains  $\gamma = 0.093$  (shear 1) and  $\gamma = 0.169$  (shear 2). The three bright rings with decaying probability (indicated by color) in the plots represent the first, second and third shell of neighbor particles. The configuration of the sample before shear,  $\gamma = 0$ , already shows a slight anisotropy, visible as 6-fold maxima in the first-order ring, especially in the  $X$ -(velocity) direction. This is probably due to the particle layering possibly induced by the flow when the top cassette was lowered on top of the sample. The amount of order that this flow may have introduced appears modest as can be observed from the images in Figure 6.3. Moreover, this flow caused a uniaxial compression of the structure of the shells, which is the cause of the observed flattening of the bright rings along the  $Z$  axis. When the sample was then sheared the configuration became more asymmetric around the center where the bright rings got closer to the center as the shells were squeezed along the compression axis and the rings moved away from the center as the shells were stretched out along the extension axis.

In the velocity-vorticity ( $XY$ ) plane the configuration was symmetric and remained unaffected by shear. For  $\gamma = 0.204$  and  $\gamma = 0.216$  the structure only changed slightly from that shown in Figure 6.4. Since in these cases significant wall slip took place and the microstructure was not distorted much further.

#### *Contact number ( $Z$ )*

The distribution of the contact numbers per particle for the shells subjected to shear strain is shown in Figure 6.5. Only particles that were more than one particle diameter away from the edge of the image volume were considered for the contact number distribution. This was to avoid under-estimating of the average contact number, as there will be many contacts missing for the particles identified at the edges.

There is no significant change in the shape of the distribution with increasing strain, except for a slight increase of probability at lower contact numbers. Therefore, the average contact number  $\langle Z \rangle$  remained nearly the same for the low strains applied in these experiments. However,  $\langle Z \rangle$  was slightly higher for shear deformation  $\gamma = 0.093$  compared to the sample before shear,  $\gamma = 0$  (inset plot). The reason is perhaps the compression of the shells along the  $Z$  axis of the microscope during the relaxation of the bottom cassette creating slightly more contacts along  $Z$ . From the small amount the sample was strained in the experiment it is likely that shells are not significantly making or losing contacts during shear. Particles also hardly underwent rearrangements

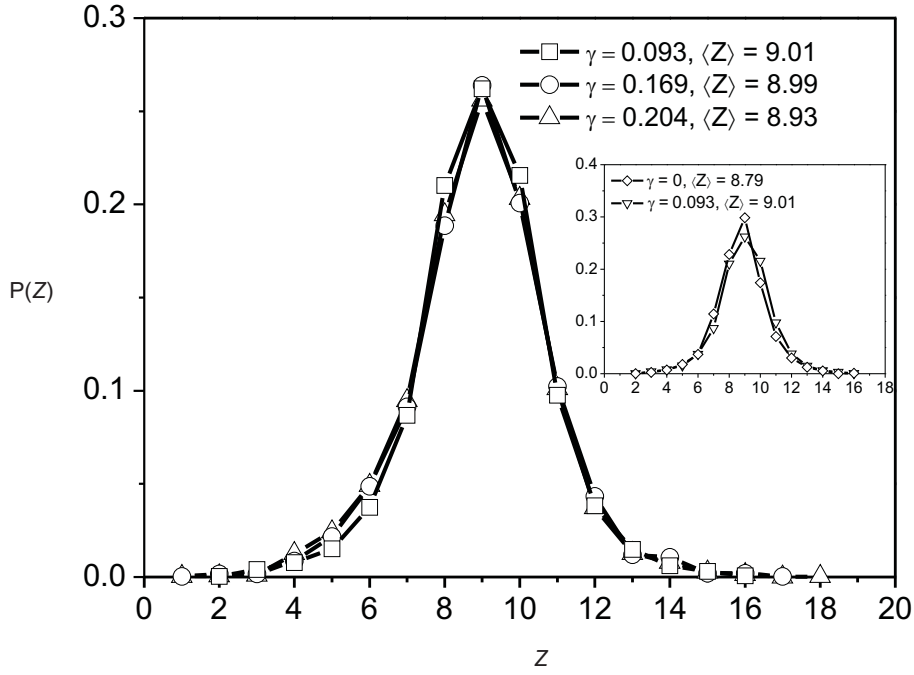


FIGURE 6.5. Probability distribution of the number of contacts per particle,  $Z$  for the sample at different values of strain. Inset plot is the distribution before applying shear on the sample,  $\gamma = 0$  and after the sample is strained by  $\gamma = 0.093$ .

for the low applied shear deformation. This was also confirmed in the confocal movies taken during shear.

### 6.3.2 Contact forces under shear

*Probability distribution of the contact force magnitudes -  $P(f)$*

The magnitudes of contact forces were calculated for all particle pairs with overlap depth  $\delta_{ij} > 0$  using the non-linear force law [117,118] (see chapter 5 for more details),

$$F_{ij} = \frac{0.534\pi E d^{5/2}}{1 - \nu^2} \frac{\sqrt{\delta_{ij}}}{\sqrt{R}} \sqrt{\frac{\delta_{ij}}{R_{ij}}} \quad (6.1)$$

Where  $E = 200$  MPa is the Young's modulus of the shell,  $R$  is the average radius of the particle from *SLS*,  $d$  is the thickness of the shell and  $\nu = 0.3$  is the Poisson ratio [116].

The average contact forces and the respective relative standard deviation obtained from the sample subjected to shear are included in Table 6.1. We measured a 7% increase in the magnitude of the average force when the sample was deformed by an amount  $\gamma = 0.093$  and for further strains the average force remained constant. The increase in force during shear step 1, perhaps resulted from the compression of the

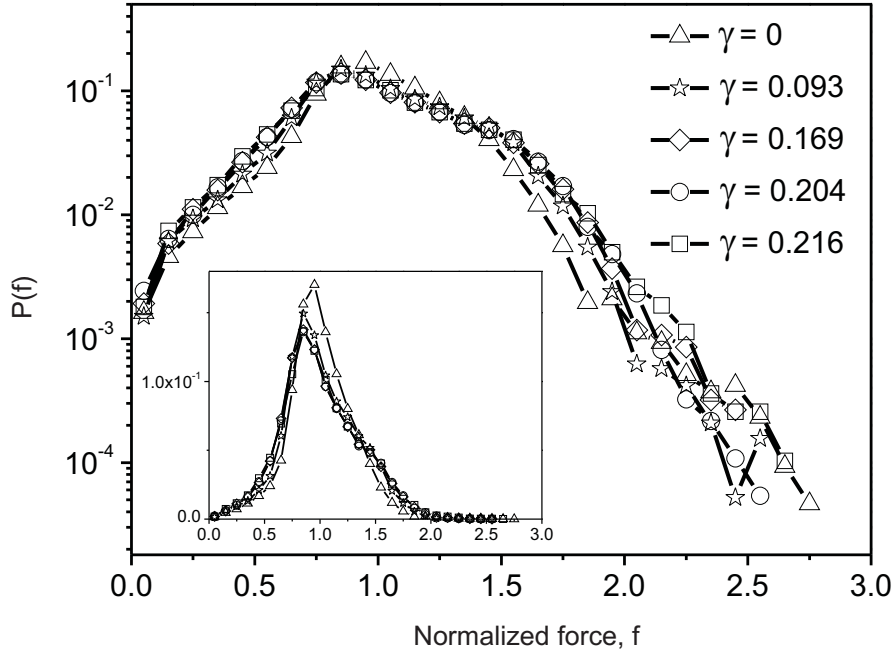


FIGURE 6.6. Probability distribution of the contact forces normalized by the average contact force for the suspension of jammed shells under shear.

shells along the gradient direction during the relaxation of bottom cassette. Further shear apparently did not change the average contact forces for the small shear strains sampled but the relative standard deviation ( $\sigma_F/\langle F \rangle$ ) increased slightly with increasing strain. This is perhaps not surprising, as shear deformation causes both a compression and an extension.

Figure 6.6 shows the distribution of contact force magnitude normalized by the average contact force,  $P(f)$  ( $f = F/\langle F \rangle$ ) for the different strain amplitudes. The distribution clearly became wider with an increase in the measured strain from  $\gamma = 0$  to  $\gamma = 0.216$ . The higher probability of large and small forces likely results from an increase in the deformations of approaching shells along the compression axis and a relaxation of receding shells along the extension axis. A similar broadening of the distribution under shear has been reported in granular materials under pure shear where the tail of the distribution became less steep than exponential with deformation [32]. To see if the observed changes in the shape of the force distribution indeed correlate with the compression/extension axes of the shear we now turn to the angular distribution of the contact forces.

#### *Angular distribution of the contact forces, $P(\theta)$*

Shear induced anisotropy in the orientation of the contact forces was analyzed by plotting the angle that the contact forces make with the velocity axis for all forces with a magnitude above the average as shown in Figure 6.7. Only the component of the

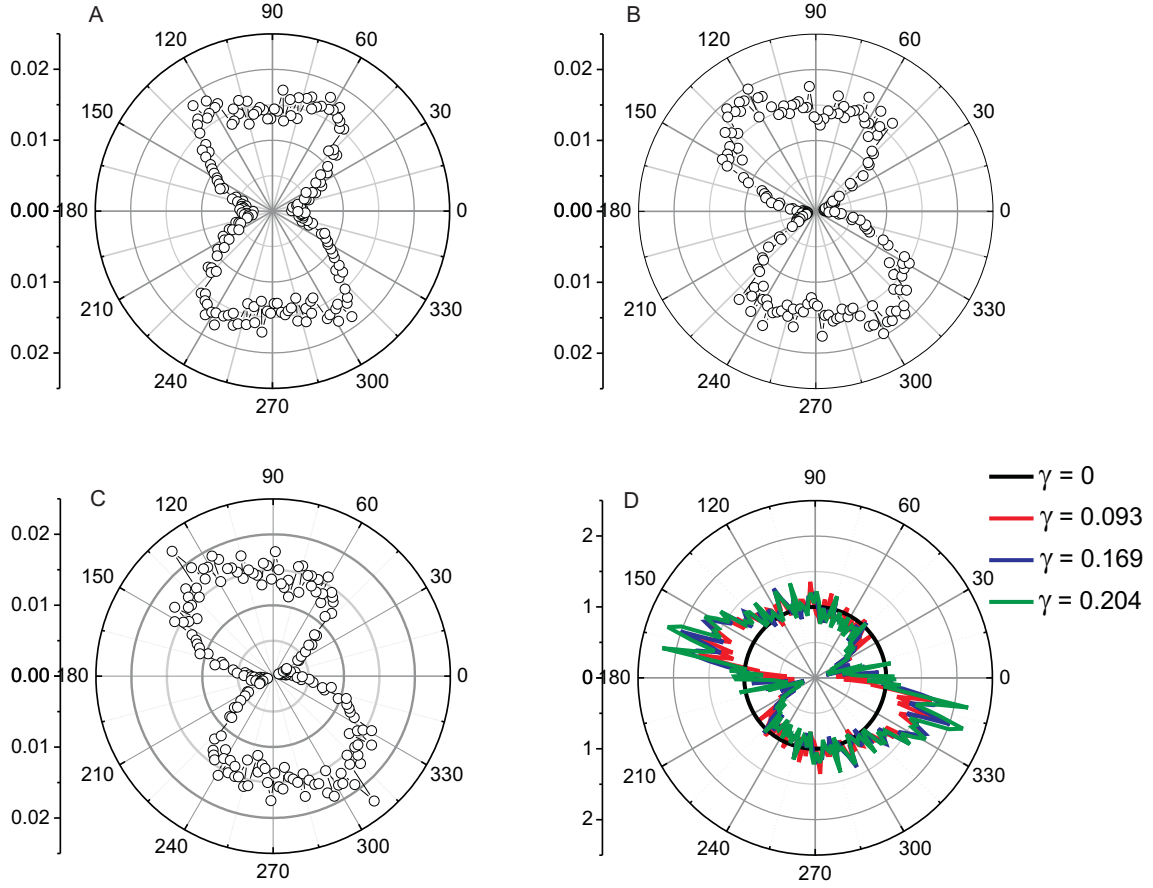


FIGURE 6.7. Probability distribution of contact angles carrying forces above average force with respect to velocity direction ( $X$ -axis) in the suspension of jammed shells (A) for  $\gamma = 0$  and at strain (B)  $\gamma = 0.093$  and (C)  $\gamma = 0.204$ . (D) Ratio of probability after shear to before shear for three values of strain amplitudes.

force in the  $XZ$ -plane was taken for the angle distribution. This distribution was found to be anisotropic even before the sample was sheared, due to the compression flow that was induced by lowering the upper plate onto the sample (Figure 6.7 A). With the applied strain we noticed a clear increase in the probability in the quadrants  $90^\circ$ - $180^\circ$  and  $270^\circ$ - $360^\circ$  (compression zone) and a decrease of  $P(\theta)$  in the other two quadrants (extension zone). The effect of shear becomes more clear in Figure 6.7 D where the ratio of the probability after shear to the reference sample (before shear) is plotted. Clearly, a large increase in the direction of large forces takes place between  $135^\circ$ - $170^\circ$  with a maximum around  $160^\circ$ . A corresponding large reduction is found between  $10^\circ$  and  $45^\circ$ , with a maximum at  $20^\circ$ . While these directions qualitatively correlate with the compression and extension axes of the shear there is a clear preference for a force build up at an angle of about  $20^\circ$  to the velocity direction.

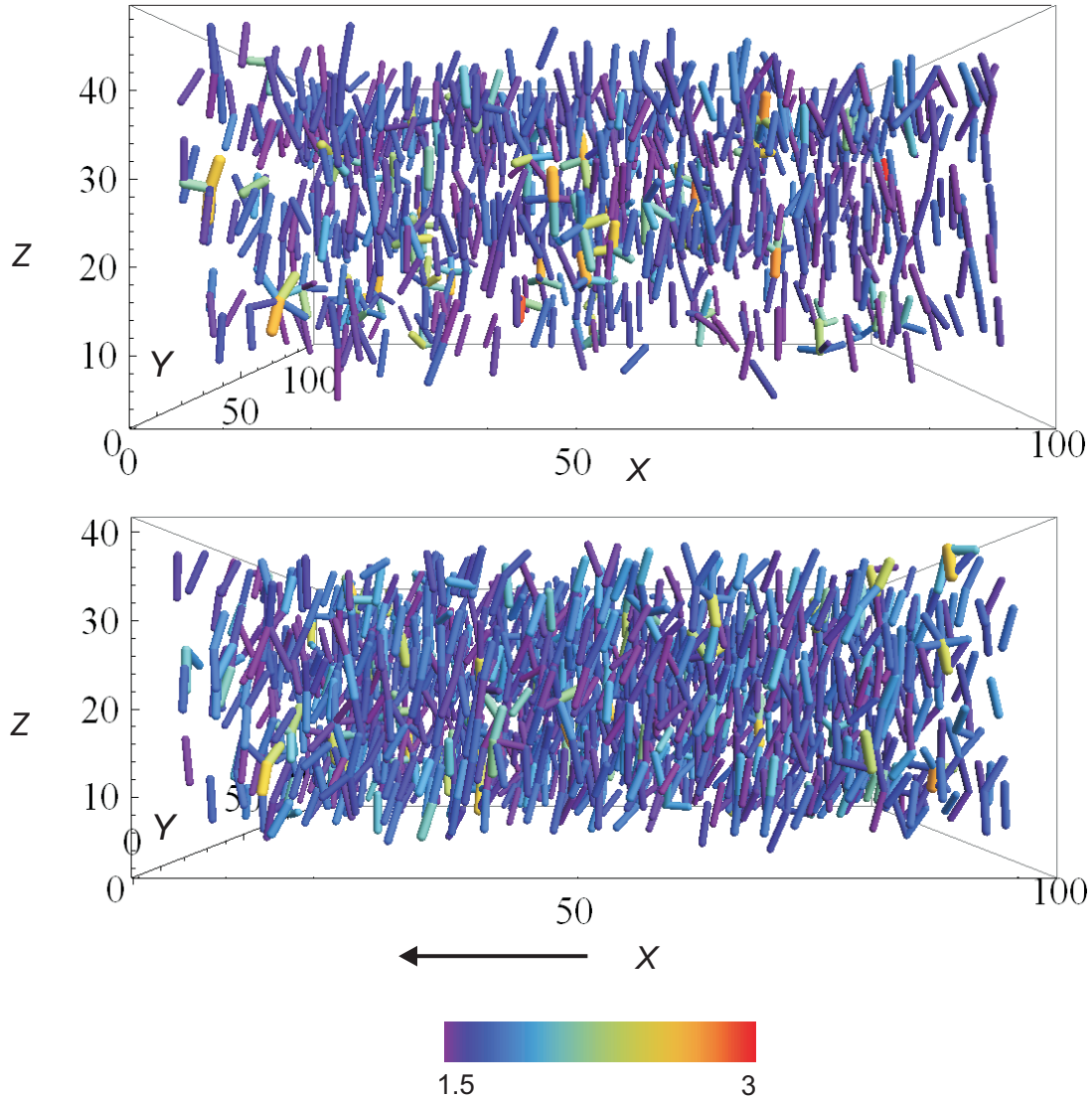


FIGURE 6.8. 3D force networks in jammed deformable shells showing only forces above 1.5 times average force. (A) Sample before shear,  $\gamma = 0$  and (B) after shear,  $\gamma = 0.169$ . Forces, in units of the average force  $\langle F \rangle$  are represented by tubes connecting the centers of contact pairs where the thickness and color of the tubes are proportional to the magnitude of the force.  $XZ$  is the velocity-gradient direction. The  $Z$  coordinate is increased by a factor of 1.5 for better visualization.

### *Force network*

The effect of shear on the 3D contact force network in the sample volume is depicted in Figure 6.8. Only forces above 1.5 times the average force are shown in the figure, where the thickness and color of the tubes represent the magnitude of the forces. In the sample at  $\gamma = 0$  large forces in the force network are mostly aligned along the gradient

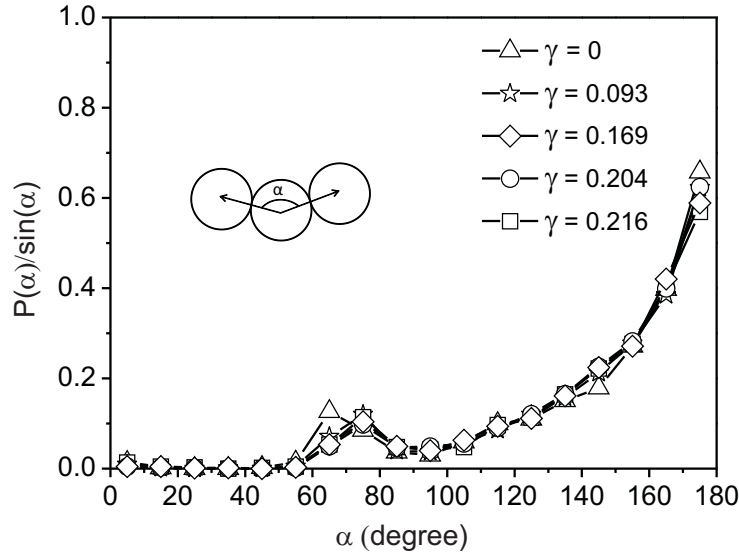


FIGURE 6.9. Probability distribution of the angles between the force segments in force chains normalized by the unit solid angle for different strains.

axis in layers due to the compression induced by the plate-plate confinement. As the sample was sheared the number of the force segments increased due to a build up of large forces in the compression zone. However, we did not see long chains of forces with increase in the strain.

To quantify the chain correlation we calculated the average length and persistence length of force chains as described in chapter 5 using the definition of a force chain in reference [134]. Note that according to this definition a force segment belongs to a force chain if it is one of the two largest forces on both particles joined by the force segment. The results are listed in Table 6.2. The chains are rather short and comparable in length to those in chapter 5, where the samples were not confined between plates. The effect of the shear appears to be only a very small increase in the persistence length, except for  $\gamma = 0.216$ . This could have resulted from the slip of particles near the wall. Figure 6.9 describes the probability of the angle between the force segments in a chain. The main effect of the shear was to displace the small local maximum from  $60^\circ$  to about  $75^\circ$  or a deformation of the local order around a particle.

#### *Amorphous packing of shells under a large strain*

A number of preliminary experiments with a larger strain was also conducted. This was possible only in a few cases without wall slip reducing the actual strain to a much lower value. These successful results do indicate that a significantly larger strain could be applied without slip after minimization of the slip. Figure 6.10 shows the confocal images ( $XZ$  mode) of amorphous packing of jammed shells taken after shearing the shells by an amount  $\gamma = 1.72$  and  $\gamma = 2.17$ . The two images were taken from different experiments and the applied shear rates were  $\dot{\gamma} = 7.8 \times 10^{-2} \text{ s}^{-1}$  and  $\dot{\gamma} = 2.8 \times 10^{-3} \text{ s}^{-1}$ .

Image stack	Measured strain	average chain length $\times \langle 2R_t \rangle$	Persistence length ( $\ell^*$ ) $\times \langle 2R_t \rangle$
Before shear	0	4.42	3.31
Shear1	0.093	4.61	3.51
Shear2	0.169	4.66	3.64
Shear3	0.204	4.93	3.76
Shear4	0.216	4.63	3.46

TABLE 6.2. The value of average length and persistence length of force chains for different shear strain.

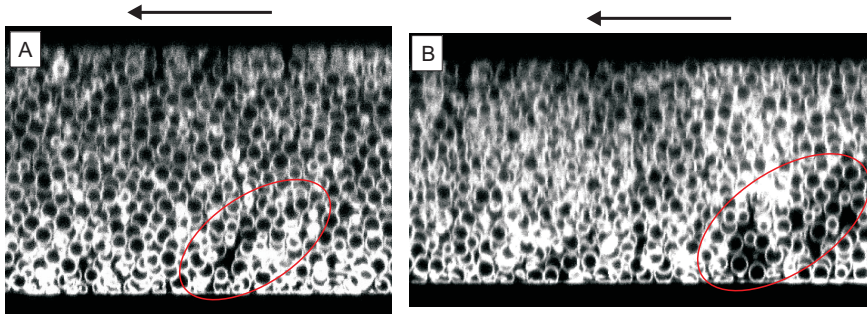


FIGURE 6.10. Confocal images in  $XZ$  mode of jammed shells under shear at much larger shear strain and shear rate in two different experiments. The systems underwent failure by developing cracks, in regions marked by red circles (A) at shear strain  $\gamma = 1.72$  and shear rate  $\dot{\gamma} = 7.8 \times 10^{-2} \text{ s}^{-1}$  and (B) for the jammed suspension of shells at shear strain  $\gamma = 2.17$  and shear rate  $\dot{\gamma} = 2.8 \times 10^{-3} \text{ s}^{-1}$ .

We didn't perform quantitative analysis on these systems, but the observations revealed that the packings of jammed shells at these relatively large strains and shear rates do undergo fracture. In Figure 6.10 A and B cracks that developed during the strain in the sample can be seen along the direction approximately normal to the direction of extension. The formation of cracks is a likely indication that the jammed packings of shells behaved like a brittle amorphous solid under this shear rate and much larger strain than in the previous experiments .

## 6.4 CONCLUSIONS

We discussed our preliminary results on jammed packing of shells under shear. Although shear deformation was small ( $\gamma \leq 0.216$ ) the microstructure and contact force network showed anisotropy with increase in strain. We observed an increase in the probability of forces both larger and smaller than average, correlating with the compression and extension axes of the shear, respectively. Interestingly, the largest changes

in the contact forces were seen not at  $\pm 45^\circ$  to the velocity axis but at  $\pm 20^\circ$ . However, due to the small strains, no appreciable change was observed in the distribution of contact number. That means the rearrangement of particles was almost absent in the system. Apparently, the system was only elastically deformed by the applied stress. It would be interesting to carry out quantitative studies at even higher values of strain, provided we solve the wall slip problem by introducing a better adhesion between the shells and the walls.

## 6.5 ACKNOWLEDGMENTS

We thank Peter Helfferich for his assistance in operating shear cell setup, Thijs Besseling for useful discussions about the shear cell and Bas Kwaadgras for modifying the  $g(r)$  program.



# Bibliography

- [1] R.J. Hunter. *Foundations of colloid science*. Oxford University Press, Oxford, 2nd edn, 2001.
- [2] I.W. Hamley. *Introduction to Soft Matter: polymer, colloids, amphiphiles and liquid crystals*. 2000.
- [3] P.N. Pusey and W. Van Megen. Phase behaviour of concentrated suspensions of nearly hard colloidal spheres. *Nature*, 320:340–342, 1986.
- [4] W. Van Megen and P.N. Pusey. Dynamic light-scattering study of the glass transition in a colloidal suspension. *Physical Review A*, 43:5429, 1991.
- [5] T.G. Mason and D.A. Weitz. Linear viscoelasticity of colloidal hard sphere suspensions near the glass transition. *Physical Review Letters*, 75:2770, 1995.
- [6] W.K. Kegel and A. van Blaaderen. Direct observation of dynamical heterogeneities in colloidal hard-sphere suspensions. *Science*, 287:290–293, 2000.
- [7] E.R. Weeks, J.C. Crocker, A.C. Levitt, A. Schofield, and D.A. Weitz. Three-dimensional direct imaging of structural relaxation near the colloidal glass transition. *Science*, 287:627–631, 2000.
- [8] C.A. Angell, K.L. Ngai, G.B. McKenna, P.F. McMillan, and S.W. Martin. Relaxation in glassforming liquids and amorphous solids. *Journal of applied physics*, 88:3113–3157, 2000.
- [9] L.K.A. Dorren. A review of rockfall mechanics and modelling approaches. *Progress in Physical Geography*, 27:69–87, 2003.
- [10] S. De Toni and P. Scotton. Two-dimensional mathematical and numerical model for the dynamics of granular avalanches. *Cold regions science and technology*, 43:36–48, 2005.
- [11] W.R. Ketterhagen, J.S. Curtis, C.R. Wassgren, and B.C. Hancock. Modeling granular segregation in flow from quasi-three-dimensional, wedge-shaped hoppers. *Powder Technology*, 179:126–143, 2008.
- [12] F.Y. Fraige, P.A. Langston, and G.Z. Chen. Distinct element modelling of cubic particle packing and flow. *Powder Technology*, 186:224–240, 2008.
- [13] E.D. Lachiver, N. Abatzoglou, L. Cartilier, and J.S. Simard. Agglomeration tendency in dry pharmaceutical granular systems. *European journal of pharmaceuticals and biopharmaceutics*, 64:193–199, 2006.
- [14] K. Lee, T. Kim, P. Rajniak, and T. Matsoukas. Compositional distributions in multicomponent aggregation. *Chemical Engineering Science*, 63:1293–1303, 2008.
- [15] M. van Hecke. Shape matters. *Science*, 317:49, 2007.
- [16] M. van Hecke. Granular matter - a tale of tails. *Nature*, 435:1041–1042, 2005.
- [17] H.P. Zhu, Z.Y. Zhou, R.Y. Yang, and A.B. Yu. Discrete particle simulation of particulate systems: theoretical developments. *Chemical Engineering Science*, 62:3378–3396, 2007.
- [18] M.E. Cates, J.P. Wittmer, J.P. Bouchaud, and P. Claudin. Jamming, force chains, and fragile matter. *Physical Review Letters*, 81:1841–1844, 1998.
- [19] C.H. Liu, S.R. Nagel, D.A. Schecter, S.N. Coppersmith, S. Majumdar, O. Narayan, and T.A. Witten. Force fluctuations in bead packs. *Science*, 269:513–515, 1995.
- [20] W. Kob, C. Donati, S.J. Plimpton, P.H. Poole, and S.C. Glotzer. Dynamical heterogeneities in a supercooled lennard-jones liquid. *Physical Review Letters*, 79:2827, 1997.
- [21] S.A. Langer and A.J. Liu. Effect of random packing on stress relaxation in foam. *The Journal of Physical Chemistry B*, 101:8667–8671, 1997.
- [22] M.D. Ediger. Spatially heterogeneous dynamics in supercooled liquids. *Annual review of physical chemistry*, 51:99–128, 2000.

- [23] D. Kivelson and G. Tarjus. Superarrhenius character of supercooled glass-forming liquids. *Journal of non-crystalline solids*, 235:86–100, 1998.
- [24] P.N. Pusey and W. van Megen. Observation of a glass transition in suspensions of spherical colloidal particles. *Physical Review Letters*, 59:2083–2086, 1987.
- [25] G. D’Anna and G. Gremaud. Vogel-fulcher-tammanntype diffusive slowdown in weakly perturbed granular media. *Physical Review Letters*, 87:254302, 2001.
- [26] C.S. O’Hern, S.A. Langer, A.J. Liu, and S.R. Nagel. Force distributions near jamming and glass transitions. *Physical Review Letters*, 86:111–114, 2001.
- [27] J. Brujic, S.F. Edwards, D.V. Grinev, I. Hopkinson, D. Brujic, and H.A. Makse. 3d bulk measurements of the force distribution in a compressed emulsion system. *Faraday discussions*, 123:207–220, 2003.
- [28] G. Katgert and M. van Hecke. Jamming and geometry of two-dimensional foams. *Europhysics Letters*, 92:34002, 2010.
- [29] A.J. Liu and S.R. Nagel. Nonlinear dynamics: Jamming is not just cool any more. *Nature*, 396:21–22, 1998.
- [30] C.S. O’Hern, L. E. Silbert, A.J. Liu, and S.R. Nagel. Jamming at zero temperature and zero applied stress: The epitome of disorder. *Physical Review E*, 68:011306, 2003.
- [31] V. Trappe, V. Prasad, L. Cipelletti, P.N. Segre, and D.A. Weitz. Jamming phase diagram for attractive particles. *Nature*, 411:772–775, 2001.
- [32] T.S. Majmudar and R.P. Behringer. Contact force measurements and stress induced anisotropy in granular materials. *Nature*, 435:1079–1082, 2005.
- [33] D.M. Mueth, H.M. Jaeger, and S.R. Nagel. Force distribution in a granular medium. *Physical Review E*, 57:3164, 1998.
- [34] L.S. Zha, Y. Zhang, W.L. Yang, and S.K. Fu. Monodisperse temperature-sensitive microcontainers. *Advanced Materials*, 14:1090–1092, 2002.
- [35] J. Berg, D. Sundberg, and B. Kronberg. Microencapsulation of emulsified oil droplets by in-situ vinyl polymerization. *Journal of Microencapsulation*, 6:327–337, 1989.
- [36] F.A. Tiarks, K. Landfester, and M. Antonietti. Preparation of polymeric nanocapsules by miniemulsion polymerization. *Langmuir*, 17:908–918, 2001.
- [37] E. Donath, G. B. Sukhorukov, F. Caruso, S.A. Davis, and H. Möhwald. Novel hollow polymer shells by colloid-templated assembly of polyelectrolytes. *Angew. Chem. Int. Ed.*, 37(16), 1998.
- [38] F. J Rossier-Miranda, C.G.P.H. Schron, and R.M. Boom. Colloidosomes: Versatile microcapsules in perspective. *Colloids and Surfaces A: Physicochemical and Engineering Aspects*, 343:43–49, 2009.
- [39] C.I. Zoldesi and A. Imhof. Synthesis of monodisperse colloidal spheres, capsules, and microballoons by emulsion templating. *Advanced Materials*, 17:924–928, 2005.
- [40] B. Städler, A.D. Price, R. Chandrawati, L. Hosta-Rigau, A.N. Zelikin, and F. Caruso. Polymer hydrogel capsules: en route toward synthetic cellular systems. *Nanoscale*, 1:68–73, 2009.
- [41] F. Caruso. Hollow capsule processing through colloidal templating and self-assembly. *Chem. Eur. J.*, 6:413–419, 2000.
- [42] F. Caruso, W. Yang, D. Trau, and R. Renneberg. Microencapsulation of uncharged low molecular weight organic materials by polyelectrolyte multilayer self-assembly. *Langmuir*, 16:8932–8936, 2000.

- [43] R. Georgieva, S. Moya, M. Hin, R. Mitlhner, E. Donath, H. Kiesewetter, H. Möhwald, and H. Bäuml. Permeation of macromolecules into polyelectrolyte microcapsules. *Biomacromolecules*, 3:517–524, 2002.
- [44] G.B. Sukhorukov, A. A. Antipov, A. Voigt, E. Donath, and H. Möhwald. pH-controlled macromolecule encapsulation in and release from polyelectrolyte multilayer nanocapsules. *Macromolecular Rapid Communications*, 22:44–46, 2001.
- [45] Gibbs B.F., Selim K., Inteaz A., and Catherine N.M. Encapsulation in the food industry: a review. *International Journal of Food Sciences and Nutrition*, 50:213–224, 1999.
- [46] M.S. Romero-Cano and B. Vincent. Controlled release of 4-nitroanisole from poly (lactic acid) nanoparticles. *Journal of Controlled Release*, 82(1):127–135, 2002.
- [47] M. Delcea, H. Möhwald, and A.G. Skirtach. Stimuli-responsive lbl capsules and nanoshells for drug delivery. *Advanced Drug Delivery Reviews*, 63:730–747, 2011.
- [48] S. De Koker, L.J. De Cock, P. Rivera-Gil, W.J. Parak, R. Auzly Veltly, C. Vervaet, J.P. Remon, J. Grooten, and B.G. De Geest. Polymeric multilayer capsules delivering biotherapeutics. *Advanced Drug Delivery Reviews*, 63:748–761, 2011.
- [49] S.A. Sukhishvili. Responsive polymer films and capsules via layer-by-layer assembly. *Current Opinion in Colloid & Interface Science*, 10:37–44, 2005.
- [50] R. Langer. Drug delivery and targeting. *Nature*, 392:5–10, 1998.
- [51] C.S. Peyratout and L. Dahne. Tailor-made polyelectrolyte microcapsules: From multilayers to smart containers. *Angew.Chem.Int.Ed.*, 43:3762–3783, 2004.
- [52] A.P.R. Johnston, C. Cortez, A.S. Angelatos, and F. Caruso. Layer-by-layer engineered capsules and their applications. *Curr. Opin. Colloid Interface Sci.*, 11:203–209, 2006.
- [53] K. Ariga, J.P. Hill, M.V. Lee, A. Vinu, R. Charvet, and S. Acharya. Challenges and breakthroughs in recent research on self-assembly. *Sci. Technol. Adv. Mater.*, 9:1–96, 2008.
- [54] D.M. Vriezema, M.C. Aragonés, J. Elemans, J. Cornelissen, A.E. Rowan, and R.J.M. Nolte. Self-assembled nanoreactors. *Chemical Reviews*, 105:1445–1489, 2005.
- [55] H.N. Yow and A.F. Routh. Formation of liquid corepolymer shell microcapsules. *Soft Matter*, 2:940–949, 2006.
- [56] F. Caruso, R.A. Caruso, and H. Möhwald. Nanoengineering of inorganic and hybrid hollow spheres by colloidal templating. *Science*, 282:1111–1114, 1998.
- [57] X.L. Xu and S.A. Asher. Synthesis and utilization of monodisperse hollow polymeric particles in photonic crystals. *Journal of the American Chemical Society*, 126:7940–7945, 2004.
- [58] K. Kamata, Y. Lu, and Y.N. Xia. Synthesis and characterization of monodispersed core-shell spherical colloids with movable cores. *Journal of the American Chemical Society*, 125:2384–2385, 2003.
- [59] A. Imhof. Preparation and characterization of titania-coated polystyrene spheres and hollow titania shells. *Langmuir*, 17:3579–3585, 2001.
- [60] C. Graf, D.L.J. Vossen, A. Imhof, and A. van Blaaderen. A general method to coat colloidal particles with silica. *Langmuir*, 19:6693–6700, 2003.
- [61] X.W.D. Lou, L.A. Archer, and Z. Yang. Hollow micro-/nanostructures: Synthesis and applications. *Advanced Materials*, 20:3987–4019, 2008.
- [62] M. Horecha, V. Senkovskyy, M. Stamm, and A. Kiriy. One-pot synthesis of thermoresponsive pNIPAM hydrogel microcapsules designed to function in apolar media. *Macromolecules*, 42:5811–5817, 2009.

- [63] E. Tjijto, K.D. Cadwell, J.F. Quinn, A.P.R. Johnston, N. L. Abbott, and F. Caruso. Tailoring the interfaces between nematic liquid crystal emulsions and aqueous phases via layer-by-layer assembly. *Nano Letters*, 6:2243–2248, 2006.
- [64] D.G. Shchukin, K. Khler, H. Mhwald, and G.B. Sukhorukov. Gas filled polyelectrolyte capsules. *Angewandte Chemie International Edition*, 44:3310–3314, 2005.
- [65] A.P. Esser-Kahn, S.A. Odom, N.R. Sottos, S.R. White, and J.S. Moore. Triggered release from polymer capsules. *Macromolecules*, 44:5539–5553, 2011.
- [66] B. Abismal, J.P. Canselier, A.M. Wilhelm, H. Delmas, and C. Gourdon. Emulsification by ultrasound: drop size distribution and stability. *Ultrasonics Sonochemistry*, 6:75–83, 1999.
- [67] W. T. Richards. The chemical effects of high frequency sound waves ii. a study of emulsifying action. *Journal of the American Chemical Society*, 51:1724–1729, 1929.
- [68] P. Hsu, P. Poulin, and D.A. Weitz. Rotational diffusion of monodisperse liquid crystal droplets. *Journal of Colloid and Interface Science*, 200:182–184, 1998.
- [69] J. Bibette. Depletion interactions and fractionated crystallization for polydisperse emulsion purification. *Journal of Colloid and Interface Science*, 147:474–478, 1991.
- [70] T.G Mason and J. Bibette. Emulsification in viscoelastic media. *Physical Review Letters*, 77:3481, 1996.
- [71] C. Priest, A. Quinn, A. Postma, A.N. Zelikin, J. Ralston, and F. Caruso. Microfluidic polymer multilayer adsorption on liquid crystal droplets for microcapsule synthesis. *Lab on a Chip*, 8:2182–2187, 2008.
- [72] W. Engl, R. Backov, and P. Panizza. Controlled production of emulsions and particles by milli- and microfluidic techniques. *Current Opinion in Colloid and Interface Science*, 13:206–216, 2008.
- [73] A.S. Utada, E.I. Lorenceau, D.R. Link, P.D. Kaplan, H.A. Stone, and D.A. Weitz. Monodisperse double emulsions generated from a microcapillary device. *Science*, 308:537–541, 2005.
- [74] W.J. Duncanson, T. Lin, A.R. Abate, S. Seiffert, R.K. Shah, and D.A. Weitz. Microfluidic synthesis of advanced microparticles for encapsulation and controlled release. *Lab on a Chip*, 12:2135–2145, 2012.
- [75] C. Berkland, K.K. Kim, and D. W. Pack. Fabrication of plg microspheres with precisely controlled and monodisperse size distributions. *Journal of Controlled Release*, 73:59–74, 2001.
- [76] C. Berkland, E. Pollauf, N. Varde, D.W. Pack, and K.K. Kim. Monodisperse liquid-filled biodegradable microcapsules. *Pharmaceutical Research*, 24:1007–1013, 2007.
- [77] D.S. Kohane. Microparticles and nanoparticles for drug delivery. *Biotechnology and Bioengineering*, 96:203–209, 2007.
- [78] Van-T. Tran, Jean-P. Benot, and Marie-C. Venier-Julienne. Why and how to prepare biodegradable, monodispersed, polymeric microparticles in the field of pharmacy? *International Journal of Pharmaceutics*, 407:1–11, 2011.
- [79] T.M. Obey and B. Vincent. Novel monodisperse silicone oil-water emulsions. *Journal of Colloid and Interface Science*, 163:454–463.
- [80] M. O’Sullivan, Z.B. Zhang, and B. Vincent. Silica-shell/oil-core microcapsules with controlled shell thickness and their breakage stress. *Langmuir*, 25:7962–7966, 2009.
- [81] J.W. Cui, Y.J. Wang, A. Postma, J.C. Hao, L. Hosta-Rigau, and F. Caruso. Monodisperse polymer capsules: Tailoring size, shell thickness, and hydrophobic cargo loading via emulsion templating. *Advanced Functional Materials*, 20:1625–1631, 2010.
- [82] C. A. Prestidge, T. Barnes, and S. Simovic. Polymer and particle adsorption at the pdms droplet-water interface. *Advances in Colloid and Interface Science*, 108:105–118, 2004.

- [83] T. Ohta, D. Nagao, H. Ishii, and M. Konno. Preparation of oil-containing, polymeric particles having a single depression with various shapes. *Soft Matter*, 8:4652–4658, 2012.
- [84] A.G. Skirtach, A.M. Yashchenok, and H. Möhwald. Encapsulation, release and applications of lbl polyelectrolyte multilayer capsules. *Chemical Communications*, 47:12736–12746, 2011.
- [85] M.A. Yaseen, J. Yu, B. Jung, M.S. Wong, and B. Anvari. Biodistribution of encapsulated indocyanine green in healthy mice. *Molecular pharmaceuticals*, 6:1321–1332, 2009.
- [86] P.A.L. Fernandes, M. Delcea, A.G. Skirtach, H. Möhwald, and A. Fery. Quantification of release from microcapsules upon mechanical deformation with afm. *Soft Matter*, 6:1879–1883, 2010.
- [87] C.Y. Gao, E. Donath, H. Möhwald, and J. C. Shen. Spontaneous deposition of water-soluble substances into microcapsules: Phenomenon, mechanism, and application. *Angew. Chem. Int. Ed.*, 41:3789–3793, 2002.
- [88] J. Zhang, R.J. Coulston, S.T. Jones, J. Geng, O.A. Scherman, and C. Abell. One-step fabrication of supramolecular microcapsules from microfluidic droplets. *Science*, 335:690–694, 2012.
- [89] C. Li, Z.-Y. Li, J. Zhang, K. Wang, Y.-H. Gong, G.-F. Luo, R.-X. Zhuo, and X.-Z. Zhang. Porphyrin containing light-responsive capsules for controlled drug release. *Journal of Materials Chemistry*, 22:4623–4626, 2012.
- [90] C.I. Zoldesi, C.A. van Walree, and A. Imhof. Deformable hollow hybrid silica/siloxane colloids by emulsion templating. *Langmuir*, 22:4343–4352, 2006.
- [91] Nina Elbers. Thesis.
- [92] A.J. Liu and S.R. Nagel. Granular and jammed materials. *Soft Matter*, 6:2869–2870, 2010.
- [93] J. Brujic, S. F. Edwards, I. Hopkinson, and H.A. Makse. Measuring the distribution of interdroplet forces in a compressed emulsion system. *Physica A: Statistical Mechanics and its Applications*, 327:201212, 2003.
- [94] O. Seok Kwon, J. Jang, and J. Bae. A review of fabrication methods and applications of novel tailored microcapsules. *Current Organic Chemistry*, 17:3–13, 2013.
- [95] R. Xie, U. Kolb, J. Li, T. Basche, and A. Mews. Synthesis and characterization of highly luminescent cdse-core cds/zno. 5cd0. 5s/zns multishell nanocrystals. *Journal of the American Chemical Society*, 127:7480–7488, 2005.
- [96] T.G. Mason and J. Bibette. Shear rupturing of droplets in complex fluids. *Langmuir*, 13:4600–4613, 1997.
- [97] C.F. Bohren and D.R. Huffman. *Absorption and scattering of light by small particles*. Wiley. com, 2008.
- [98] J.A. Moore and A.L. Smith. *The Analytical Chemistry of Silicones*, volume 112. Wiley-Interscience: New York, 1991.
- [99] C.I. Zoldesi, P. Steegstra, and A. Imhof. Encapsulation of emulsion droplets by organosilica shells. *Journal of Colloid and Interface Science*, 308:121–129, 2007.
- [100] K. R. Anderson, T.M. Obey, and B. Vincent. Surfactant-stabilized silicone oil in water emulsions. *Langmuir*, 10:2493–2494, 1994.
- [101] B. Neumann, B. Vincent, R. Krustev, and H. Müller. Stability of various silicone oil/water emulsion films as a function of surfactant and salt concentration. *Langmuir*, 20:4336–4344, 2004.
- [102] G.H. Bogush, M.A. Tracy, and C.F. Zukoski. Preparation of monodisperse silica particles: control of size and mass fraction. *Journal of Non-Crystalline Solids*, 104:95–106, 1988.
- [103] Y. Zhang and R. M. Miller. Effect of a pseudomonas rhamnolipid biosurfactant on cell hydrophobicity and biodegradation of octadecane. *Applied and Environmental Microbiology*, 60:2101–2106, 1994.

- [104] <http://avogadro.chem.iastate.edu/msds/pentane.htm>.
- [105] <http://www.epa.gov/chemfact/s.cycloh.txt>.
- [106] N. Tsuda, T. Ohtsubo, and M. Fuji. Preparation of self-bursting microcapsules by interfacial polymerization. *Advanced Powder Technology*, 23:724–730, 2012.
- [107] B.G. De Geest, N.N. Sanders, G.B. Sukhorukov, J. Demeester, and S.C. De Smedt. Release mechanisms for polyelectrolyte capsules. *Chemical Society Reviews*, 36:636–649, 2007.
- [108] G. Sukhorukov, L. Dahne, J. Hartmann, E. Donath, and H. Möhwald. Controlled precipitation of dyes into hollow polyelectrolyte capsules based on colloids and biocolloids. *Advanced Materials*, 12:112–115, 2000.
- [109] Y. Lvov, A.A. Antipov, A. Mamedov, H. Möhwald, and G.B. Sukhorukov. Urease encapsulation in nanoorganized microshells. *Nano Letters*, 1:125–128, 2001.
- [110] A.A. Antipov and G.B. Sukhorukov. Polyelectrolyte multilayer capsules as vehicles with tunable permeability. *Advances in Colloid and Interface Science*, 111:49–61, 2004.
- [111] P. R. Gil, L. L. del Mercato, P. del Pino, A. Muñoz-Javier, and W. J. Parak. Nanoparticle-modified polyelectrolyte capsules. *Nano Today*, 3:12–21, 2008.
- [112] G.A. Vliegthart and G. Gompper. Compression, crumpling and collapse of spherical shells and capsules. *New J.Phys.*, 13, 2011.
- [113] C. Quilliet, C. Zoldesi, C. Riera, A. van Blaaderen, and A. Imhof. Anisotropic colloids through non-trivial buckling. *Eur. Phys. J. E*, 27:13–20, 2008.
- [114] C. Gao, E. Donath, S. Moya, V. Dudnik, and H. Möhwald. Elasticity of hollow polyelectrolyte capsules prepared by the layer-by-layer technique. *Eur. Phys. J. E*, 5:21–27, 2001.
- [115] S. S. Datta, S.H. Kim, J. Paulose, A. Abbaspourrad, D.R. Nelson, and D.A. Weitz. Delayed buckling and guided folding of inhomogeneous capsules. *Physical Review Letters*, 109:134302, 2012.
- [116] C.I. Zoldesi, I.L. Ivanovska, C. Quilliet, G.J.L. Wuite, and A. Imhof. Elastic properties of hollow colloidal particles. *Phys. Rev. E*, 78:051401, 2008.
- [117] L.D. Landau and E.M. Lifshitz. *Theory of Elasticity*. Pergamon, New York, 1986.
- [118] A.V. Pogorelov. *Bendings of surfaces and stability of shells*. American Mathematical Society, Providence, 1988.
- [119] W. W. Yu, L. Qu, W. Guo, and X. Peng. Experimental determination of the extinction coefficient of cdte, cdse, and cds nanocrystals. *Chemistry of Materials*, 15:2854–2860, 2003.
- [120] G. Wanka, H. Hoffmann, and W. Ulbricht. Phase-diagrams and aggregation behavior of poly(oxyethylene)-poly(oxypropylene)-poly(oxyethylene) triblock copolymers in aqueous-solutions. *Macromolecules*, 27:4145–4159, 1994.
- [121] J. Bibette, D. Roux, and F. Nallet. Depletion interactions and fluid-solid equilibrium in emulsions. *Physical Review Letters*, 65:2470–2473, 1990.
- [122] S. Sacanna, W.T.M. Irvine, P.M. Chaikin, and D.J. Pine. Lock and key colloids. *Nature*, 464:575–578, 2010.
- [123] S. Knoche and J. Kierfeld. Buckling of spherical capsules. *Phys. Rev. E*, 84:046608, 2011.
- [124] L. Pauchard and S. Rica. Contact and compression of elastic spherical shells: the physics of a ‘ping-pong’ ball. *Phil. Mag. B*, 78:225–233, 1998.
- [125] S.S. Datta, H.C. Shum, and D.A. Weitz. Controlled buckling and crumpling of nanoparticle-coated droplets. *Langmuir*, 26:18612–18616, 2010.

- [126] M. Okubo, H. Minami, and K. Morikawa. Production of micron-sized, monodisperse, transformable rugby-ball-like-shaped polymer particles. *Colloid and Polymer Science*, 279:931–935, 2001.
- [127] E. Katifori, S. Alben, E. Cerda, D.R. Nelson, and J. Dumais. Foldable structures and the natural design of pollen grains. *PNAS*, 107(17):7635–7639, 2010.
- [128] R. Pericet-Camara, A. Best, H.J. Butt, and E. Bonaccorso. Effect of capillary pressure and surface tension on the deformation of elastic surfaces by sessile liquid microdrops: An experimental investigation. *Langmuir*, 24:10565–10568, 2008.
- [129] D.L. Blair, N.W. Mueggenburg, A.H. Marshall, H.M. Jaeger, and S.R. Nagel. Force distributions in three-dimensional granular assemblies: Effects of packing order and interparticle friction. *Physical Review E*, 63:041304, 2001.
- [130] J.M. Erikson, N.W. Mueggenburg, H.M. Jaeger, and S.R. Nagel. Force distributions in three-dimensional compressible granular packs. *Physical Review E*, 66:040301, 2002.
- [131] G. Lvoll, K.J. Mly, and E.G. Flekky. Force measurements on static granular materials. *Physical Review E*, 60:5872, 1999.
- [132] T.S. Majmudar, M. Sperl, S. Luding, and R.P. Behringer. Jamming transition in granular systems. *Physical Review Letters*, 98:058001, 2007.
- [133] J. Zhou, S. Long, Q. Wang, and A.D. Dinsmore. Measurement of forces inside a three-dimensional pile of frictionless droplets. *Science*, 312:1631–1633, 2006.
- [134] K.W. Desmond, P.J. Young, D.D. Chen, and E.R. Weeks. Experimental study of forces between quasi-two-dimensional emulsion droplets near jamming. *Soft Matter*, 9:3424–3436, 2013.
- [135] M.A. Bevan and S.L. Eichmann. Optical microscopy measurements of kt scale colloidal interactions. *Current Opinion in Colloid and Interface Science*, 16:149–157, 2011.
- [136] L. Isa, R. Besseling, A.B. Schofield, and W.C.K. Poon. *Quantitative imaging of concentrated suspensions under flow*. Springer, 2010.
- [137] A. Van Blaaderen. *Quantitative real-space analysis of colloidal structures and dynamics with confocal scanning light microscopy*. Springer, 1997.
- [138] V. Prasad, D. Semwogerere, and E.R. Weeks. Confocal microscopy of colloids. *Journal of Physics: Condensed Matter*, 19:113102, 2007.
- [139] M.C. Jenkins and S.U. Egelhaaf. Confocal microscopy of colloidal particles: Towards reliable, optimum coordinates. *Advances in colloid and interface science*, 136:65–92, 2008.
- [140] A. Van Blaaderen and P. Wiltzius. Real-space structure of colloidal hard-sphere glasses. *Science*, 270:1177–1177, 1995.
- [141] J.C. Crocker and D.G. Grier. Methods of digital video microscopy for colloidal studies. *Journal of colloid and interface science*, 179:298–310, 1996.
- [142] A. Mohraz and M.J. Solomon. Direct visualization of colloidal rod assembly by confocal microscopy. *Langmuir*, 21:5298–5306, 2005.
- [143] A. Kuijk, A. van Blaaderen, and A. Imhof. Synthesis of monodisperse, rodlike silica colloids with tunable aspect ratio. *Journal of the American Chemical Society*, 133:2346–2349, 2011.
- [144] T. H. Besseling, M. Hermes, A. Kuijk, B. Peng, B. de Nijs, T. Deng, M. Dijkstra, A. Imhof, and A. van Blaaderen. Determination of the position and orientation of concentrated rod-like colloids from confocal microscopy images in two and three dimensions. *in preparation*.
- [145] S. Sacanna and D.J. Pine. Shape-anisotropic colloids: Building blocks for complex assemblies. *Current Opinion in Colloid and Interface Science*, 16:96–105, 2011.

- [146] D.J. Kraft, R. Wittkowski, B. ten Hagen, K.V. Edmond, D.J. Pine, and H. Löwen. Brownian motion and the hydrodynamic friction tensor for colloidal particles of complex shape. *Physical Review E*, 88:050301, 2013.
- [147] S. Anthony, L. Zhang, and S. Granick. Methods to track single-molecule trajectories. *Langmuir*, 22:5266–5272, 2006.
- [148] S.M. Anthony, M. Kim, and S. Granick. Translation-rotation decoupling of colloidal clusters of various symmetries. *The Journal of chemical physics*, 129:244701–244707, 2008.
- [149] ImageJ. <http://rsb.info.nih.gov/ij/index.html>.
- [150] T.J. Collins. Imagej for microscopy. *Biotechniques*, 43:25–30, 2007.
- [151] M.D. Abramoff, P.J. Magalhães, and S.J. Ram. Image processing with imagej. *Biophotonics international*, 11:36–42, 2004.
- [152] S. Hell, G. Reiner, C. Cremer, and E.H.K. Stelzer. Aberrations in confocal fluorescence microscopy induced by mismatches in refractive index. *Journal of microscopy*, 169:391–405, 1993.
- [153] T. H. Besseling, J. Jose, and A. van Blaaderen. Methods to calibrate and scale axial distances in confocal microscopy as a function of refractive index. *in preparation*.
- [154] O.R. Vincent and O. Folorunso. A descriptive algorithm for sobel image edge detection. *Proceedings of Informing Science and IT Education Conference*, 2009.
- [155] E.R. Davies. *Machine vision: theory, algorithms, practicalities*. Morgan Kaufmann, 2004.
- [156] J.E. Bresenham. Algorithm for computer control of a digital plotter. *IBM Systems journal*, 4:25–30, 1965.
- [157] C.S. O’Hern, S.A. Langer, A.J. Liu, and S.R. Nagel. Random packings of frictionless particles. *Physical Review Letters*, 88, 2002.
- [158] D.W. Howell, R.P. Behringer, and C.T. Veje. Fluctuations in granular media. *Chaos: An Interdisciplinary Journal of Nonlinear Science*, 9:559–572, 1999.
- [159] H.A. Makse, D.L. Johnson, and L.M. Schwartz. Packing of compressible granular materials. *Physical Review Letters*, 84:4160, 2000.
- [160] H.P. Zhang and H.A. Makse. Jamming transition in emulsions and granular materials. *Physical Review E*, 72:011301, 2005.
- [161] A.O.N Siemens and M. Van Hecke. Jamming: A simple introduction. *Physica A: Statistical Mechanics and its Applications*, 389:4255–4264, 2010.
- [162] M. van Hecke. Jamming of soft particles: geometry, mechanics, scaling and isostaticity. *Journal of Physics-Condensed Matter*, 22, 2010.
- [163] I. Jorjadze, L. Pontani, and J. Brujic. Microscopic approach to the nonlinear elasticity of compressed emulsions. *Physical Review Letters*, 110(4):048302, 2013.
- [164] D. J. Durian. Foam mechanics at the bubble scale. *Physical Review Letters*, 75(26):4780–4783, 1995.
- [165] R. Kurita, D.B. Ruffner, and E.R. Weeks. Measuring the size of individual particles from three-dimensional imaging experiments. *Nature communications*, 3:1127, 2012.
- [166] M.N. van der Linden, D. El Masri, M. Dijkstra, and A. van Blaaderen. Expansion of charged colloids after centrifugation: formation and crystallisation of long-range repulsive glasses. *Soft Matter*, 9:11618–11633, 2013.
- [167] L.E. Silbert, A.J. Liu, and S.R. Nagel. Structural signatures of the unjamming transition at zero temperature. *Physical Review E*, 73:041304, 2006.
- [168] G.S. Cargill. Dense random packing of hard spheres as a structural model for noncrystalline metallic solids. *Journal of applied physics*, 41:2248–2250, 1970.

- [169] T.M. Truskett, S. Torquato, S. Sastry, P.G. Debenedetti, and F.H. Stillinger. Structural precursor to freezing in the hard-disk and hard-sphere systems. *Physical Review E*, 58:3083–3088, 1998.
- [170] S.P. Pan, J.Y. Qin, W.M. Wang, and T.K. Gu. Origin of splitting of the second peak in the pair-distribution function for metallic glasses. *Physical Review B*, 84:092201, 2011.
- [171] T.A. Caswell, Z.X. Zhang, M.L. Gardel, and S.R. Nagel. Observation and characterization of the vestige of the jamming transition in a thermal three-dimensional system. *Physical Review E*, 87, 2013.
- [172] P.J. Steinhardt, D.R. Nelson, and M. Ronchetti. Bond-orientational order in liquids and glasses. *Physical Review B*, 28:784, 1983.
- [173] W. Lechner and C. Dellago. Accurate determination of crystal structures based on averaged local bond order parameters. *The Journal of chemical physics*, 129:114707, 2008.
- [174] P.R. Ten Wolde, M.J. Ruiz-Montero, and D. Frenkel. Numerical evidence for bcc ordering at the surface of a critical fcc nucleus. *Physical Review Letters*, 75:2714, 1995.
- [175] A. Fery, F. Dubreuil, and H. Möhwald. Mechanics of artificial microcapsules. *New journal of Physics*, 6:18, 2004.
- [176] Reissner.E. Stresses and small displacement of shallow spherical shells.i. *JMathPhys*, pages 80–85, 1946.
- [177] Reissner.E. Stresses and small displacement of shallow spherical shells.ii. *JMathPhys*, 312:279–300, 1946.
- [178] J. Zhou and A.D. Dinsmore. A statistical model of contacts and forces in random granular media. *Journal of Statistical Mechanics: Theory and Experiment*, 2009:05001, 2009.
- [179] J. Geng, G. Reydellet, E. Clement, and R.P. Behringer. Greens function measurements of force transmission in 2d granular materials. *Physica D: Nonlinear Phenomena*, 182:274–303, 2003.
- [180] D.M. Mueth, G.F. Debregeas, G.S. Karczmar, P.J. Eng, S.R. Nagel, and H.M. Jaeger. Signatures of granular microstructure in dense shear flows. *Nature*, 406:385–389, 2000.
- [181] S. Ostojic, T.J.H. Vlugt, and B. Nienhuis. Universal anisotropy in force networks under shear. *Physical Review E*, 75:030301, 2007.
- [182] J.H. Snoeijer, W.G. Ellenbroek, T.J.H. Vlugt, and M. van Hecke. Sheared force networks: Anisotropies, yielding, and geometry. *Physical Review Letters*, 96:098001, 2006.
- [183] Y.L. Wu, J.H.J. Brand, J.L.A. van Gemert, J. Verkerk, H. Wisman, A. van Blaaderen, and A. Imhof. A new parallel plate shear cell for in situ real-space measurements of complex fluids under shear flow. *Review of Scientific Instruments*, 78:103902–103902–11, 2007.



# Summary

This thesis covers experiments performed with elastic shells in two areas of research: in the field of microencapsulation and for the study of jammed matter. It is the flexibility of the shell that plays a pivotal role in both these studies. The shells that we used for these purposes are made of a semipermeable polymer network of tetraethoxysilane-crosslinked-polydimethylsiloxane (*TC – PDMS*). The shells were addressed as (micro)capsules in chapter 2 and 3, as both chapters highlight the capability of shells in microencapsulation applications.

In chapter 2 we describe the synthesis of monodisperse capsules (shells) of diameter larger than  $3 \mu\text{m}$  on a bulk scale. The synthesis was based on a well known emulsion templating technique where we coat the liquid droplet template by a thin polymeric shell. For *TC – PDMS* capsules we used polydimethylsiloxane (*PDMS*) oil droplets as the templates that are formed by base catalyzed hydrolysis and condensation of the difunctional monomer dimethyldiethoxysilane (*DMDES*). The capsule size is determined by the size of the droplet template, and so we developed various convenient methods to prepare large *PDMS* oil droplet template. These include the use of a Turrax homogenizer for the effective mixing of the monomer, prehydrolysing the monomer, shaking of a preformed polydisperse emulsion, and finally a seeded growth procedure where *PDMS* droplets were exposed to *DMDES* monomer or hydrocarbons or a silicone oil. In a final step a thin shell of tetraethoxysilane-crosslinked-polydimethylsiloxane was formed around the droplet by the interfacial polymerization of tetraethylorthosilicate (*TEOS*) and *PDMS* via a post addition method in the presence of poly(vinylpyrrolidone) (*PVP*) stabilizer that prevented capsule aggregation.

Chapter 3 describes a robust encapsulation and release strategy for *TC – PDMS* capsules. The materials that were encapsulated/released included different apolar liquids and fluorescent dye molecules. The strategy used for the release of encapsulated oil from preformed capsules was based on the dissolution of oil by surfactant micelles outside the capsules. Depending on the ratio of shell thickness to particle radius ( $d/R_t$ ), capsules formed different morphologies. In the range of  $d/R_t = 0.007\text{-}0.05$  they were bowl shaped, where the depth of the bowl could be tuned by changing the surfactant concentration, indicative of controlled release of encapsulant. We showed that the bowls can be further used to load oils, where the elasticity of the capsule wall and the left-over *PDMS* oil inside the capsule drove the uptake of different oils. Depending on the chemical nature of oil and kinetics at which the content was able to pass through the shell, particles formed different shapes during encapsulation. The bowls formed spheres in the presence of silicone oil, they were overloaded and formed dumbbells in

the presence of low molecular weight oils and finally they became thinner (with a deep dimple) when high molecular weight oils were added.

The last three chapters of the thesis focus on the study of the jamming phenomenon in systems of flexible elastic shells, starting with a 3D quantitative analysis of tracking of shells using confocal microscopy in combination with image processing (chapter 4). For jamming studies the shells were dispersed in an index matching solvent, after removing the *PDMS* core from inside. The shells were prepared following the Turrax homogenizer method described in chapter 2. Jammed states of shells were obtained by unidirectional compression by centrifugation in a capillary that resulted in regions of different volume fractions in the sediment. At high volume fractions the shells were in close contact with each other and underwent deformation such that one of the shells formed a dimple and the other remained spherical at contact regions. Therefore, the volume of the shell was not conserved anymore. From the 3D stack of confocal images of shells, which appeared anisotropic both in shape and fluorescent intensity distribution, we extracted the coordinates and radii of the shells in three steps: locating the edges of shells in all 2D slices, analyzing their shape to obtain their 2D coordinates, and finally determining their 3D centers by grouping the corresponding 2D coordinates. In addition to this we identified the shell that contained the dimple by measuring the position of the peak of the intensity distribution along the 3D line connecting the centers of particle pairs.

From the coordinates and radii of particles we investigated the microstructure and contact force network in jammed packings of shells as a function of distance to the jamming transition, as described in chapter 5. The parameters that gave insight about the structure of the packing of shells are the radial distribution function, local bond order parameter, contact number and buckling number. The radial distribution function in jammed packings showed resemblance to the structure of liquids, except that the amplitude of the peaks decayed and the width of the peaks increased with increasing volume fraction. Even the position of the first peak shifted to a distance less than the diameter of the particle, caused by the deformation of shells at contact regions. The distribution of the local bond order parameter at various volume fractions also confirmed the amorphous or fluid-like structure of the packings.

Another structural feature, the contact number, showed a power law scaling with distance to jamming point. The value of the scaling parameters were found to depend on whether the volume of the dimple is included or not in the calculation of volume fraction. When the volume of the dimple was taken into account we obtained a similar value of scaling exponent as predicted in numerical simulation and also found in experiments on foams, compressed emulsions and granular materials. The final parameter, the buckling number that indicates the number of dimples per particle, also showed a power law scaling where the coefficients were just half the coefficients in the scaling of

contact number, because at each contact only one of the shells was dimpled and the other remained spherical. A check for the probability of dimpling one way or the other revealed the non-randomness of this process at higher volume fractions.

After studying the microstructure we investigated the contact forces between shells in these packings by measuring the depth of the dimple at contact regions. From the non-linear buckling theory of thin shells, force is proportional to the square root of the dimple depth. We observed that the probability distribution of contact forces showed a similar trend as in simulations and experiments on deformable particles that conserve volume, such as emulsion droplets and foam bubbles. At larger forces, above the mean, the probability was found to decay exponentially for the lowest volume fractions and to cross-over to a Gaussian for the highest volume fractions. The spatial distribution of contact forces showed anisotropy with large forces aligned along the direction of gravity (compression axis) for higher volume fractions, whereas in low volume fraction packings the distribution was isotropic.

Jammed materials are known to possess a yield stress, the stress below which the system behaves like a solid and above which it undergoes plastic rearrangement or flow. Chapter 6 illustrates the effects of shear deformation on jammed shells, at a volume fraction 0.835, placed between parallel plates of a shear cell mounted on top of an inverted confocal microscope. Shear was applied by moving one of the plates that created a velocity gradient perpendicular to the direction of the plate movement. Though the amount of strain in the sample was small, we observed anisotropy both in the structure and contact force network. The distribution of contact forces showed an increased probability at small and large forces with the largest changes occurring at  $\pm 20^\circ$  instead of  $\pm 45^\circ$  to the velocity axis.



# Samenvatting

Dit proefschrift beschrijft experimenten die gedaan zijn met elastische schillen op twee onderzoeksgebieden: op het gebied van micro-encapsulatie en voor de studie van vastzittende materie (Engels: "jammed matter"). Het is de flexibiliteit van de schillen die een sleutelrol speelt in deze beide studies. De schillen die we voor deze doeleinden gebruikten zijn gemaakt van een semipermeabel polymeernetwerk van polydimethylsiloxaan vernet met tetraethoxysilaan (*TC – PDMS*). Deze schillen worden in hoofdstuk 2 en 3 (micro)capsules genoemd, omdat beide hoofdstukken de mogelijkheden belichten van schillen in micro-encapsulatietoepassingen.

In hoofdstuk 2 beschrijven we de synthese op bulkschaal van monodisperse capsules (schillen) met een diameter groter dan  $3 \mu\text{m}$ . De synthese is gebaseerd op een bekende emulsie-mal techniek, waarbij we de vloeibare druppel voorzien van een dunne polymeerschil. Voor *TC – PDMS* capsules gebruikten we als mal polydimethylsiloxaan (*PDMS*) oliedruppels, die gevormd worden door base-gekatalyseerde hydrolyse en condensatie van het difunctionele monomeer dimethyldiethoxysilaan (*DMDES*). De grootte van de capsules wordt bepaald door de grootte van de druppels en dus ontwikkelden we verschillende geschikte methodes om grote *PDMS* oliedruppelmallen te maken. Deze methodes omvatten het gebruik van een Turrax homogeniseerder voor het effectief mixen van het monomeer, het prehydrolyseren van het monomeer, het schudden van een vooraf gevormde polydisperse emulsie en tenslotte een aangroei procedure, waarbij *PDMS* druppels blootgesteld werden aan *DMDES* monomeer, koolwaterstoffen of een siliconenolie. In een laatste stap werd rondom de druppels een dunne schil gevormd van polydimethylsiloxaan vernet met tetraethoxysilaan door middel van een oppervlaktepolymerisatie van tetraethyl orthosilicaat (*TEOS*) en *PDMS*. Deze werden naderhand toegevoegd in de aanwezigheid van poly(vinylpyrrolidon) (*PVP*) stabilisator, die aggregatie van capsules voorkwam.

Hoofdstuk 3 beschrijft een robuuste capsulatie- en vrijgevingsmethode voor *TC – PDMS* capsules. De materialen die gecapsuleerd/vrijgegeven werden omvatten verschillende apolaire vloeistoffen en fluorescente kleurstofmoleculen. De strategie die werd gebruikt voor het laten vrijkomen van geëncapsuleerde olie was gebaseerd op het oplossen van de olie door surfactantmicellen buiten de capsules. Afhankelijk van de verhouding tussen de schildikte en de deeltjesstraal ( $d/R_t$ ) vormden de capsules verschillende morfologieën. In het bereik van  $d/R_t=0.007-0.05$  waren ze komvormig, waarbij de diepte van de kom gevarieerd kon worden door middel van de surfactantconcentratie, wat indicatief is voor het gecontroleerd laten vrijkomen van de gecapsuleerde stof. We lieten zien dat de kommen vervolgens gebruikt konden worden voor vulling met oliën, waarbij de elasticiteit van de capsulewand en de resterende *PDMS* olie in de capsules

de drijvende krachten waren achter de opname van verschillende oliën. Afhankelijk van de chemische aard van de olie en de kinetiek waarmee de inhoud door de schillen heen ging, namen deeltjes verschillende vormen aan gedurende de capsulatie. De kommen werden bolvormig in aanwezigheid van siliconenolie, ze werden overvol en vormden halteres in aanwezigheid van oliën met een laag molecuulgewicht en ze werden dunner (met een diepe indeuking), tenslotte, wanneer oliën met een hoog molecuulgewicht werden toegevoegd.

De laatste drie hoofdstukken van dit proefschrift zijn gericht op de studie van het fenomeen van vastzitting in systemen van flexibele, elastische schillen. We beginnen met een 3D kwantitatieve analyse van het lokaliseren van schillen. Hiervoor maakten we gebruik van confocale microscopie in combinatie met beeldverwerking (hoofdstuk 4). Voor studies naar vastzitting werden de schillen gedispergeerd in een oplosmiddel met dezelfde brekingsindex als de schillen, nadat de PDMS kern uit de binnenkant verwijderd was. De schillen werden gemaakt met de Turrax homogeniseerder methode, die beschreven is in hoofdstuk 2. Toestanden van vastzitting werden verkregen door unidirectionele compressie door middel van centrifugatie in een capillair, wat resulteerde in gebieden met verschillende volumefractie in het sediment. Bij hoge volumefracties zaten de schillen dicht op elkaar en vervormden ze, zodanig dat één van de schillen ingedeukt werd en de ander bolvormig bleef op hun beider contactoppervlak. Daardoor was het volume van de schillen niet langer behouden. Uit de 3D stapel van confocale beelden van schillen, die zowel qua vorm als qua verdeling van fluorescentie-intensiteit anisotroop bleken, extraheerden we in drie stappen de coördinaten en straal van de schillen: het lokaliseren van de randen van de schillen in alle 2D doorsnedes, het analyseren van hun vorm om hun 2D coördinaten te verkrijgen en tenslotte het vaststellen van hun 3D middelpunt door het groeperen van de bijbehorende 2D coördinaten. Daarnaast identificeerden we welke schil de indeuking had door de positie van de piek te meten in de intensiteitsverdeling langs de lijn die de middelpunten van een deeltjespaar met elkaar verbond.

Uitgaande van de coördinaten en de straal van deeltjes onderzochten we de microstructuur en het netwerk van contactkrachten in vastzittende pakkingen van schillen als functie van de afstand tot de overgang naar vastzitting, zoals beschreven in hoofdstuk 5. De parameters die inzicht gaven in de structuur van de pakking van de schillen zijn de radiële distributiefunctie, de lokale-bindingsordeparameter, het contactgetal en het indeukingsgetal. De radiële distributiefunctie in vastzittende pakkingen vertoonde overeenkomsten met de structuur van vloeistoffen, behalve dat de amplitude van de pieken afzwakte en de breedte van de pieken toenam bij toenemende volumefractie. Zelfs de positie van de eerste piek schoof op naar een afstand kleiner dan de deeltjesdiameter.

Dit werd veroorzaakt door de vervorming van schillen in contactregionen. De verdeling van de lokale-bindingsordeparameter bij verschillende volumefracties bevestigde de amorfe of vloeistofachtige structuur van de pakkingen eveneens.

Een ander structureel kenmerk, het contactgetal, vertoonde een schaling met de afstand tot het vastzittingspunt volgens een machtwet. De waarde van de schalingparameters bleek af te hangen van of in de berekening van de volumefractie het volume van de indeukingen meegenomen wordt of niet. Wanneer het volume van de indeukingen meegerekend werd, verkregen we voor de schalingsexponent een vergelijkbare waarde als die voorspeld is met numerieke simulaties en die ook gevonden is in experimenten met schuimen, gecomprimeerde emulsies en granulaire materie. De laatste parameter, het indeukingsgetal, dat het aantal indeukingen per deeltje aangeeft, vertoonde eveneens een schaling volgens een machtwet, waarbij de coëfficiënten slechts de helft waren van de coëfficiënten van de schaling met het contactaantal, omdat bij elk contact slechts één van de schillen een indeuking had en de ander bolvormig bleef. Een controle van de waarschijnlijkheid dat een schil indeukt of bolvormig blijft toonde aan dat dit proces bij hogere volumefracties niet willekeurig was.

Na het bestuderen van de microstructuur onderzochten we de contactkrachten tussen schillen in deze pakkingen door de diepte van de indeuking te meten in het contactgebied. Uit de niet-lineaire indeukingstheorie van dunne schillen volgt dat deze kracht evenredig is met de wortel van de diepte van de indeuking. We vonden dat de waarschijnlijkheidsverdeling van contactkrachten een vergelijkbare trend vertoonde als in simulaties en bij experimenten aan vervormbare deeltjes die hun volume behouden, zoals emulsiedruppels en schuimbellen. Bij krachten boven het gemiddelde bleek de waarschijnlijkheid exponentieel af te nemen bij de laagste volumefracties en over te gaan in een Gaussische verdeling bij de hoogste volumefracties. De ruimtelijke verdeling van contactkrachten vertoonde voor hogere volumefracties anisotropie, waarbij de grote krachten langs de richting van de zwaartekracht (de compressieas) gericht waren, terwijl bij pakkingen met lage volumefractie de verdeling isotroop was.

Het is bekend dat materialen in toestand van vastzitting een vloeigrens hebben. Beneden deze grens gedraagt het systeem zich als een vaste stof en erboven ondergaat het plastische herschikking of stroming. Hoofdstuk 6 illustreert het effect van schuifvervorming op vastzittende schillen, bij een volumefractie van 0.835, geplaatst tussen de parallelle platen van een schuifcel die bovenop een geïnverteerde confocale microscoop is geplaatst. Afschuiving werd uitgeoefend door het bewegen van één van de platen, wat een snelheidsgradiënt veroorzaakte loodrecht op de bewegingsrichting van de plaat. Hoewel de hoeveelheid vervorming in het monster klein was, namen we anisotropie waar in zowel de structuur als in het netwerk van contactkrachten. De verdeling van contactkrachten vertoonde een verhoogde waarschijnlijkheid voor kleine

en grote krachten, waarbij de grootste veranderingen optraden bij  $\pm 20^\circ$  in plaats van bij  $\pm 45^\circ$  ten opzichte van de bewegingsrichting.

# Acknowledgments

This thesis would not have been possible without the help and support of many people around me. Here I would like to extend my appreciation and gratitude to them.

I express my sincere gratitude to my supervisors Prof. Alfons van Blaaderen and Dr. Arnout Imhof for giving the opportunity to pursue my PhD. Arnout, it is your active involvement throughout the entire project that I am able to reach the finishing line. I thank you from the bottom of my heart for the generous support, guidance, innumerable discussions and listening to me at times of frustration. Thank you Alfons for the many insightful discussions, guidance and for your wise and valuable suggestions. I am also deeply grateful to you for giving your timely comments on most of the thesis chapters.

My Sincere thanks to the committee members Marjolein Dijkstra, Martin van Hecke, Rene van Roij, Albert Philipse and Hans Gerritson for participating in my thesis defence.

I would like to thank my collaborators and colleagues who have contributed to my thesis or have kindly shared their skills and knowledge. Nina, I had a great time working with you on synthesis of these shells. Thanks for the numerous fruitful discussions, constructive criticism on my writing and for the initiative to meet up for coffee or dinner. I wish you good luck with your thesis. Marlous, thank you for your contributions in the paper/chapter on microencapsulation and for many useful discussions. My sincere thanks to Gerhard, Anjan, Bas, Johan, Thijs and Ernest for writing or sharing their programs for the quantitative analysis of jammed packings of shells. Thijs, thanks for the useful discussions on image processing and shear experiments. Peter, thanks for helping with experimental setups, especially shear cell, and fixing problems with my computer. Coming from a physics background, little did I know about safely dealing with chemicals and doing synthesis, although my cooking skills helped a bit there. Thanks to Judith, Gülşen, Bo, Stéphane, Bing and all my fellow colleagues working in the synthesis lab for their kind help. Thank you Thea, Maria, Maria (FOM), Marjoke and Marion for secretarial support. I would also like to thank John, Johan, Thijs and Ernest for proof reading some of the chapters in my thesis. Thank you Krassimir and Patrick for valuable suggestions and discussions.

I am thankful to my officemates, Johan and Wessel, for setting up a good working ambience in room 012. I am glad to have shared office space with both of you - two guys with extremely good baking skills. Thanks for those cakes and cookies at times when I skipped coffee breaks. I enjoyed our conversations whether it be scientific or in general and our trip to Den Bosch is a highly memorable one. Johan, thank you for the informative talks, numerous help on dutch translation and Latex, and being a good listener. Thanks for the samenvatting. Thanks Teun, Alessandro, Peter, Marjolein,

Anke and Rao for the scientific and friendly talks. My sincere thanks to all my former and present SCM colleagues for their support during my PhD. Thanks to colleagues from the Biophysics, especially Helena for introducing me to yoga and appelbollen, which turned out to be one of my favorite dutch sweet.

I am grateful to my friends, for the occasional social gatherings and of course for the incredible food that we shared. Thanks Bill, our counselling sessions were extremely helpful and it was a good experience. Harry, thanks for the career advices and it was a great relief talking to you during thesis writing.

I express my wholehearted gratitude to my parents. It is your unconditional love, support and blessings, that made me reach so far. Many thanks to Jesmy and Shaine, Jainy, Jincy and Mathew for your love, encouragement and just being an awesome family. Above all I thank God for the countless blessings showered upon me and guiding me throughout my life.

# List of publications

This thesis is partly based on the following publications

N. Elbers\*, J. Jose\*, A. Imhof, A. van Blaaderen. Bulk scale synthesis of monodisperse, permeable microcapsules with diameters above  $3 \mu\text{m}$ , \*These authors contributed equally, in preparation - Chapter 1

J. Jose, M. Kamp, A. van Blaaderen, A. Imhof. Unloading and reloading of colloidal microcapsules with apolar solutions by controlled and reversible buckling, *Langmuir* 2014, 30, 2385-2393 - Chapter 2

J. Jose, G. Blab, A. van Blaaderen, A. Imhof, Quantitative study of 3D microstructure of amorphous packing of compressed elastic shells, in preparation - Chapter 4 & 5

J. Jose, A. van Blaaderen, A. Imhof, Quantitative study of 3D force network in amorphous packing of elastic shells under static compression and shear, in preparation - Chapter 5 & 6

## Other publications

T. H. Besseling, J. Jose and A. van Blaaderen. Methods to calibrate and scale axial distances in confocal microscopy as a function of refractive index, in preparation

# About the author

Jissy Jose was born on 10 April 1986, in Cochin, Kerala, India. She obtained her Bachelor (2006) and Master (2008) degree in Physics from Mahatma Gandhi University, India. In September 2009, she joined the Soft Condensed Matter group, Utrecht University, The Netherlands, as a PhD student under the supervision of Prof. Alfons van Blaaderen and Dr. Arnout Imhof. Her work involved synthesis of large elastic polymeric shells and their potential use as a model system for studying jammed granular matter and in controlled encapsulation/release of apolar solutions. The results of that work are presented in this thesis. She presented her results in various international and national conferences.